Charles University

Faculty of Science

Institute of Geology and Paleontology

Master‘s programme: Geology

Branch of study: Basic geology

Bc. Petr Vitouš

From deposition to caldera resurgence: pyroclastic density current dynamics as revealed by magnetic anisotropy of the Teplice rhyolite, Bohemian Massif

Od uložení po kalderovou resurgenci: dynamika pyroklastických hustotních proudů zjištěná magnetickou anisotropií z Teplického ryolitu, Český masiv

Diploma thesis

Supervisor: Mgr. Filip Tomek, PhD.

Prague 2020

Prohlášení

Prohlašuji, že jsem tuto práci sepsal samostatně, a že jsem veškerou použitou literaturu a informační zdroje řádně citoval. Dále prohlašuji, že tato práce nebyla použita jako závěrečná práce pro získání jiného nebo obdobného druhu vysokoškolské kvalifikace.

V Praze dne 14. 8. 2020 ……

Acknowledgements

I hereby greatly acknowledge my supervisor Filip Tomek for overseeing and leading my work. Further, I thank him and Jiří Žák for introducing me into geology of the Teplice rhyolite and Altenberg–Teplice caldera. I also acknowledge Lesy ČR a.s., namely its branches Telnice and Litvínov, for forest research allowance. Field campaigns and preparations of the samples were financed by the Czech Science Foundation Junior Grant No. 19-02177Y to Filip Tomek. Furthermore, I thank Mr. Jiří Petráček for AMS samples preparation, and Marta Tomková and Milena Vostrá for the preparation of thin-sections. At last but not least, I would like to express great appreciation to the Institute of Geology and Paleontology, Faculty of Science at Charles University, for providing of Laboratory of Rock Magnetism and great overall study environment.

Abstract

Better understanding of pyroclastic density current (PDC) dynamics is one of the key volcanological focuses, as PDCs represent one of the most life-threatening volcanic hazards. PDCs associated with explosive collapse calderas are difficult to observe and examine directly, and thus research of internal architecture of calderas and their PDC deposits is focused on extinct and partly eroded volcano-plutonic systems. Such a case is the Late-Carboniferous Altenberg–Teplice caldera in NW Bohemian Massif, which exposes a large body of ignimbrites (deposits of the PDC) called Teplice rhyolite (an intra-caldera fill). This body is well exposed on the southern flank of the Krušné hory/Erzgebirge Mts., mainly its members: Teichweg, Lugstein-Pramenáč, Vlčí kámen-Medvědí vrch and Přední Cínovec. As these ignimbrites appear macroscopically isotropic, I employed the Anisotropy of magnetic susceptibility (AMS) in order to quantify their internal structure. A total of 1232 specimens from 63 sampling stations were analyzed for the AMS, complemented by susceptibility vs. temperature variations and petrographic observations. Obtained AMS data, carried by a mixture of paramagnetic ferrosilicates and low-Ti titanomagnetite, indicate various processes recorded in ignimbrites. The relatively oldest and moderately welded Teichweg member exhibit subhorizontal oblate magnetic fabrics indicating general westward flow directions corroborated by asymmetry of flow foliated flattened fiamme, whereas the source vents were likely situated around the eastern caldera rim. In contrast, Lugstein-Pramenáč, Vlčí kámen-Medvědí vrch and Přední Cínovec members are characterized by higher degree of anisotropy and triaxial to prolate magnetic fabrics, indicating rheomorphic viscous flow obscuring primary flow fabrics. In addition, I hypothesize magnetic fabrics of some local domains around younger post-caldera intrusions are compatible with caldera resurgence that occurred shortly after deposition of still hot and ductile ignimbrites. In terms of PDC dynamics, the exposed portion of the Teplice rhyolite is complex body recording PDC flow directions, welding, rheomorphism and possible a caldera resurgence.

Keywords: Anisotropy of magnetic susceptibility (AMS); Pyroclastic density current; Welding; Rheomorphism; Caldera resurgence; Rhyolite

Abstrakt

Porozumění dynamice pyroklastických hustotních proudů (PDC) je jednou z klíčových otázek moderní vulkanologie, jelikož PDC jsou jedním z nejvíce život ohrožujících vulkanických rizik. PDC jsou často spojovány se silně explozivními kolapsovými kalderami, avšak pro jejich nebezpečnou povahu se nedají studovat přímo. Výzkumy vnitřních struktur kalder a PDC se tudíž soustředí na vyhaslé a erozí odhalené horniny kalder. Jedním z příkladů je svrchně karbonská altenbersko–teplická kaldera situovaná v severozápadní části Českého masívu, uvnitř které se zachovaly relikty intrakalderové výplně souhrnně nazývané teplický ryolit. Na jižních svazích Krušných hor vystupují jednotlivé členy teplického ryolitu: Teichweg, Lugstein-Pramenáč, Vlčí kámen-Medvědí vrch a Přední Cínovec, které jsou složené téměř výhradně z ignimbritů, uloženin PDC. Jelikož se tyto horniny jeví makroskopicky izotropní, použil jsem metodu Anisotropie magnetické susceptibility (AMS) ke kvantifikaci jejich vnitřních staveb. Celkem bylo odebráno 1232 AMS válečků ze 63 lokalit na analýzu AMS struktur, která byla doplněna měřením závislosti susceptibility na měnící se teplotě a petrografickým popisem. Získaná AMS data, jejichž susceptibilita je dominována paramagnetickými ferosilikáty a titanomagnetitem s nízkým obsahem Ti, zaznamenávají různorodé pochody uchované v horninách Teplického ryolitu. Relativně nejstarší a středně spečený (moderately welded) člen Teichweg je charakteristický subhorizontálními oblátními magnetickými foliacemi a tokovými foliacemi podél fiammé, zaznamenávající tok PDC směřující generelně od východu k západu. Předpokládaná přívodní oblast je situovaná v oblasti východního okraje kaldery. Naopak relativně mladší členy Lugstein-Pramenáč, Vlčí kámen-Medvědí vrch a Přední Cínovec se vyznačují vyšším stupněm anisotropie a triaxiálními až prolátními magnetickými stavbami. Tyto stavby byly způsobeny duktilní reomorfní deformací v důsledku viskózního toku ignimbritu po uložení PDC. Tato událost tudíž způsobila přetištění primárních tokových staveb PDC. Předpokládám, že některé magnetické stavby byly dále ovlivněny resurgencí v důsledku intruze mladších post-kalderových žil, což se muselo stát krátce po uložení ignimbritů, které byly stále horké a náchylné k duktilní deformaci. Teplický ryolit je tudíž komplexní těleso zaznamenávající širokou škálu procesů od uložení PDC, spečení, přes duktilní reomorfismus až po možný záznam post-kalderové resurgence.

Klíčová slova: Anisotropie magnetické susceptibility (AMS); Pyroklastický hustotní proud; Spečení; Reomorfismus; Kalderová resurgence; Ryolit

Table of contents

1 Introduction

1.1 Pyroclastic density currents and ignimbrites

Caldera is a volcanic depression formed by a gravitation-driven collapse of an overlying floor (original surface) into a magma chamber that was partially exhausted by voluminous eruptions (e.g., Lipman, 1997; Cole et al., 2005; Acocella, 2006, 2007). These eruptions are very often of Plinian character associated with ash clouds and pyroclastic density currents (PDCs). PDCs transport juvenile and lithic material to great distances, up to tens to hundreds of kilometers away, and can climb up obstacles even more than 1000 m high (e.g., Ross and Smith, 1961; Fisher et al., 1993). PDCs are characterized as a rapidly moving dense mix of volcanic ash, hot gases (steam, SO_2, H_2S, CO_2, NO_x, etc.), pumice, crystal and lithic fragments, which is initiated when a part of the erupted material in the ash cloud becomes too dense and collapses. After a deposition, they are compacted into a special igneous rock collectively referred to as an ignimbrite (e.g., Elston & Smith, 1970; Sparks, 1976; Zrelak et al., 2020).

PDCs are also known under other names like *nuée ardente* (fiery cloud, regarding its glowy appearance in the dark), ash-flows, pyroclastic flows, pumice flows or simply ignimbrite flows. These rocks are not associated exclusively with caldera-forming eruptions (Rose & Chesner, 1987; Willcock et al., 2015), but can also be found in relation to phreatomagmatic eruptions and maars (e.g., Porreca, 2003), or to stratovolcanoes (e.g., Zrelak et al., 2020).

Sparks (1976) suggested for PDCs an *en masse* emplacement (in mass; meaning "at once") similar to laminar debris flow. He imagined that the PDC would travel as basically non-deforming mass, however, this image of the current is based on the deposited ignimbrite, which usually appears as a thick massive unit. Instead, Branney and Kokelaar (1992, 2002) proposed that the deposition is rather continuous, and involves incremental aggradation from a sustained current.

The aerial extent of a PDC can vary depending on the eruption volume and energy, but most of PDCs can travel 3–10 km (e.g., Zrelak et al., 2020) away from the volcano, whereas some super-eruptions are capable of producing voluminous PDCs reaching distances over 100 km far from the source vent (e.g., Chapin & Lowell, 1979; Roche et al., 2016). At proximal distances from the source (first hundred meters to kilometers), the PDC is usually highly turbulent, deposition is rapid, and sorting of the material does not occur

much, even with large blocks. However, with increasing distance from the vent, the pyroclastic flow becomes more laminar and gradually changes its texture from massive to layer-stratified, and grain size from coarse- to fine-grained (e.g., Ross and Smith, 1961; Branney and Kokelaar, 2002).

The vertical section of an ignimbrite can be divided into three units described as follows: (1) a base (ground) surge forming a thin, very coarse and often cross-bedded layer; (2) main flow unit in the middle starting with a well-sorted fine-grained lowermost layer overlain by an unsorted ignimbrite; and (3) a fine-grained and crystal-poor upper-most unit (Sparks, 1976).

The instantaneous syn- to post-deposition processes comprise (1) welding compaction and/or (2) rheomorphism. (1) Welding can be imagined as compaction due to higher temperatures and/or ductile deformation produced by an overlying younger ignimbrite mass, depending on several properties like temperature, volume, or composition. It is petrographically revealed by a groundmass deformed to a greater or lesser extent and reduction of pore space. Ignimbrite welding is essentially distinguished as (a) primary and (b) secondary (e.g., Chapin & Lowell, 1979). (a) Primary welding is a syn-depositional process produced by agglutination of deposits by newly deposited increment if the pyroclastic particles are sufficiently hot. (b) Secondary welding, on the other hand, is when welding temperature is decreased due to an increase of a lithostatic pressure produced by an overlying mass. Different degrees of welding can be observed, from non-welded tuffs to densely welded (e.g., Chapin and Lowell, 1979; Branney and Kokelaar, 1992; Pioli et al., 2008). (2) When the deposited PDC is even hotter, a rheomorphism (ductile deformation) takes place. It can occur either as a syn-depositional transformation of the pyroclastic turbulent flow into a late-stage viscous flow or as a post-depositional re-mobilization. Such ignimbrites are then forming lava-like textures, lithologically almost indistinguishable from lavas (Ross and Smith, 1961; Branney and Kokelaar, 1992; Branney et al., 2004).

1.2 Case study

For this study, I have chosen the Teplice rhyolite of the Late Carboniferous Altenberg–Teplice caldera (e.g., Breiter et al., 2001; Štemprok et al., 2003; Mlčoch and Skácelová, 2010; Casas-García et al., 2019). The ~318–312 Ma Teplice rhyolite represents a deeply eroded caldera fill comprising dominantly of ignimbrites (e.g., Jiránek et al., 1987;

Schovánek et al., 2004; Casas-García et al., 2019; Tomek et al., under review). These ignimbrites are well exposed on the southern flank of the Krušné hory/Erzgebirge Mts. on the border between Czechia and Germany (Saxothuringian unit, NW Bohemian Massif; Fig. 1a and b). I have examined the Teplice rhyolite through detailed geological mapping, petrographic analyses and magnetic fabrics determined using the Anisotropy of magnetic susceptibility (e.g., Hrouda, 1982; Hrouda and Kahan, 1991; Tarling and Hrouda, 1993; Borradaile, 2001; Borradaile and Jackson, 2010). After a brief introduction into the geological setting and methodology, I present a dataset of 1232 AMS specimens collected at 63 sampling sites, and describe their scalar and vector parameters. Further on, I discuss this dataset with respect to flow direction, degree of welding and rheomorphism of the Teplice rhyolite, and caldera resurgence.

2 Geological setting

2.1 Late-Variscan magmatic activity

The Variscan orogeny is one of the main global geological events in the Late Paleozoic (e.g., Pin, 1990; Veevers, 2004; Kroner and Romer, 2013). It has created an orogen a few thousand kilometers long and several kilometers high during the Pangea supercontinent amalgamation (e.g., Matte, 1986). This orogenic process formed due to the dextral convergence and collision of Gondwana in the south and Laurussia in the north, which progressively subducted and closed the Rheic Ocean together with the convergence of several other smaller microcontinents (e.g., Tait et al., 1997; Pharaoh, 1999; Franke, 2006; Kroner and Romer, 2013; Stampfli et al., 2013). One of the main and largest relics of the European Variscan belt is the Bohemian Massif (Fig. 1a; e.g., Franke and Żelaźneiewicz, 2002; Winchester et al., 2006).

The Bohemian Massif forms the geological basement of the Czechia, Germany, Austria and Poland. It is composed of four main lithotectonic units: Saxothuringian, Teplá-Barrandian, Moldanubian, and Brunovistulian. Borders between these are not always well exposed, however, they can be distinguished upon their geological and geophysical properties (e.g., Babuška and Plomerová, 2013).

Formation of the Bohemian massif commenced by subduction of the Saxothuringian ocean towards SE beneath the Teplá-Barrandian microplate followed by a continental collision at ~380–346 Ma (e.g., for overview see Schulmann et al., 2009, 2014; Žák et al., 2014 and references therein). This caused a transpression shortening of the Teplá–Barrandian unit (e.g., Rajlich, 1988; Žák et al., 2009) and emplacement of the calc-alkaline to high-K magmatic-arc granites of the Central Bohemian Plutonic Complex (e.g., Holub et al., 1997a, 1997b; Janoušek and Holub, 2007). This convergent phase was followed by a gravitational collapse of the Teplá–Barrandian unit and exhumation of the Moldanubian high-grade metamorphic core at ~346–335 Ma (e.g., Zulauf et al., 2002; Žák et al., 2005, 2012; Schulmann et al., 2009, 2014; Dörr and Zulauf, 2010). Later, the Brunovistulian unit was underthrusted from the east under the assemblage of Saxothuringian/Teplá-Barrandian/Moldanubian units, ceasing at around 330 Ma (e.g., Guy et al., 2011; Verner et al., 2014; Racek et al., 2017). The orogenic collapse was associated with extensive crustal anatexis and emplacement of voluminous peripheral S-type granites and high-K to ultra

high-K melagranites and melasyenites at ~335–315 Ma (e.g., Finger et al., 2009; Kotková et al., 2010; Žák et al., 2014, 2018; Janoušek et al., 2019).

Apart from the ultra-potassic melagranites and melasyenites, the late-Variscan magmatism is mostly represented in the Bohemian Massif by the Moldanubian batholith and surrounding Saxothuringian plutonic bodies (Fig. 1b). Moldanubian batholith is exposed in two branches: (1) NE–SW trending in the central part of the Moldanubian unit and (2) NW–SE trending along the Czech southwestern border (e.g., Liew et al., 1989; Klečka and Matějka, 1996; Finger et al., 2009). Moreover, peripheral magmatism is also represented by the Saxothuringian units plutons. To the NE, these are for instance by the Krkonoše–Jizera plutonic complex, Strzegom-Sobótka, Strzelin, Kłodsko-Złoty Stok, Žulová plutons and others. The NW and W part is dominated by the Krušné hory/Erzgebirge Mts. batholith.

In the Krušné hory/Erzgebirge Mts. (western Saxothuringian unit; Fig. 1b), this post-collisional magmatism took place mainly during a time span of 330–285 Ma (e.g., Štemprok, 1993; Breiter et al., 1999; Förster et al., 1999; Štemprok et al., 2007; Finger et al., 2009; Breiter, 2012). Even though magmatic activity in the Krušné hory/Erzgebirge Mts. have dominantly formed larger batholiths, the present-day erosional level exposes deeply eroded shallow level volcano-plutonic complexes as well. In general, the rocks of the Krušné hory/Erzgebirge Mts. batholith have compositional evolution from mafic to dominant felsic, and generally are strongly peraluminous S-type, moderately peraluminous A-type and moderately peraluminous transitional I–S-type (e.g., Tischendorf and Förster, 1990; Breiter et al., 1999; Breiter, 2012). Based on age and composition, the granites of the Krušné hory/Erzgebirge Mts. are traditionally divided into two major groups: Older (~325–315 Ma) and Younger Intrusive Complex (~305–285 Ma; Lange et al., 1972; Vigneresse, 2001; Štemprok et al., 2003). Förster et al. (1999) have also subdivided these intrusions into: (1) low-F biotite granites (e.g., Kirchberg granite), (2) low-F two-mica granites (e.g., Bergen granite), or (3) high-F, high-P_2O_5 and Li-mica granites, which geochemically exhibit the highest differentiation (e.g., Eibenstock granite). Between 1945–1980, the Krušné hory/Erzgebirge granites were studied in greater detail due to prospection of mineral and ore deposits (e.g., Tischendorf and Förster, 1990; Förster and Tischendorf, 1994; Štemprok et al., 2003).

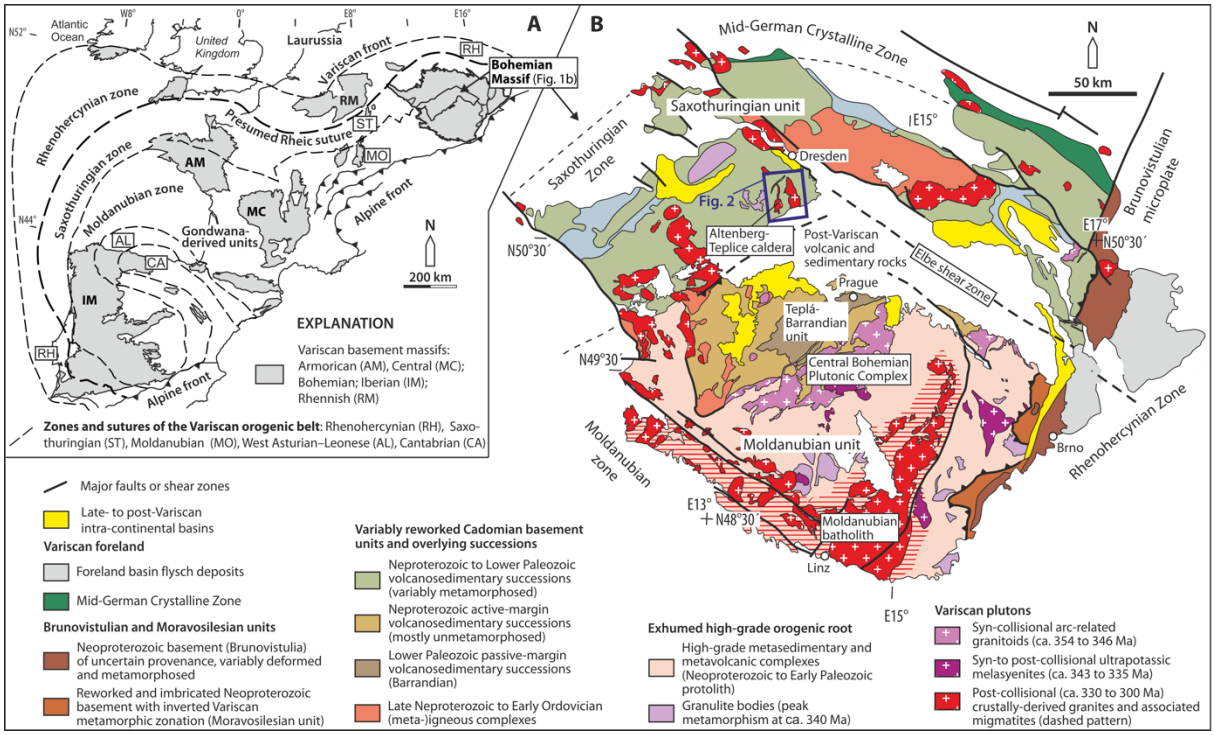

Fig. 1 a) Simplified sketch map of the European Variscides showing individual zones, sutures and major exposures; modified after Žák et al. (2014); b) overview geologic map of the Bohemian Massif based on 1:500.000 maps of Fusán et al. (1967) and Cháb et al. (2007).

2.2 Altenberg–Teplice caldera

The Late Carboniferous Altenberg–Teplice caldera belongs to the late-Variscan post-collision magmatic activity in the western area of Krušné hory/Erzgebirge batholith of the northwestern Bohemian Massif (Figs. 1b, 2a). At the present-day erosional level, the Altenberg–Teplice caldera is prolonged in ~NNW–SSE direction and is approximately 26 × 18 km large, however, another ~10 km (ca. one third) is covered by younger Cenozoic volcanic rocks of the Ohře/Eger graben and coal-bearing sedimentary basins (Figs. 1b, 2a; e.g., Breiter et al., 2001; Mlčoch and Skácelová, 2010). Genetically, the caldera collapse (by definition of Lipman, 1997) is an asymmetric trapdoor type, with maximum subsidence in the southeastern part (Fig. 2a–c; Benek, 1991). Here, the largest accumulation of proximal caldera volcanic facies is exposed (Fig. 2a, b; Jiránek et al., 1987; Benek, 1991). Recently, Tomek et al. (2019) suggested that the subsidence dynamics might have been more complex, while combining trapdoor and downsag collapse components assisted by one or more normal faults within the caldera floor (Mlčoch and Skácelová, 2010). The Altenberg–Teplice caldera was emplaced into various orthogneiss and paragneiss complexes including relics of phyllites and metabasaltic nappes. These host rocks were

deformed and metamorphosed during the early stages of the Variscan orogeny (e.g., Schovánek et al., 2004; Mlčoch and Skácelová, 2010).

The Altenberg–Teplice caldera comprises several plutonic, hypabyssal and volcanic units sorted here based on geologic mapping and cross-cutting relations from relatively oldest to youngest units. Evolution of the caldera started by emplacement of the pre-caldera Fláje monzogranite pluton (e.g., Förster et al., 1999; Štemprok et al., 2003) and the Schönfeld–Altenberg volcano-sedimentary depression (Walther et al., 2016). This was followed by intrusion of rhyolite and microgranite dikes (Sayda-Berggießhübel dike swarm) oriented ~NE–SW and ~N–S to ~NNW–SSE and interpreted as a possible source for the intra-caldera fill of the Teplice rhyolite (e.g., Winter et al., 2008). The Teplice rhyolite consists of fall tuffs, ignimbrites and lava complexes intercalated with volcano-sedimentary horizons (e.g., Fiala, 1960; Lobin, 1986; Jiránek et al., 1987). Termination of volcanic activity is highlighted by the emplacement of the ring dike system encircling most of the caldera (Müller and Seltmann, 2002; Tomek et al., 2019). The evolution of the Altenberg–Teplice caldera was completed by post-collapse sub-volcanic A-type granitic intrusions, which were accompanied by post-magmatic Sn-W-Li greisen mineralizations (e.g., Štemprok et al., 2003, 2014; Štemprok, 2016). Each unit is described in detail below.

The precise timing of magmatic activity of the Altenberg–Teplice caldera has been debated over the last ca. 20 years. Different radiometric methods yielded contrasting results, which were in some case in variance with biostratigraphy, relative ages and cross-cutting relations (see discussion in Casas-García et al., 2019). However, the new LA–ICP–MS U/Pb zircon dating of plutonic, hypabyssal and volcanic units provided a lifetime of ~325–312 Ma, with main ignimbrite activity between ~318–312 Ma peaked at ca. 313.5 Ma (Tomek et al., under review).

2.2.1 Fláje pluton

The Fláje pluton is an elliptical (elongated in ~N–S direction) composite pluton, ca. 50 km^2 large in the map at the present-day erosional level, and is located in the southwestern part of the caldera (Fig. 2a). The pluton comprises several granite facies with gradational contacts: porphyritic fine-, medium- and coarse-grained biotite monzogranites, and transitional porphyritic two-mica monzogranite (e.g., Klomínský et al., 2010). This shallow-level pluton is asymmetrically zoned, and the basicity and biotite content decrease from the south to the north (Müller and Seltmann, 2002).

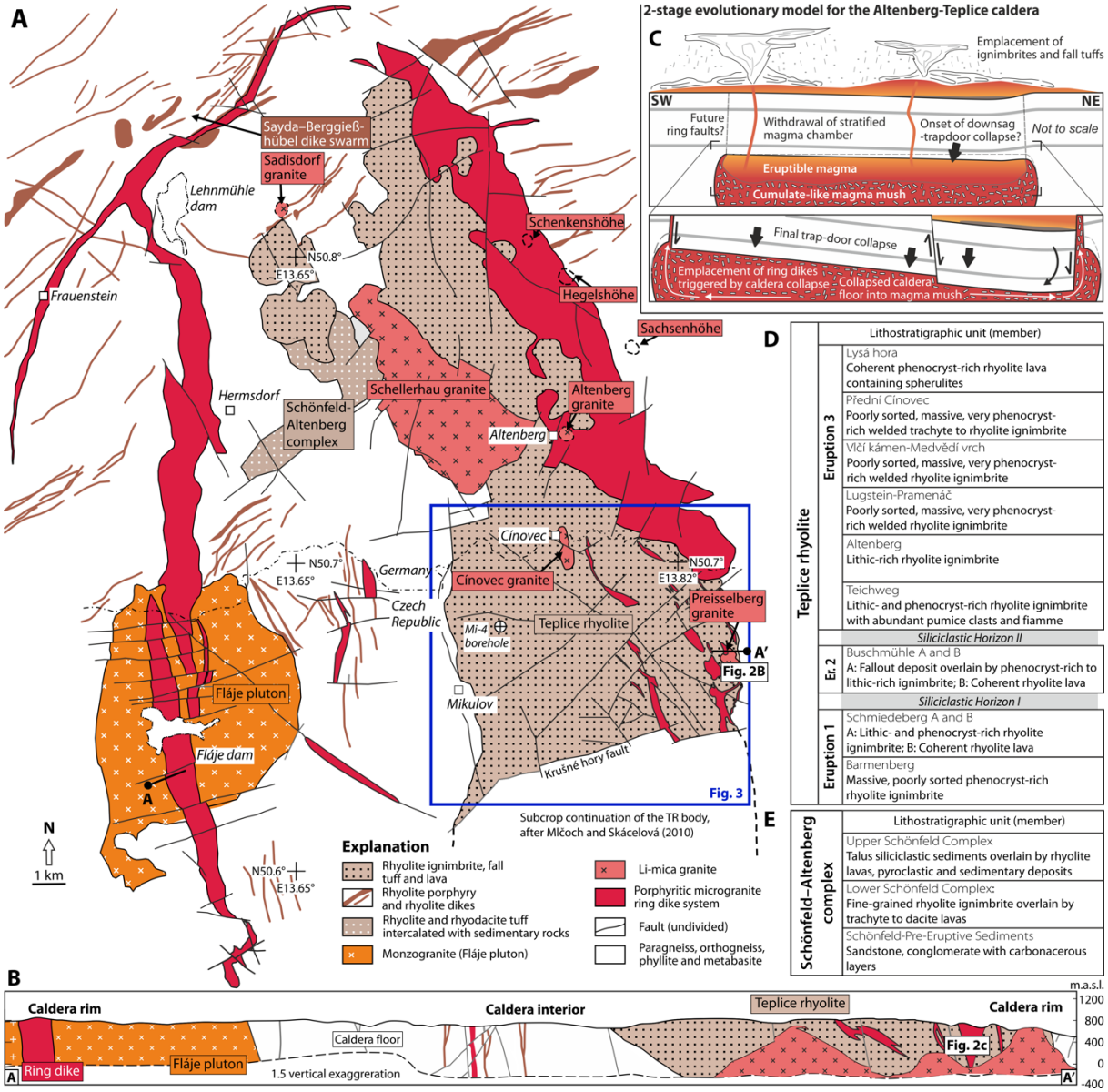

Fig. 2 a) Simplified geologic map of the Altenberg–Teplice caldera; edited and modified from Tomek et al. (2019). The blue square shows the area of interest. b) Approximately W–E cross-section through the southern portion of the caldera, modified from Jiránek (1991) and Schovánek (2004a, 2004b). c) 2-stage evolutionary model showing eruptions of the Teplice rhyolite followed by a trap door collapse triggering emplacement of ring dike system. Modified form Tomek et al. (2019). Simplified stratigraphic scheme of d) the Teplice rhyolite and e) the Schönfeld–Altenberg volcano-sedimentary depression modified from Casas-García et al. (2019) and Walther et al. (2016), respectively.

Based on the geochemical signature, the Fláje pluton has an affiliation to I- and S-type granitoids. According to Štemprok et al. (2003), the Fláje monzogranite is rather primitive with relatively high CaO contents and can be classified as low-F biotite granite of the Krušné hory/Erzgebirge Mts. batholith (Förster et al., 1999).

2.2.2 Schönfeld-Altenberg volcano-sedimentary depression

This depression crops out in the central-northern part of the Altenberg–Teplice caldera (Fig. 2a), is approximately ~10 × 15 km on the map, and consists of pre-caldera subaerial volcanic deposits, intercalated with volcanoclastic and siliciclastic sequences up to 700 m thick (Walther et al., 2016). Boreholes at several locations on the Czech and the German side have detected Schönfeld-Altenberg sequences buried also underneath the Teplice rhyolite (see below). For instance, in Czechia, these sequences were identified in Mi-4 borehole at depths ~925–625 m (Breiter et al., 2001).

Recently, Walther et al. (2016) have distinguished three major parts of volcanic, volcanoclastic and siliciclastic successions (Fig. 2e): (1) Lower Schönfeld Pre-Eruptive Sediments; (2) Lower Schönfeld Complex and (3) Upper Schönfeld Complex.

(1) The Lower Schönfeld Pre-Eruptive Sediments comprises 60–110 m of non-volcanogenic sedimentary rocks, mostly sandstones and sandy conglomerates to conglomerates, which are explained to be part of an alluvial fan and fluvial environments. They had accumulated gneiss debris and intercalations of coal and anthracite horizons (e.g., Lobin, 1986; Walther et al., 2016). (2) The Lower Schönfeld Complex is up to 160 m thick, however, in the borehole Mi-4 this sequence is about 300 m thick (Lobin, 1986; Walther et al., 2016). This complex comprises two main segments: (a) lower fine- to coarse-grained ignimbrites and tuffites and (b) overlying dacitic to rhyolitic lavas and weakly porphyritic subvolcanic bodies. Similarly, sedimentary intercalations are present, in form of anthracite or carbonaceous claystones. (3) The stratigraphically youngest Upper Schönfeld Complex is a succession formed by volcano-sedimentary rocks with up to 50 m of compact talus deposits at the base. These rocks are clast-supported, consisting almost exclusively of gneiss clasts embedded in a dark carbonaceous matrix. Above, a sequence of volcano-sedimentary rocks changes itself mostly laterally between different areas. In some parts, it consists of dominantly fluvial and alluvial fan deposits, in other parts it includes coherent volcanic rocks.

2.2.3 Sayda-Berggießhübel dike swarms

The Altenberg–Teplice caldera and its surroundings, namely area to the NW, N and NE of the caldera, are intruded by numerous rhyolitic and microgranitic dikes (Fig. 2a). Most of these dikes are oriented in ~NW–SE to WNW–ESE direction, while the rest is oriented N–S to NNW–SSE (Schust, 1980; Wetzel, 1984). Mlčoch and Skácelová (2010)

argued that some of the dikes might be older than the collapse of the caldera, while the N–S to NNW–SSE striking dikes could have been simultaneous with the collapse, as they are roughly parallel with the caldera elongation. Winter et al. (2008) distinguished coherent rhyolite and pyroclastic rhyolite dikes. The succession of these two facies indicates a subvolcanic feeding system that may have sourced the Teplice rhyolite.

2.2.4 Teplice Rhyolite

In the eastern third of the caldera, the Teplice rhyolite is exposed. It stretches all the way from the northern end in Germany to the southern one in Czechia (Fig. 2a). The maximum thickness reaches up more than 1 km. The exposure of these rocks is also described from the Teplice area (at Písečný vrch). Based on a geophysical survey, Mlčoch and Skácelová (2010) proposed the continuation of the Teplice rhyolite beneath the Cenozoic sedimentary and volcanic rocks.

A vast majority of the Teplice rhyolite rocks includes rhyolite to rhyodacite tuffs, voluminous ignimbrite bodies and lava flow and dome complexes (Fig. 2d). Individual volcanic rocks of the Teplice rhyolite are intercalated with two volcaniclastic and sedimentary layers including small coal anthracite seams (Fiala, 1960; Wetzel et al., 1985; Jiránek et al., 1987). A detailed description of the Teplice rhyolite is provided below in Chapter 3.

2.2.5 Ring dike system (granitporphyr)

In the shape of a horseshoe, the caldera is encircled by a ring dike system (Fig. 2a). The apparent width of dikes varies from hundreds of meters up to three kilometers. The rocks include porphyritic microgranite of various microstructural varieties with abundant plagioclase-mantled K-feldspars phenocrysts defining a rapakivi texture (Müller and Seltmann, 2002). In detail, the porphyritic microgranites can be divided into two rather differently fractionated types: GP I and GP II (Müller and Seltmann, 2002). The former is more acid and fractionated, with phenocrysts of K-feldspar, plagioclase and quartz and with quartzo-feldspatic fine-grained matrix, whereas the latter is less fractionated and more mafic with quartz-feldspar-hornblende granophyric matrix. The GP I type is relatively older, and is considered to be derived from more evolved parts of the caldera's stratified magma chamber, whereas the GP II is probably the result of mixing with another, more mafic

member. The GP I type can be found almost everywhere in the ring dike system, while GP II only in eastern segments (Müller and Seltmann, 2002).

Recently, Tomek et al. (2019) suggested that the porphyritic microgranite was emplaced synchronously with the caldera collapse. Their model suggests eruptions of the Teplice rhyolite draining the underlying magma chamber, while the collapsed caldera floor triggered remobilization and emplacement of a residual cumulate magma mush into the caldera ring fault (Fig. 2c).

2.2.6 Post-collapse granite stocks

Evolution of the Altenberg–Teplice caldera was terminated by the emplacement of multiple shallow-level A-type plutons and stocks. These magma bodies intruded both the Teplice rhyolite and the porphyritic microgranite ring dikes along the eastern rim and norther caldera third.

The largest exposed pluton is the Schellerhau granite (~5 × 3 km in the map) to the north of the central part of the caldera (Fig. 2b). Among others, there are much smaller stocks, namely Altenberg, Sadisdorf, Krupka, Preisselberg, and Cínovec granites (Fig. 2b). Other plutons that are not exposed at the present-day erosional level are Hegelshöhe, Schenkenshöhe, Knötl and Sachsenhöhe discovered by mining activity (e.g., Štemprok et al., 2003; Štemprok, 2016). Štemprok et al. (2003) suggested that the post-caldera evolution of these plutonic bodies originated from a rather different magma source than the relatively older Teplice rhyolite and the ring dike system. These granitic bodies probably represent residual late-stage melts, and are enriched by volatiles and incompatible components. Their already complex development was affected by hydrothermal alterations (Johan and Johan, 1994; Johan and Johan, 2005; Johan et al., 2012; Štemprok, 2016; Breiter et al., 2017).

3 Teplice rhyolite

3.1 General overview

Even though the Teplice rhyolite body is commonly referred to as a single unit, it shows remarkable variations in composition, microstructure, age and type of volcanic deposit across the whole exposed area. It includes rhyolite to rhyodacite fall tuffs, pyroclastic density current deposits and lava flows and domes. Unfortunately, as the Teplice rhyolite body is situated on the border of two countries, classification into so-called "petro-types" had occurred differently in each country, mostly by Lobin (1986) in Germany, and Fiala (1960), Eisenreich and Jeřábek (1978) and Jiránek et al. (1987) in Czechia.

On the German side, the rocks were intensively studied by Lobin (1986). Lobin (1986) distinguished eight individual "petro-types" of the Teplice rhyolite: Barmenberg, Schmiedeberg, Molchgrund, Buschmühle, Langer Grundbach, Teichweg, Lugstein and Altenberg (Fig. 2d). Similarly, as in the Czech part, these "petro-types" were described upon their petrographical characteristics. Among these "petro-types", two volcaniclastic layers were also recognized.

In the Czech part, the geological research was initiated by Fiala (1960), who divided the Teplice rhyolite into six types. After that, few other authors have been investigating this volcanic body. Geological mapping by Eisenreich and Jeřábek (1978) separated the Teplice rhyolite into seven "petro-types", usually based on their macroscopic appearance, the proportion of pumice, fiamme, crystals and lithic clasts, and other petrographical properties: Západní okraj (Western margin), Pramenáč, Vlčí kámen, Přední Cínovec, Medvědí vrch, Vrchoslav and Lysá hora. Most of these are ignimbrites, with minor fall tuffs for instance the Western margin, and lavas in the eastern margin of the caldera - the Lysá hora "petro-type". These authors assumed that the relative age decreases from the west to the east due to the eastward collapse of the caldera floor (Benek, 1991). This classification was later used in a complex study of Jiránek et al. (1987), where the authors summarize up-to-date knowledge at that time.

A borehole Mi-4 has been subject of many interests during the ore deposits prospecting. Breiter et al. (2001) explored the chemical evolution and petrography throughout the core and divided the volcanic rocks into five volcanic phases. (1) The first volcanic phase (the Basal Rhyolite) at depth 870.1–924.5 m comprises fall tuffs and ignimbrites. Sedimentary intercalations of arkose, sandstone, shale and coal are also present.

(2) The second volcanic phase includes dacite tuffs and ignimbrites (604.3–924.5 m), and together with the first volcanic phase is an equivalent of the Schönfeld–Altenberg volcano-sedimentary depression. (3) The third volcanic phase (TR 1; 493.4–601.6 m) corresponds to the basal portion of the Teplice rhyolite, and is represented by rhyolitic tuffs and ignimbrites with sedimentary horizon containing plant remnants in coal-bearing shale. (4) The fourth volcanic phase (TR 2) is divided into fall tuffs with lava clots (TR 2a; 412.9–490.6 m) overlain by ignimbrites (TR 2b; 412.9–191.4 m). This phase is likely an equivalent of the Western margin "petro-type" (Jiránek et al., 1987). (5) Fifth volcanic phase (TR 3; 0–191.4 m) includes three "petro-types": TR 3a – Pramenáč, TR 3b – Vlčí kámen and TR 3c – Přední Cínovec. The latter two are not present in the Mi-4 borehole but crop out at the surface. It is important to note, that this study has been using data only from one borehole, and the thickness of different phases can vary beneath the surface.

Recently, Gnojek et al. (2018) used airborne and ground gamma-ray spectrometry in order to approximately correlate the Czech and German classifications. Soon after that, Casas-García et al. (2019) applied multi-disciplinary research, including petrography and whole-rock geochemistry, which resulted into the final correlation of Teplice rhyolite on both sides of the border. Casas-García et al. (2019) introduced a new concept of lithofacies architecture, where the previously used "petro-types" are unified into well-defined lithostratigraphic members. Their final lithofacies succession includes nine individual members and two intercalating volcanoclastic and sedimentary horizons: (1) Barmenberg, (2) Schmiedeberg, (a) sedimentary horizon I, (3) Buschmühle, (b) sedimentary horizon II, (4) Teichweg, (5) Altenberg, (6) Lugstein-Pramenáč, (7) Vlčí kámen-Medvědí vrch, (8) Přední Cínovec and (9) Lysá hora (Fig. 2d; Casas-García et al., 2019).

Moreover, Casas-García et al. (2019) interpreted that the Teplice rhyolite evidenced three main eruptions phases. First (Barmenberg and Schmiedeberg) and second (Buschmühle) eruption opened and cleared vents, producing lithic-rich ignimbrites, while the third eruption (from Teichweg to Lysá hora) recorded a waxing phase with massive and voluminous, crystal-rich (nevaditic) ignimbrites followed by emplacement of lava flows and domes. They suggested that lithological evidence indicates partial to complete welding during hot emplacement and progressive aggradation of deposited volcanic rocks.

Apart from the caldera interior, correlative ignimbrites were identified south of the caldera in Oparno valley (Casas-García et al., 2019), in few boreholes such as Tř 1 (near Tŕťeno; Opluštil et al., 2016) and GTPV-LT1 (Litoměřice; Žáček and Škoda, 2009; Šafanda et al., 2020), and as xenoliths in Cenozoic volcanic rocks in the Velemín area (V.

Rapprich, personal communication). Recently, Tomek et al. (under review) proposed that the Bělka tuff, a layer identified across the Central and Western Carboniferous sedimentary basins, is a product of an eruption from the Altenberg–Teplice caldera.

3.2 Lithofacies architecture

In this chapter, I illustrate the lithofacies architecture from the relatively oldest to youngest rhyolite members based on the interpretation proposed by Casas-García et al. (2019).

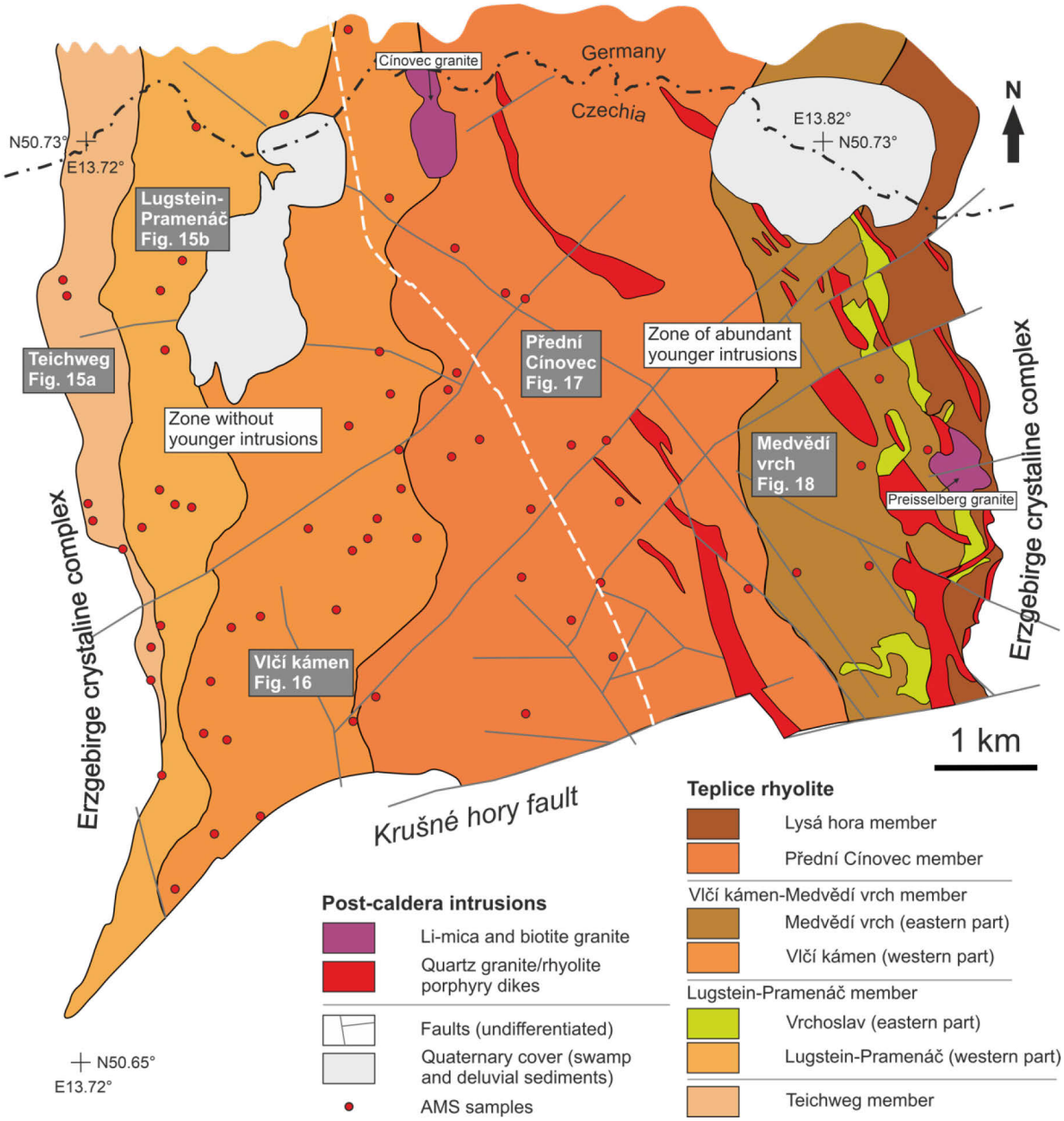

Fig. 3 Geological map of the Czech part of the Teplice rhyolite based on 1:25.000 geological maps of the Czech Geological Survey (Jiránek, 1991; Schovánek, 2004a, 2004b). Lithostratigraphic members correspond to the new classification of Casas-García et al. (2019).

(1) Exposed in the northernmost part of Teplice rhyolite, crystal-rich Barmenberg is the oldest member. However, it is not certain whether it´s geochemically affinity is an equivalent either to the Schönfeld-Altenberg complex or to the Teplice rhyolite. Therefore, Casas-García et al. (2019) interpreted the Barmenberg as a transitional member.

(2) The overlying Schmiedeberg member is further divided into the Schmiedeberg A (laterally changing ignimbrite from crystal-rich to lithic-rich) and the Schmiedeberg B (lava flows) overlain by a thin sandstone layer (horizon I) representing a volcanic quiescence.

(3) The Bushmühle member also comprises two sub-members A and B, with similar characteristics as the Schmiedeberg (A – laterally changing ignimbrites; B – lava flows/domes). This sequence is overlain by a sedimentary horizon II (another volcanic quiescence), comprising fluvial conglomerates and charcoal-bearing sandstone. Importantly, both horizons I and II are traceable throughout the Teplice rhyolite and therefore Casas-García et al. (2019) interpreted them as volcanic quiescence episodes separating the three major eruption phases.

(4) The Teichweg member is composed of two slightly geochemically distinctive parts: the former Western Margin and the Langer Grundbach "petro-types". However, based on the gamma-ray spectrometry, Gnojek et al. (2018) did not find good correlations between these two either.

(5) In a small area next to Altenberg, lithic-rich ignimbrite of the Altenberg member is exposed. Based on geochemistry, this Altenberg member does not correlate with other members.

Another three members are all crystal rich (nevaditic), and petrographically similar. From stratigraphic bottom to top, these are represented by (6) Lugstein-Pramenáč, (7) Vlčí kámen-Medvědí vrch member and (8) Přední Cínovec.

Note that Casas-García et al. (2019) connected the former separate Vlčí kámen and Medvědí vrch "petro-types" into one member. Without any structural evidence, Casas-García et al. (2019) interpreted the former "petro-types" Vlčí kámen and Medvědí vrch as representing two limbs of a syncline, while the Přední Cínovec member crops out in the center of this syncline. This imply that the Přední Cínovec should be relatively younger than the Medvědí vrch "petro-type", which is in variance with classical interpretation by Eisenreich and Jeřábek (1978) and Jiránek et al. (1987).

(9) The relatively youngest Lysá hora member is somehow different and is formed by lava flows and domes alongside the eastern margin of the Altenberg–Teplice caldera.

3.3 Teplice rhyolite members – focus of this study

Particular members of the Teplice rhyolite that crop out mostly at the southern flank of the Krušné hory/Erzgebirge Mts. on the Czech side of the border are presented below in greater detail, as they are the principal subject of this study; these include: Teichweg, Lugstein-Pramenáč, Vlčí kámen-Medvědí vrch, and Přední Cínovec member (Figs. 2a and 3). Other members are not sufficiently exposed for an AMS study. I have further divided the Vlčí kámen-Medvědí vrch member into western and eastern part (former names are used), in order to analyze the data more easily. The studied area of the Teplice rhyolite illustrated in the Figure 3 is divided into eastern and western zones. The former is intensely intruded by younger post-caldera microgranite dikes and granite stocks, whereas the latter is intrusion free.

Hereafter, the description of these members is a combination of my own field works, observations of Jiránek et al. (1987) and Casas-García et al. (2019), and explanatory comments to the geological maps by Schovánek et al. (2004).

3.3.1 Teichweg member

In the westernmost part of the Teplice rhyolite, the Teichweg member is exposed in a relatively thin ~N–S elongated area (Fig. 3). At two large outcrops in the Czech part, basal fall tuffs are overlain by ignimbrites (Fig. 4a). These tuffs are very fine-grained showing a typical layering, which dips 20° to 40° to the east (Jiránek et al., 1987). The mean orientation of layering calculated from measured data is 068°/27°. Note, that dip direction and dip for planar structures, and trend and plunge for linear structures is used throughout the thesis.

Above the fall tuffs, the ignimbrites display apparent foliation defined by elongated greenish fiamme (Fig. 4b–d) representing a characteristic feature that distinguishes the Teichweg from the other Teplice rhyolite members (see below). This white to pale shadow rock is poor in crystals (compared to other members), however, it is more abundant in juvenile pumice and lithic clasts (host rock gneisses). Quartz and K-feldspar crystals are usually hypidiomorphic; the latter is often kaolinized. Sericitized plagioclase is present in lesser amounts. Matrix is formed by compacted ash, mostly devitrified, forming welded and fluidal microstructures.

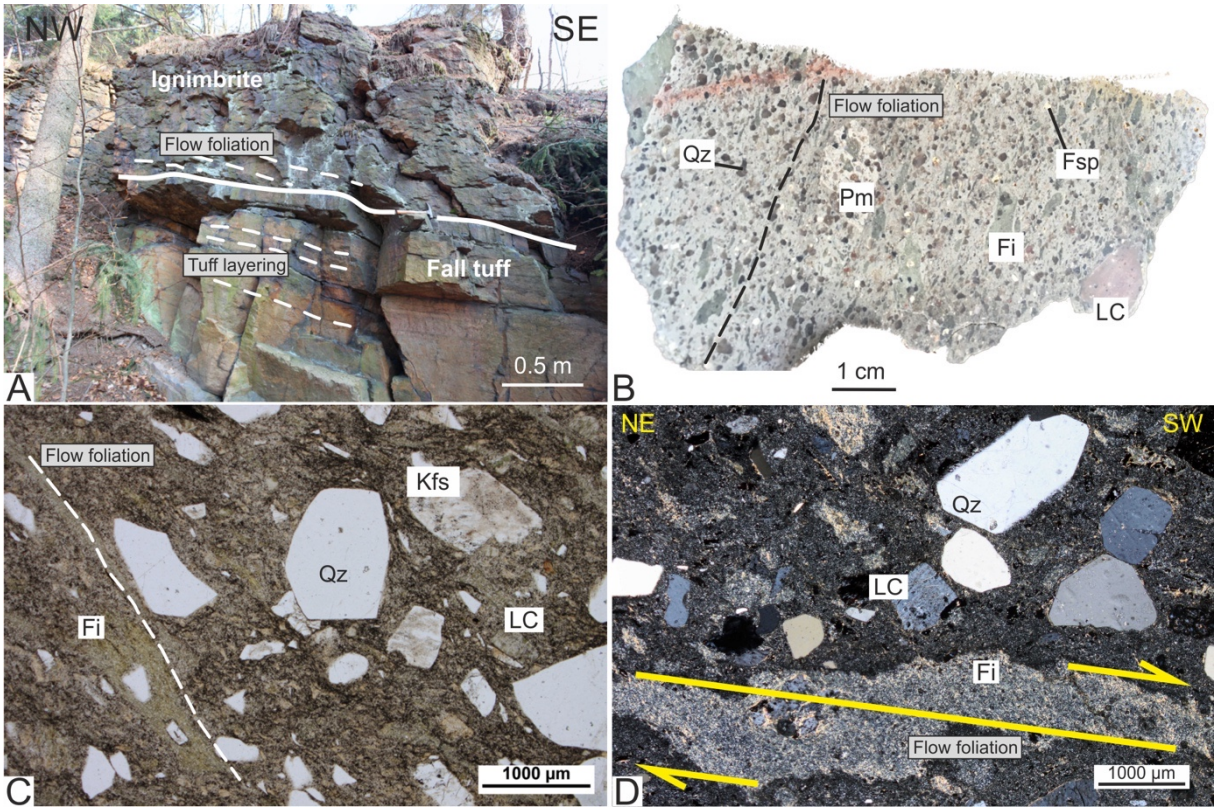

Fig. 4 The Teichweg member: a) station FT001 showing flat-lying contact between ignimbrites deposited on fall tuff; b) image of an ignimbrite rock slab at station FT105; c) plane and d) cross-polarized microphotographs of the ignimbrite, station FT001. Note the apparent flow foliation. Fi – fiamme; LC – lithic clast; Pm – pumice; Qz – quartz; Kfs – K-feldspar. Mineral abbreviations are after Whitney and Evans (2010) are used throughout the thesis.

3.3.2 Lugstein-Pramenáč member

The Lugstein-Pramenáč member forms pronounced morphological elevation inside the Teplice rhyolite area in form of small rock cliffs on the southern flank of the Krušné hory/Erzgebirge Mts. Such outcrops very often display subvertical to subhorizontal cooling columnar jointing with various plunge (Fig. 5a). The orientation of cooling joints will be discussed below.

This member includes massive, reddish to brownish ignimbrite containing abundant phenocrysts, which form more than 40% of the rock (Fig. 5b). The K-feldspar is more abundant than quartz, and about two times more abundant than plagioclase. K-feldspar and quartz are sometimes almost fully idiomorphic. Feldspar often shows kaolinization while plagioclase sericitization. In detail, the devitrified glassy matrix of the ignimbrite displays visible, sometimes recrystallized pseudofluidal microstructures as well as opaque minerals (Fig. 5c and d).

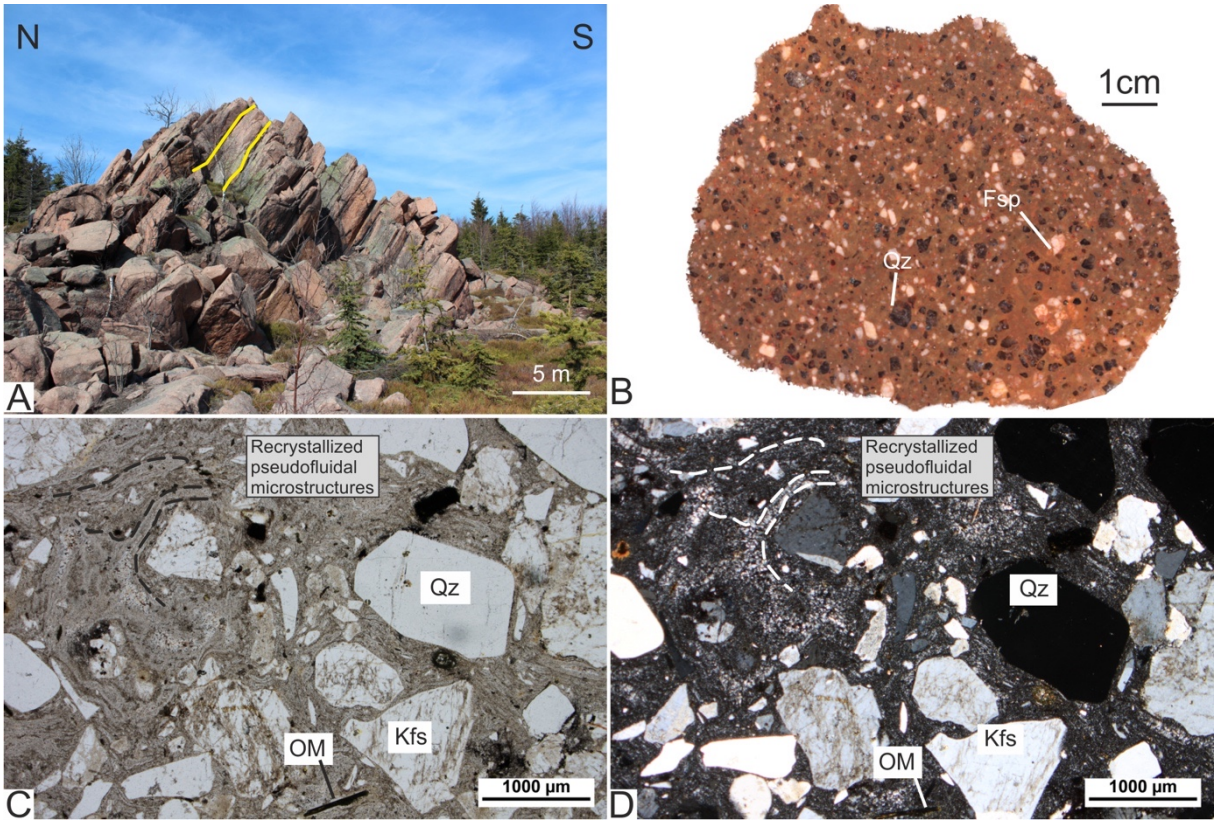

Fig. 5 The Lugstein-Pramenáč member: a) station FT004 showing subvertical columnar jointing; b) image of an ignimbrite rock slab at station PV006; c) plane and d) cross-polarized microphotographs of the ignimbrite, station FT090. OM – opaque minerals; Qz – quartz; Kfs – K-feldspar.

3.3.3 Vlčí kámen-Medvědí vrch member – Vlčí kámen

The Vlčí kámen similarly as the Lugstein-Pramenáč crops out on the southern flank of the Krušné hory/Erzgebirge Mts, whereas its northern portion lacks outcrops, and is partly covered by a swamp (Fig. 3). At few available outcrops, columnar jointing is measurable, not resulting in any preferred direction (Fig. 6a).

The Vlčí kámen includes nevaditic ignimbrites showing phenocrysts dominance over matrix (Fig. 6b). Apart from quartz and K-feldspar, the Vlčí kámen is also rich in altered pyroxene. The ash matrix shows also recrystallized pseudofluidal microstructure (Fig. 6c and d).

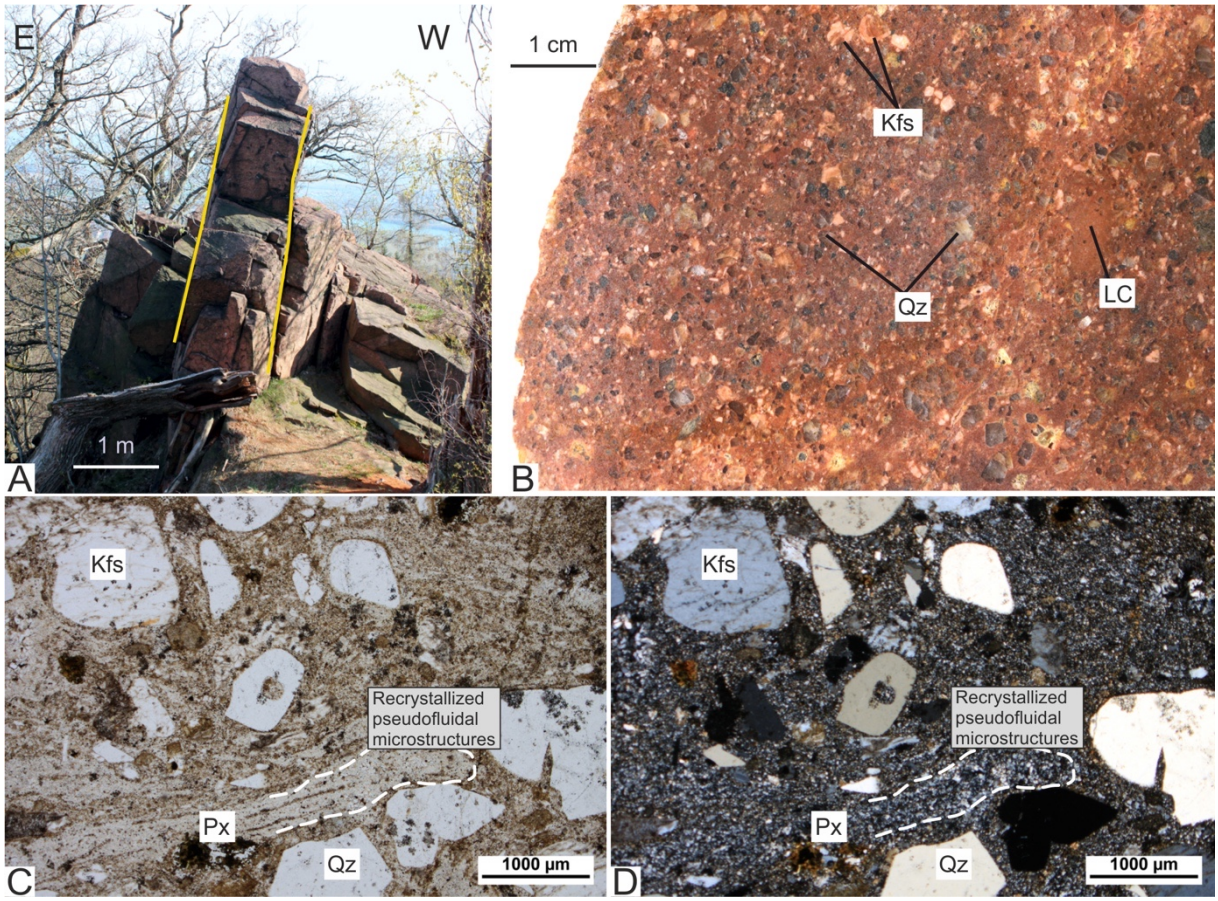

Fig. 6 The western part of the Vlčí kámen-Medvědí vrch member, formerly Vlčí kámen: a) station FT009 showing subvertical columnar jointing. Yellow curves are delineating columnar jointing. b) Image of an ignimbrite rock slab at station FT033; c) plane and d) cross-polarized microphotographs of the ignimbrite, station FT089. LC – lithic clast; Qz – quartz; Kfs – K-feldspar; Px – pyroxene.

3.3.4 Přední Cínovec

The Přední Cínovec member is very similar to both Vlčí kámen and Medvědí vrch "petrotypes". It is composed of reddish nevaditic ignimbrite with abundant phenocrysts dominating over matrix (Fig. 7a, b). This member is likely an equivalent of outflow facies cropping out in the Kubo quarry in the Oparno valley (Casas-García et al., 2019) and was identified in boreholes Tř-1 and GTPV-LT1 (Žáček and Škoda, 2009; Opluštil et al., 2016; Šafanda et al., 2020). Columnar jointing is rather sparse, instead this member shows sets of several fracture patterns (Fig. 7a). The northern and eastern portion is intruded by several microgranite dikes and the Cínovec pluton (Fig. 3).

The microstructure includes (in volume decreasing order) quartz, kaolinized K-feldspar, sericitized plagioclase and altered pyroxene phenocrysts (Fig. 7c, d). In addition, large (~1 mm) biotite grains and abundant opaque minerals are embedded in a devitrified glassy matrix. Locally, recrystallized pseudofluidal microstructures are visible adjacent to some larger phenocrysts.

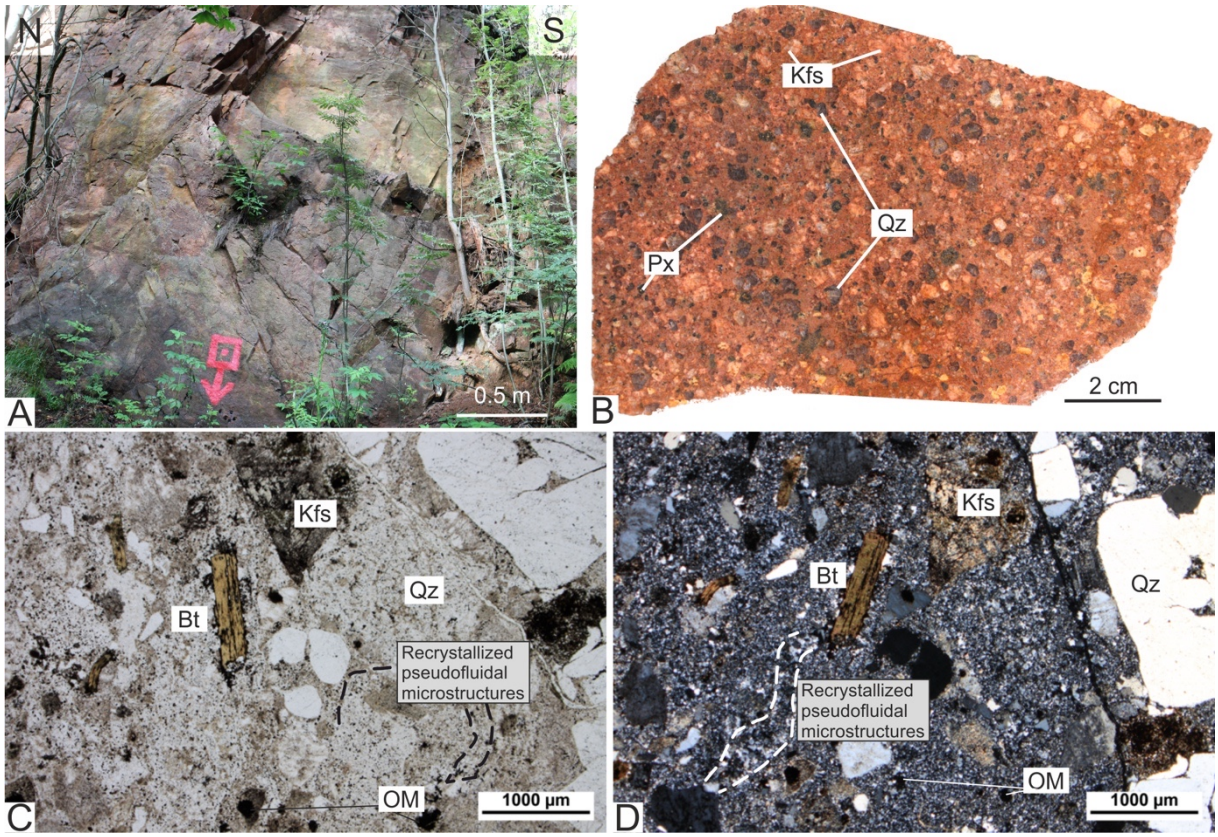

Fig. 7 The Přední Cínovec member: a) an outcrop photography of station FT027; b) image of an ignimbrite rock slab at station FT081; c) plane and d) cross-polarized microphotographs of the ignimbrite, station FT084. OM – opaque minerals; Qz – quartz; Kfs – K-feldspar; Px – pyroxene; Bt – biotite.

3.3.5 Vlčí kámen-Medvědí vrch member – Medvědí vrch

The western part of the Vlčí kámen-Medvědí vrch member is situated on the contact with Lugstein-Pramenáč to the West and Lysá hora members to the east and is intensely intruded by microgranite dikes and Preiselberg–Krupka granite (Fig. 3). This area is poorer in outcrops; they are usually small and not always in-situ (Fig. 8a). I have not sampled outcrops where I was not sure if they were in-situ.

The ignimbrite is characterized as reddish to pale brown showing apparent nevaditic texture. Macroscopically visible crystals of quartz, K-feldspar, but also opaque minerals are present (Fig. 8b). In addition, this member has abundant lithic gneiss clasts (~1 cm), which is not a typical feature of its western equivalent – the Vlčí Kámen (Fig. 8c and d). Recrystallized pseduofluidal microstructures are also present (Fig. 8c).

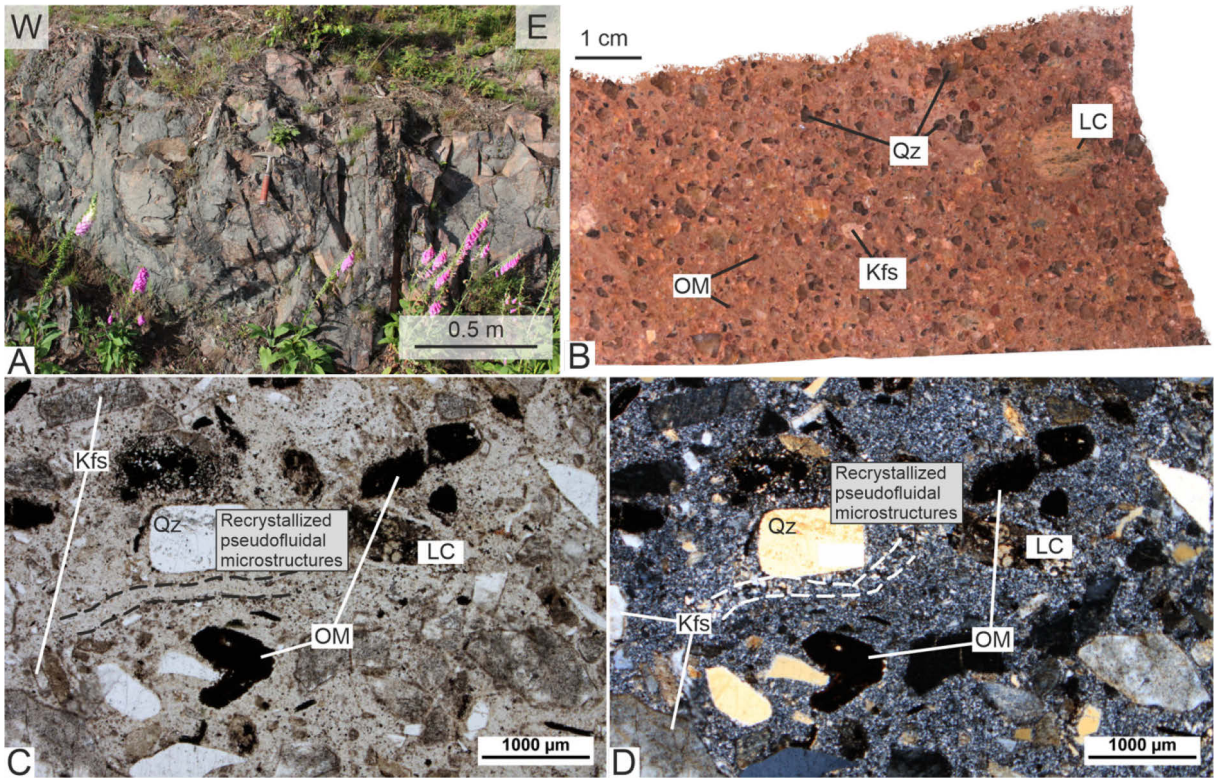

Fig. 8 Eastern part of the Vlčí kámen-Medvědí vrch member, formerly Medvědí vrch: a) an outcrop photography of station FT016; b) image of an ignimbrite rock slab at station PV021; c) plane and d) cross-polarized microphotographs of the ignimbrite, station FT019. LC – lithic clasts; OM – opaque minerals; Qz – quartz; Kfs – K-feldspar.

4 Methodology

4.1 Anisotropy of Magnetic Susceptibility – theory

One of the natural magnetic properties of materials including rocks and minerals is the magnetic susceptibility. The susceptibility can be defined as an ability of a material to get magnetized in a magnetic field. This provides a base for the Anisotropy of magnetic susceptibility (AMS) as most of the minerals yield different magnitude of susceptibility along their crystallographic axes (crystallographic anisotropy) or along their elongation (shape anisotropy). The AMS is thus a useful structural geology method quantifying internal fabrics of rocks (e.g., Hrouda, 1982; Hrouda and Kahan, 1991; Tarling and Hrouda, 1993; Borradaile, 2001; Borradaile and Jackson, 2010).

The magnetic susceptibility (k) is described by an equation $k = M/h$, where M [A/m] is the magnetization of material, and h [A/m] is the magnetic field. In this thesis, SI units are used. In three-dimensional space, the AMS can be mathematically defined as a second-rank tensor with principal components of the matrix k_1 (maximum principal susceptibility), k_2 (intermediate principal susceptibility) and k_3 (minimum principal susceptibility). Graphically, the AMS tensor can be represented by a triaxial ellipsoid with the principal susceptibility axes $k_1 \geq k_2 \geq k_3$ (Fig. 9). For expressing the orientation of magnetic fabrics, magnetic lineation (k_1 axis) and magnetic foliation (k_1–k_2 plane) are used (Fig. 9). In addition, the degree (intensity) of magnetic lineation L and foliation F is calculated as $L = k_1/k_2$ *and* $F = k_2/k_3$, respectively.

In AMS fabric studies, several other parameters are normally used: (1) mean (bulk) susceptibility k_m, (2) degree of anisotropy P and (3) shape parameter T. (1) The mean (bulk) susceptibility reflects volume fraction and type of magnetic minerals in the rock and is defined by equation $k_m = (k_1 + k_2 + k_3)/3$. Rock magnetic properties with respect to k_m values are provided below. (2) The degree of anisotropy is a ratio of maximum and minimum susceptibilities; $P = k_1/k_3$. It indicates the eccentricity of an AMS ellipsoid and can be related to intensity of magnetic fabrics (Nagata, 1962). For instance, if $P = 1$, then the ellipsoid of magnetic susceptibility is isotropic (i.e. is a sphere). If $P = 1.01$ and 1.10, the fabric intensity is 1 and 10%, respectively. (3) Symmetry of the AMS ellipsoid is then defined by the shape parameter ($T = 2ln(k_2/k_3)/ln(k_1/k_3) - 1$). This parameter ranges from –1 to 1. For negative values is the ellipsoid prolate ($k_1 \gg k_2 \geq k_3$). When $T = 0$, the shape of the AMS ellipsoid is neither prolate nor oblate (triaxial or neutral; $k_1 > k_2 > k_3$), and for $T >$

0 ($k_1 \geq k_2 \gg k_3$) is the ellipsoid oblate (Tab. 1; Hrouda, 1982; Hrouda and Kahan, 1991; Tarling and Hrouda, 1993; Borradaile, 2001; Borradaile and Jackson, 2010). Mean values of magnetic foliations (dip direction/dip), lineations (trend/plunge) and AMS scalar parameters are calculated based on Jelinek statistics from at least 5 individual specimens collected at one sampling station (Jelínek, 1981).

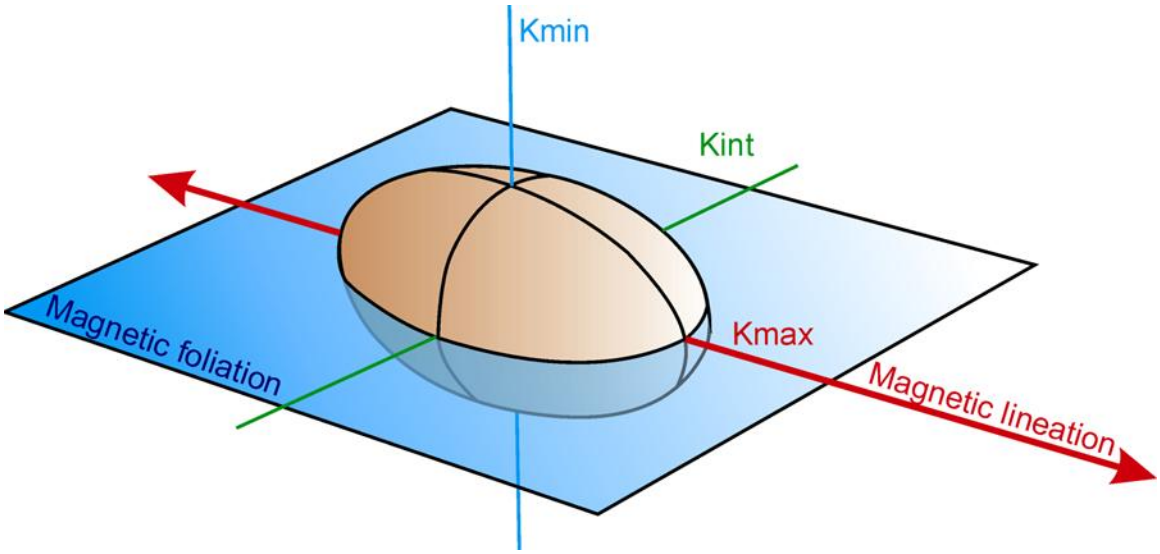

Fig. 9 Ellipsoid of magnetic susceptibility. Three principal axes are presented: Kmax = $k_1 \geq$ Kint = $k_2 \geq$ Kmin = k_3, together with magnetic foliation (pole to k_3) and magnetic lineation (k_1).

Parameter	Name	Equation
k_1	Maximum principal susceptibility	
k_2	Intermediate principal susceptibility	
k_3	Minimum principal susceptibility	
k_m	Mean (bulk) susceptibility	$k_m = (k_1+k_2+k_3)/3$
P	Degree of anisotropy	$P = k_1/k_3$
T	Shape parameter	$T = 2\ln(k_2/k_3)/\ln(k_1/k_3) - 1$
F	Magnetic foliation degree	$F = k_2/k_3$
L	Magnetic lineation degree	$L = k_1/k_2$

Tab. 1 Summarization of the Anisotropy of magnetic susceptibility parameters and their equations.

Calculation of the AMS tensor rises from all rock components (i.e., minerals). Generally, all materials (minerals) can be sorted into three groups, based on their magnetic properties: (1) ferromagnetic; (2) paramagnetic and (3) diamagnetic. (1) Ferromagnetic materials respond very well to the applied magnetic field. Their susceptibility k is theoretically between 10^{-2} and 10^{0} SI. Ferromagnetic minerals are for example magnetite, maghemite, hematite, and other Fe-Ti oxides. A better description of the complex

ferromagnetic behavior of these materials is by hysteresis loops. (2) Paramagnetic materials have weaker susceptibility than materials ferromagnetic ranging from 10^{-4} to 10^{-2} SI. Main rock-forming paramagnetic minerals are biotite, amphibole, olivine, pyroxene, muscovite and others. Together with diamagnetic materials, both do not sustain remanent magnetization. (3) In the last group are diamagnetic materials (minerals: e.g., quartz, calcite). Diamagnetic materials react differently to the applied magnetic field, and that is very weakly and negatively. That means their susceptibility is also negative ($k < 0$), on the order of -10^{-5} SI.

In bulk rock susceptibility, we have to take into consideration that the same amount of different minerals has different contributions to it. For instance, 0.01% of magnetite have the same contribution as 100% of biotite in a rock sample (Fig. 10; Hrouda and Kahan, 1991).

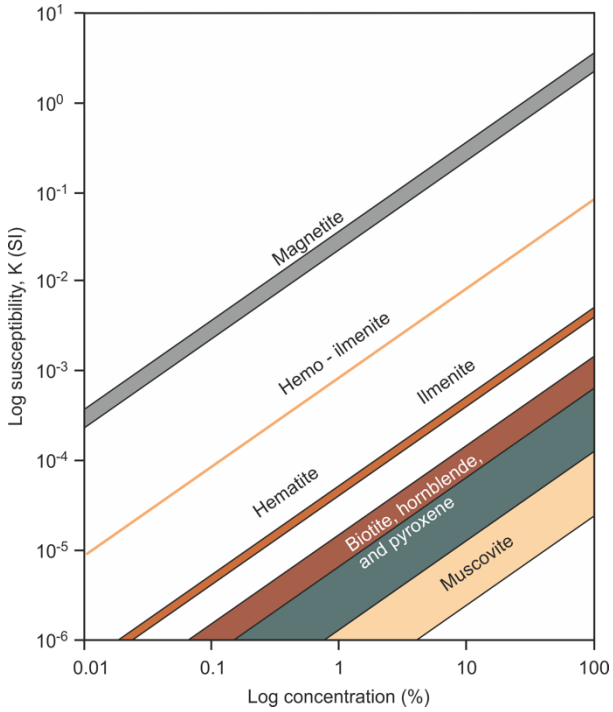

Fig. 10 Logarithmic diagram of mineral contribution to the whole rock susceptibility depending on their concentrations (after Hrouda and Kahan, 1991).

Anisotropy of magnetic susceptibility in minerals is further divided into two groups due to their crystallographic structure. Either they are (1) cubic with shape anisotropy or (2) others with crystallographic anisotropy. In case (1), principal axes of magnetic anisotropy ellipsoid correspond to longest, intermediate and shortest dimensions of a mineral (e.g., Grégoire et al., 1998). This group is represented by titanomagnetites. In case

(2), the anisotropy is reflected by the mineral's crystallographic structure, which corresponds to most rock-forming minerals except titanomagnetites (e.g., Richter et al., 1993).

For identification of bulk rock AMS signal, magnetic susceptibility variations with temperature are commonly measured. The results are thermomagnetic curves, where the bulk susceptibility is measured from ca. –195 °C (liquid nitrogen temperature) to 700 °C and back. The behavior and shape of the curve then help to identify the dominant carrier of the AMS signal. For example, a box-like shaped curve is commonly shown by magnetite, with a Verwey transition (at ca. –150 °C) and Curie temperature (T_c at ca. 580 °C), while hyperbolic curves (susceptibility decrease with temperature increase) are typical for paramagnetic minerals.

Magnetic fabrics of (titano)magnetite are, however, also dependent on the grain size, as the decreasing size may be reducing the number of magnetic domains (multi-domain), with small grains having only one domain (single domain). This variation between single-domain (SD) and multi-domain (MD) magnetite grains has a different influence on the final magnetic fabric (e.g., Butler and Banerjee, 1975; Potter and Stephenson, 1988; Clark, 1997; Soriano et al., 2016). Normally, large enough grains show multi-domain behavior, which results in k_1 axis parallel to easy magnetization (remanent) axis. On the other hand, single-domain grains have k_1 axis perpendicular to the easy magnetization axis. Thus, such magnetic fabrics are referred to as inverse, while a mixture of SD and MD grains correspond to anomalous fabrics, and dominance of MD grains reflects normal fabrics (e.g., Potter and Stephenson, 1988; Rochette et al., 1992, 1999; Soriano et al., 2016).

4.2 AMS fabrics of pyroclastic density currents

Due to violent nature and high-energy eruption dynamics, the internal dynamics of pyroclastic density currents (PDC) can be studied almost exclusively through their deposits at the present-day erosion level. In order to depict source vents and flow direction, different methods can be applied. In petrography, flow direction in ignimbrites have been determined by Elston and Smith (1970) using petrographic indicators such as the clast imbrication, preferred orientation of shaped glass shards (fork-shaped, etc.), or the blocking effect (larger grains provide "flow shadow" to the smaller ones). Usage of the AMS and application of magnetic fabrics, on the other hand, may reveal invisible structures, and may be often used as an independent flow indicator in addition to conventional petrographical

markers (e.g., MacDonald and Palmer, 1990; Fisher et al., 1993; Baer et al., 1997; Ort et al., 1999, 2003; LaBerge et al., 2009; Agrò et al., 2015; Willcock et al., 2015; Moncinhatto et al., 2019). However, the magnetic fabrics only record processes that occurred immediately before deposition, therefore representing the last strain increment before rock solidification/cooling (e.g., Baer et al., 1997; Paterson et al., 1998).

The most common parameters, that are examined in order to interpret the magnetic fabrics in ignimbrites are magnetic foliation and lineation. The plunge of the magnetic foliation (k_1–k_2 plane; usually subhorizontal) may correspond to grain imbrication while the magnetic lineation (well-clustered k_1; usually subhorizontal) is often parallel to the flow axis (e.g., MacDonadl and Palmer, 1990; Ort et al., 1999, 2003; LaBerge et al., 2009). PDCs have been divided generally into (1) proximal and (2) distal zones with respect to the relationship between distance from the source and characteristic AMS fabrics. (1) Proximal and near vent zone, where the flow is turbulent and chaotically changes its directions, shows oblate magnetic fabric (strongly clustered k_3 axes*)* without significant lineation (none to weak k_1 clustering). (2) The distal zone ignimbrites form a well-clustered magnetic foliation dipping towards the direction of the source associated with a parallel plunge of the well clustered magnetic lineation. This pattern defines a magnetic fabric recording the ash-flow imbrication (e.g., Knight and Walker, 1986; Baer et al., 1997; Ort et al., 1999, 2003; Agrò et al., 2015). Recently, Agrò et al. (2015) and Moncinhatto et al. (2019) suggested three different classes for the AMS fabrics based on the relation between the dip direction and plunge of subhorizontal magnetic foliation (k_1–k_2 plane) and lineation (k_1), respectively: (1) parallel (<35°); (2) oblique (35°–55°) and (3) transverse (>55°). Ort et al. (2003) have described k_1 axis being sometimes near-perpendicular and perpendicular to the flow direction (the case of *transverse fabric*). The authors explain that this happens when magnetic grains in a turbulent current are rolled with their k_1 axis perpendicular to flow direction. Platzman et al. (2020) determined that in a thick and voluminous single ignimbrite flow unit, cooled margins depict shallowly dipping oblate magnetic fabrics whereas hot-emplaced interior displays somewhat steeper prolate fabrics.

4.3 Locality and sampling strategy

The area of the Teplice rhyolite on the southern flank of the Krušné hory/Erzgebirge Mts. was examined during several weeks of fieldwork campaigns that were conducted throughout my first year of Master studies. During these campaigns, a total of 63 sampling

station was drilled for the AMS measurements. These stations were subjected to detailed geological and structural mapping (see Appendix A). In addition, 25 representative thin-sections were prepared and examined with a conventional optical polarizing microscope in order to study the rock petrography (Figs. 4–8, panels c and d).

4.4 Sources of data and their measurement

The AMS samples were drilled in situ using a portable gasoline hand-held drill or collected as oriented block samples in remote areas. The latter were later drilled perpendicularly to the oriented plane in the laboratory of the Institute of Geology of the Czech Academy of Sciences. The orientation of drilled cores was then recalculated accordingly. Drill cores were then cut into a total of 1232 standard cylinders specimens, each 2.1 cm long and 2.5 cm in diameter. This corresponds to an average of ~20 specimens per station. A total of eleven representative samples were selected and prepared for the thermomagnetic experiments. All measurements were conducted in the Laboratory of Rock Magnetism at the Institute of Geology and Paleontology, Faculty of Science, Charles University. AMS data were obtained via a MFK–1A Kappabridge equipped with a 3D rotator. The susceptibility dependence on temperature data were acquired using connected apparatuses CSL and CS-4, in an argon atmosphere to minimize oxidation during heating. Final data plots and diagrams were calculated and processed in an AGICO Anisoft 5 and Cureval 8 software (freely available through www.agico.com). The full AMS data are presented in Appendix B.

5 Results

5.1 Mean (bulk) susceptibility

Variations in mean susceptibility for the Teichweg member (tuff and ignimbrite) are almost evenly distributed between 35 and 465 × 10^{-6} SI for individual specimens (Fig. 11a). Sixty-seven out of 167 measured specimens are concentrated in the area of 50–100 × 10^{-6} SI, while the rest is scattered without any preferred values. For the Lugstein-Pramenáč member, susceptibilities are distributed from 83 to 3650 × 10^{-6} SI. Out of 213 specimens, 67 have paramagnetic (<500 × 10^{-6} SI), 103 have moderately ferromagnetic (500–2500 × 10^{-6} SI), and 43 have strongly ferromagnetic susceptibilities (>2500 × 10^{-6} SI). The Vlčí kámen (443 specimens) yielded also a wide spectrum of k_m values of 59–3096 × 10^{-6} SI; yet paramagnetic susceptibilities (281 specimens) are more frequent than moderately ferromagnetic (133 specimens) and strongly ferromagnetic (29 specimens; Fig. 11a). The range of the Přední Cínovec member k_m values is the widest among the Teplice rhyolite, starting at 40 × 10^{-6} SI and reaching up to 6971 × 10^{-6} SI for individual specimen values. Out of the total number of 347 specimens, 87 are showing paramagnetic values, while the rest is either moderately ferromagnetic (113 specimens) or strongly ferromagnetic (147 specimens). The Medvědí vrch yielded 62 paramagnetic values that do not reach over 332 × 10^{-6} SI (lowest at 30 × 10^{-6} SI), with two main peaks between 50–100 (15 samples) and 200–300 × 10^{-6} SI (29 samples; Fig. 11a).

5.2 Thermomagnetic curves

The Teichweg member was measured on four representative samples: one from underlying tuff (FT105A), and three from the ignimbrite (FT001B, FT003, FT024). Stations FT105A and FT003 indicate the hyperbolic curve of decreasing susceptibility from the temperature of liquid nitrogen to ~450 °C. This is followed by a slightly steeper decrease of magnetic susceptibility down to 700 °C. The course of these thermomagnetic curves is nearly reversible, with susceptibilities within the 10^{-6} to 10^{-4} orders of magnitude (Fig. 12). Station FT001B starts its heating curve with a hyperbolic decrease, which then continues until 700 °C. After that, the cooling curve is commenced by a slight decrease of susceptibility below zero, followed by a steep increase with a Curie temperature (T_c) at ~495 °C and topmost susceptibility at ~430 °C. During gradual decrease of temperature, the curve

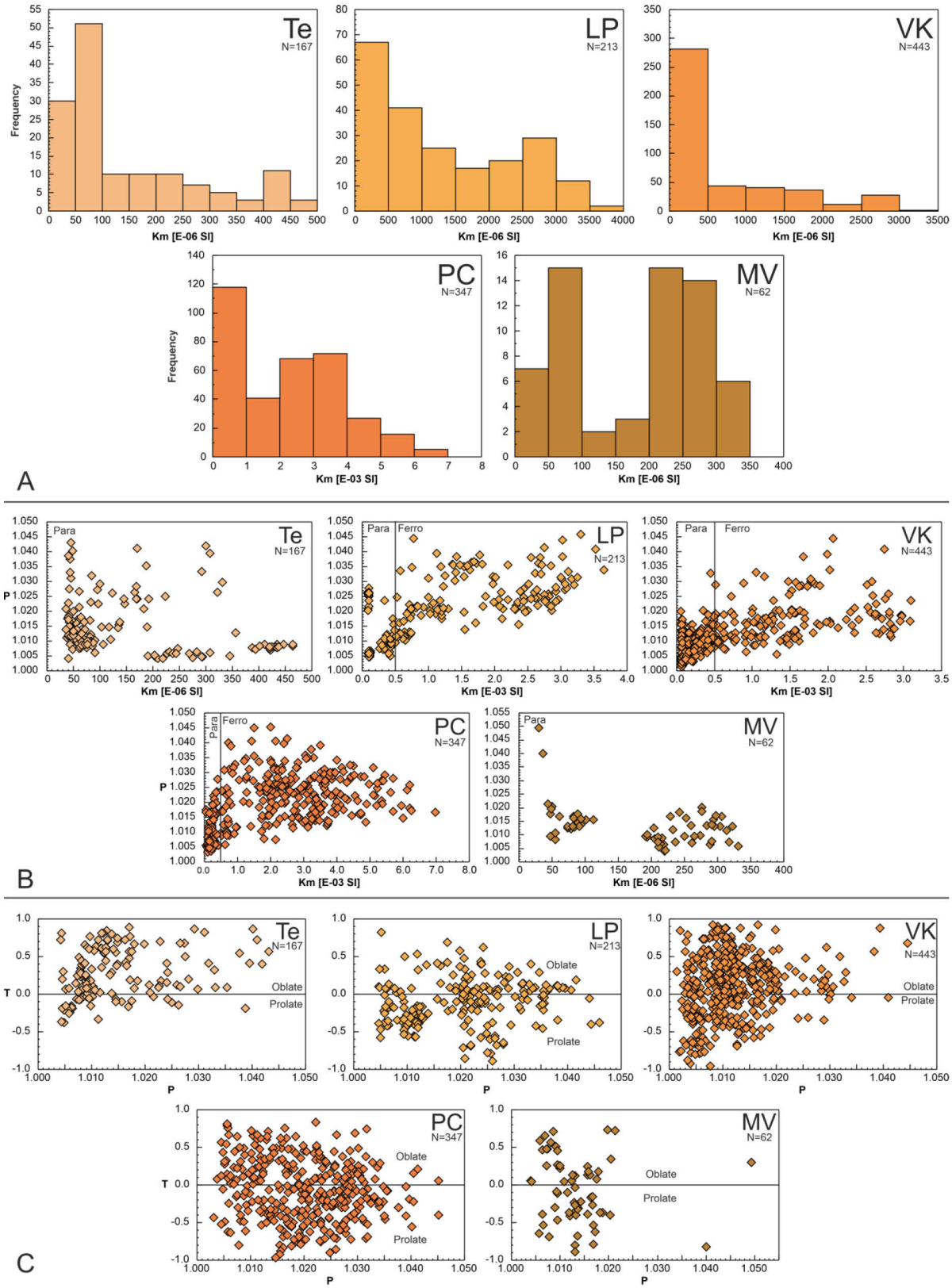

Fig. 11 a) Histograms of mean (bulk) susceptibility (k_m); b) diagrams of the degree of anisotropy (P) versus mean (bulk) susceptibility (k_m); c) Jelinek diagram showing shape parameter (T) versus degree of anisotropy (P). Te – Teichweg member, LP – Lugstein-Pramenáč member, VK – former Vlčí kámen "petro-type", PC – Přední Cínovec member, MV – former Medvědí vrch "petro-type"; Para – paramagnetic susceptibility field; ferro – ferromagnetic susceptibility field.

reaches a local minimum at ~110 °C (Fig. 12). Sample FT024 has a steep decrease in k_m values in the increase of the first few tens of degrees, then changes into a slow decline with a minimum (negative values) at 310 °C. After that, it increases up to an abrupt drop at temperatures of ~545 °C (with a T_c at ~560 °C) until 700 °C. On the cooling curve, the start of the temperature decrease is accompanied by a steep increase in susceptibility down to ~440 °C (T_c at ~510 °C). During the temperature decrease, k_m first decreases too, but around ~220 °C it changes the course and rises up until the liquid nitrogen temperature is reached (Fig. 12).

From the Lugstein-Pramenáč member, two stations (FT006 and PV004) were measured. For the heating curve of station FT006 sampling station, a sharp Verwey transition appears at ca. –150 °C (k_m ~1730 × 10^{-6} SI), followed by a slight decrease of susceptibility up to ca. –60 °C and a flat pattern until ~350 °C. After that, a graduate increase of k_m until ~520 °C is followed by an abrupt drop of susceptibility up to 700 °C with a T_c of 568 °C (Fig. 12). During cooling, the curve follows approximately the same path, but exhibits over about 1000 × 10^{-6} SI higher susceptibilities. Both PV004 curves (heating and cooling) follow the course of FT006 values (with first Verwey transition with ca. –150 °C and ~2560 × 10^{-6} SI), however, showing a significant hump on the heating curve between ~140–400 °C (Fig. 12).

Both the Vlčí kámen thermomagnetic curves (FT009 and FT050) have a similar course operating in just slightly different k_m values. For both heating curves, a Verwey transition is around ca. –150 °C, where FT009 yields k_m around ~420 × 10^{-6} SI, and FT050 indicates ~240 × 10^{-6} SI. Curie temperature is again very similar for both stations at ~570 °C (Fig. 12). Cooling curves rise above the heating ones, to about ten times higher susceptibilities, with FT009 having lower susceptibility by more than ~200 × 10^{-6}. Curie temperatures of the cooling curves are ~540–550 °C. An abrupt decrease at ~530 °C (for FT050) and ~490 °C (for FT009) is followed by a declining course of the curve until reaching a turning point at ~150 °C. The only difference is a hump of the FT050 curve, between ca. 340–490 °C, with maximal values at ~440 °C. Both curves then lead to a Verwey transition similarly at ca. –150 °C (Fig. 12).

Representative samples for susceptibility vs. temperature variation of the Přední Cínovec member are PV017 and PV020. For both heating curves, a Verwey transition appears at ca. –160 °C; for PV017 k_m at ~2200 × 10^{-6} SI and PV020 at ~2650 × 10^{-6} SI. This Verwey transition is then followed by lowering of the susceptibility, which is after ca.

–60 °C flat. During heating, both curves display a hump of k_m between ~100 °C and ~390–420 °C, with a maximum at ~280 °C, where PV017 reaches ~2600 × 10^{-6} SI and PV020 ~2550 × 10^{-6} SI. At ~550 °C both curves rapidly drop until 700 °C (Fig. 12). Curie temperatures are observed twice on each path of the heating curve first dominant at ~570 °C, and second subtle at ~620 °C (PV017) and at ~680 °C (PV020). During the cooling, both the T_c are recorded at the same temperatures for both samples. In the case of the sample PV020, susceptibility first steeply rises until ~530 °C, then continues rising but in a very slow manner before reaching down to 470 °C, after which it flatly continues at ~3000 × 10^{-6} SI. Sample PV017 increases susceptibility with a decrease of temperature until the maximum of k_m ~4240 × 10^{-6} SI at 420 °C, after which it slowly goes down to a flat pattern between ~140 °C and –70 °C. That is about the same temperature where PV020 also starts to decrease, both until a Verwey transition at ca. –150 °C (Fig. 12).

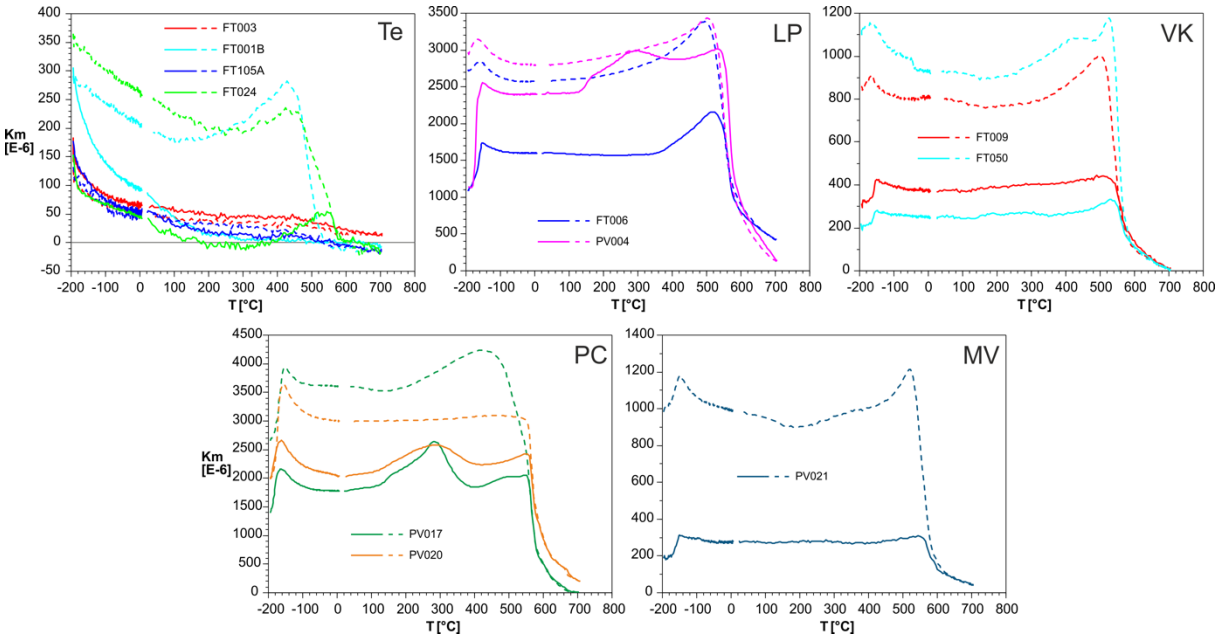

Fig. 12 Diagrams of thermomagnetic curves showing k_m as a function of temperature for representative samples from individual Teplice rhyolite members; full and dashed lines represent heating and cooling curves, respectively; Te – Teichweg member, LP – Lugstein-Pramenáč member, VK – former Vlčí kámen "petro-type", PC – Přední Cínovec member, MV – former Medvědí vrch "petro-type".

For the Medvědí vrch, sampling station PV021 was measured. The heating curve is commenced by a Verwey transition at ca. –150 °C and k_m of ~260 × 10^{-6}. After that, a flat pattern follows until an abrupt decrease at ~550 °C, with a Curie temperature at ~570 °C. T_c on the cooling is at ~550 °C. Then the curve steeply climbs up to susceptibility of 1220 × 10^{-6} SI at temperature ~510 °C. Following this local maximum, the course of the curve

is displaying susceptibilities reaching minimum at ~200 °C and k_m ~860 × 10^{-6}, after which it grows again. At ca. –140 °C, the second low-temperature curve reaches a Verwey transition (Fig. 12).

5.3 Degree of anisotropy and shape parameter (individual specimen data)

For all the Teplice rhyolite members, the degree of anisotropy varies between 1.001–1.049 for individual specimens, corresponding to 0.1–4.9% of anisotropy (Fig. 11b). In the Teichweg member k_m–P diagram, results are scattered between 0.4–4.3%. A major group of 77 specimens indicate a rather low P (0.6–2%) and low k_m (40–100 × 10^{-6} SI) values. The rest is either in line with k_m around 40 × 10^{-6} SI, whereas two minor groups with relatively P around 0.5% yield k_m values at ca. 250 and 425 × 10^{-6} SI. Lugstein-Pramenáč specimens range from 0.5% to 4.6%. The main trend is diagonal-like, where P increases with increasing k_m. In addition, samples with ferromagnetic susceptibility have anisotropy degree always over 1.5% (Fig. 11b). In the Vlčí kámen k_m–P diagram, the P of individual specimens is in the range of 0.1–4.4%. A similar diagonal-like relationship is displayed here in a lesser extent also, and samples with paramagnetic susceptibility do not have P values greater than 2% (Fig. 11b). The relatively highest degree of anisotropy was measured in the case of specimens with k_m ranging between 740–2500 × 10^{-6} SI. Ferromagnetic samples are more scattered, with the dominant cluster between ~1–2.5%. For the Přední Cínovec member, the P of individual specimens is ranging from 0.2 to 4.5% (Fig. 11b). Some minor specimens with relatively higher susceptibilities have also higher lower P values. Importantly, the paramagnetic specimens have lower P values (max ca. 2.8%) compared to ferromagnetic ones (max ca. 4.5%). In the Medvědí vrch ignimbrite, the P range of individual specimens is 0.4–4.9% (Fig. 11b). Apart from the two outliers (P = 4% and 4.9%), two groups are displayed in the k_m–P diagram. For both, P is the similar (0.4–2.1%), but the mean susceptibility corresponds to 44–113 × 10^{-6} (22 specimens) and 192–332 × 10^{-6} SI (38 specimens).

P-T relations are portrayed in Figure 11c. For the Teichweg member, the shape parameter ranges from –0.670 to 0.890. All individual specimens indicate either oblate or triaxial shape of the AMS ellipsoids (126 out of 167 specimens), whereas the rest is prolate. The shape parameter range is greatest (prolate-triaxial-oblate) at low susceptibilities (0.4% < P < 1.7%), while for a higher degree of anisotropy the T is triaxial and dominantly oblate. Lugstein-Pramenáč specimens are clustered mostly around T = 0 (triaxial ellipsoid).

Dispersion of T values from –0.902 to 0.815 is in balance with a trend to a rather prolate shape of AMS ellipsoids for P between ~2–3%. In the Vlčí kámen P-T diagram, all T values are scattered from –0.961 to 0.922, however, 282 specimens are in the oblate shape field whereas 161 specimens are in the prolate field. With P greater than 2.1%, the shape parameter is dominantly oblate. For the Přední Cínovec member, specimens are scattered all over the diagram, with T ranging from –0.971 to 0.930. More than a half (198 out of 347 specimens) depict prolate shape fabrics, with 141 of them in between P of 1.5–3.5%. The Medvědí vrch diagram shows almost uniform distribution, as all the samples are scattered between T values of –0.900 to 0.730, regardless of P. The two groups visible in k_m–P diagram do not show preferred shape of the AMS ellipsoid, as their values are spread to both prolate and oblate areas of the diagram.

5.4 Map patterns of average AMS parameters

Figure 13 illustrates an overall spatial distribution of station-mean AMS parameters k_m, T and P. For the purpose of this study, the bulk (mean) susceptibility is divided as paramagnetic (0–500 × 10^{-6} SI), moderately (500–2500 × 10^{-6} SI) and strongly ferromagnetic (>2500 × 10^{-6} SI; Fig. 13a). For all the 63 sampling stations, k_m ranges from 43 to 5265 × 10^{-6} SI. Starting from the west, the Teichweg member shows paramagnetic behavior for all of the seven sampling stations, with mean values between 43 and 337 × 10^{-6} SI (Fig. 13a). The Lugstein-Pramenáč member (11 stations) has station-mean k_m span from 103 to 3020 × 10^{-6} SI. This member yields three paramagnetic stations close to the border with the Teichweg member. Six moderately ferromagnetic stations are clustered to the north and east. Only two sampling stations show strongly ferromagnetic behavior, located in the central portion (Fig. 13a). The Vlčí kámen has station-mean k_m ranging from 69 to 2691 × 10^{-6} SI (22 stations). Out of these, seven are moderately ferromagnetic, and another two are strongly ferromagnetic. Hence, most of the stations are paramagnetic. Stations dominated by moderately and strongly ferromagnetic signal are located in the center, whereas most of paramagnetic stations occur along the margin (Fig. 13a). Station-mean k_m values for the Přední Cínovec member range between 131 and 5260 × 10^{-6} SI. Strongly ferromagnetic fabrics (8 out of 18 stations) are located mostly in the south and center. The remaining four stations with paramagnetic are in the north (Fig. 13a). Five

stations of the Medvědí vrch are purely paramagnetic, ranging from 47 to 283 × 10^{-6} SI (Fig. 13a).

Map distribution of the station-mean shape parameter (*T*) is divided into five groups (Fig. 13b): strongly prolate (-1 – -0.3), weakly prolate (-0.3 – -0.1), neutral shape (-0.1 – 0.1), weakly oblate (0.1 – 0.3) and strongly oblate (0.3 – 1). The station-mean *T* value ranges between –0.531 and 0.696 for all stations of the Teplice rhyolite. Ignimbrites of Teichweg member have rather oblate-shaped AMS ellipsoids (0.084–0.593). Three stations in the south have weakly oblate shapes of AMS, while only one station is neutral (Fig. 13b). Ranging from –0.346 to 0.286 (station-mean *T* parameter), the Lugstein-Pramenáč member has more often prolate-shaped AMS ellipsoid (5 stations, 2 of them weakly). Another four stations in the center exhibit the triaxial shape of AMS ellipsoids, and two stations in the north are weakly oblate (Fig. 13b). Vlčí kámen's stations range from –0.247 to 0.696 station-mean *T* parameter. Overall, they have rather oblate-shaped AMS ellipsoids (12 stations) and four triaxial. In addition, six stations situated in the center have weakly prolate shapes of the AMS ellipsoid (Fig. 13b). Přední Cínovec member shows almost exclusively neutral to prolate station-mean *T* values (0.364 to –0.531) with affinity to weakly and strongly prolate shape of AMS ellipsoids (10 stations) concentrated on the map in the center (Fig. 13b). From the Medvědí vrch, five stations indicate a range of station-mean shape parameter from –0.465 to 0.205, while only one station has a strongly prolate-shaped ellipsoid to the SW, one station in the center is weakly oblate, and the others have neutral shapes of the AMS ellipsoid (Fig. 13b).

Station-mean degree of anisotropy (*P*) values are relatively low, ranging from 1.004 up to 1.035 (0.4–3.5% of anisotropy). The variations are thus not great, yet I have divided them for easier description into four categories: relatively weakest (0–1%), low (1–2%), moderate (2–3%) and relatively strongest degree of anisotropy (3–4%; Fig. 13c). In the Teichweg ignimbrites, the degree of anisotropy is rather weak, but two stations reach moderate values, one in the north and one in the south (Fig. 13c). Among station-mean values between 1% and 3.5%, the Lugstein-Pramenáč member has two stations with relatively strong *P* values of 3.3% and 3.5%, whereas low *P* values between 1% and 2% at four stations are concentrated at the southern end of the member. Another seven stations indicating values higher than 2% are in the central and northern parts (Fig. 13c). The Vlčí kámen exhibit station-mean *P* values of 0.4–2.5%, yet only 3 out of 22 stations are above 2% of anisotropy. The *P* is between 1% and 2% at 13 stations distributed across the

member's borders on the map (Fig. 13c). Another five stations in the central-eastern part (at the border with Přední Cínovec) and one station to the SW have a relatively weakest degree of anisotropy (<1%).

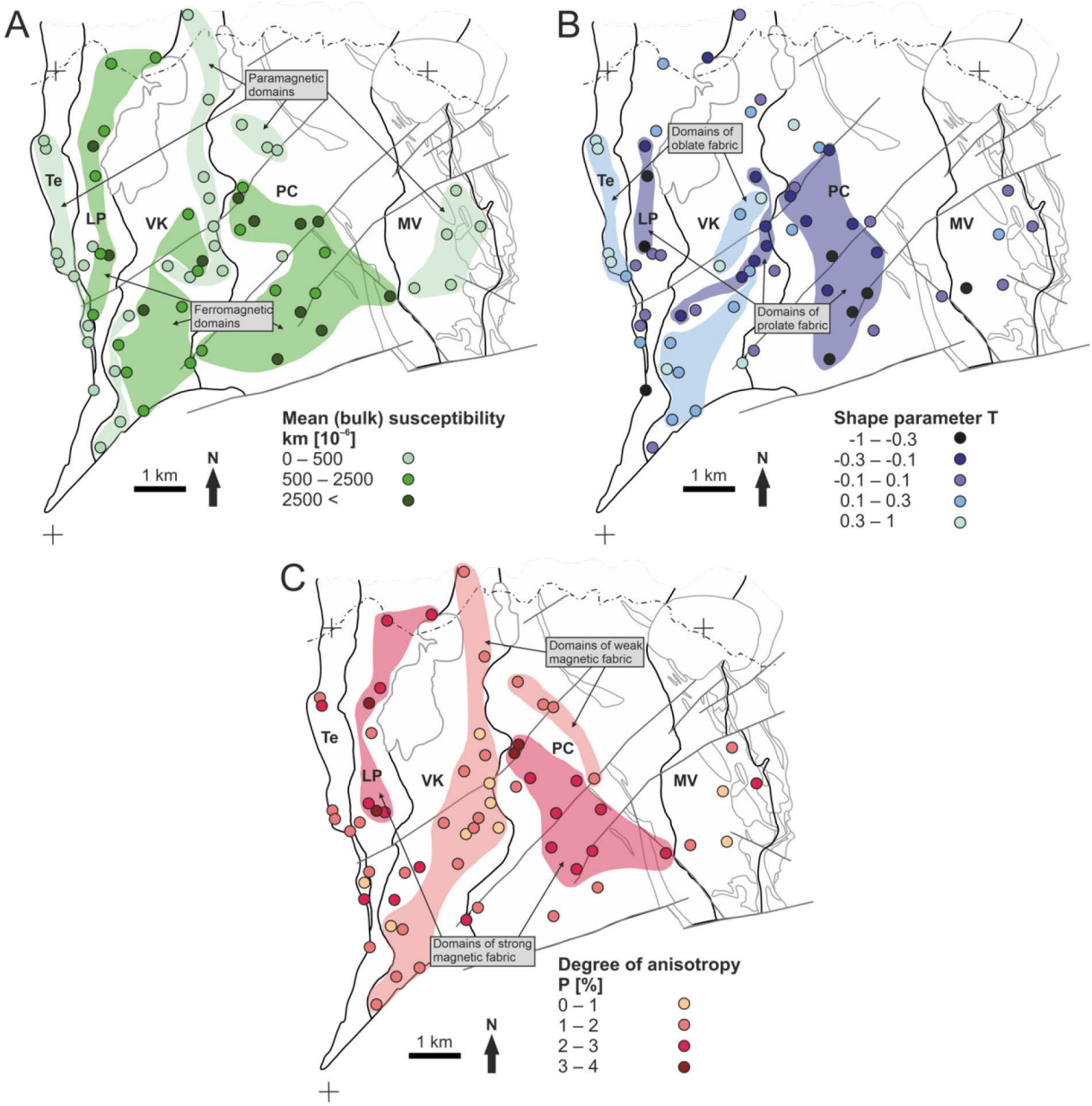

Fig. 13 Simplified maps of the Czech part of the Teplice rhyolite based on Figure 3 highlighting spatial distribution of station-mean AMS parameters color-coded based on parameter values: a) bulk susceptibility (k_m); b) shape parameter (T) and c) degree of anisotropy (P).

Station-mean P values of the Přední Cínovec member varies between 1% and 3.2%. The two highest average susceptibilities (3% and 3.2%) are located close to the borders against Vlčí kámen and Přední Cínovec (Fig. 13c). The rest of the sampling stations are forming two groups. (1) A cluster of moderate P values between 2% and 3% (8 stations) is well

grouped mostly in the center of the Přední Cínovec borders, while (2) eight stations with relatively low *P* values between 1% a 2% are scattered around the group (1) both to the south and north. Even though there are only five sampling stations on the Medvědí vrch area, the station-mean *P* values vary from 0.8% to 2.1% (three categories of *P*; Fig. 13c).

5.5 AMS measurement results

5.5.1 Caldera tilt correction

It has been suggested that the geometry of the Altenberg–Teplice caldera floor is an asymmetric trapdoor dipping towards the east (Benek, 1991). Recently, Tomek et al. (2019) interpreted that the collapse likely occurred after the last eruption of Teplice rhyolite ignimbrites. Thus, to characterize the dynamics of the emplacement of these ignimbrites based on the magnetic fabrics, all the AMS data were rotated in order to correct the post-emplacement subsidence tilt. This was achieved based on the orientation of the bedding of fall tuffs of the Teichweg member. Most of the fall tuffs are known to be deposited as subhorizontal layers. Many authors have observed that the Teichweg fall tuff bedding dips uniformly to the east under ca. 20° to 40° (Jiránek et al., 1987; Schovánek et al., 2004). I have measured bedding of the fall tuffs at two large outcrops FT001 and FT105, the only known Teichweg outcrops where the tuffs are exposed in-situ (e.g., Fig. 14a). The calculated mean dip direction and dip is 068°/27°. Using this bedding orientation, the AMS data for all the Teplice rhyolite members were rotated in the ANISOFT 5 software (Fig. 14a).

In Figure 14a, four stereonets of the Teichweg member measurements are presented highlighting correction for trapdoor subsidence tilt. The left two (blue) stereonets show magnetic foliations of the ignimbrites, while the second two present flow foliation measured at the outcrops. The mean value of the measured magnetic foliation dips generally to the east with a mean dip direction of 078°, dip of 29°, and pole to the magnetic foliation (k_3 axis) is 258°/61°. After the above-outlined rotation procedure, the magnetic foliation is 143°/05° and its pole is 323°/85° indicating near-horizontal magnetic foliation (Fig. 14a). Ignimbrite flow foliations defined by the preferred orientation of fiamme measured at the outcrops are dipping mostly to the east (mean foliation 094°/18°), with few exceptions dipping either rather to the north and south (Fig. 14a). After the rotation of the

data, foliations are slightly more horizontal, however some of the data display also steeper attitudes. The mean rotated flow foliation is 092°/14° (Fig. 14a).

Measurements of individual sampling stations are described in the following chapters and presented in Figures 15–18. Differentiation of the fabrics into normal, oblique and transverse is after Agrò et al. (2015) and Moncinhatto et al. (2019), which describes the angle between magnetic foliation dip direction and magnetic lineation plunge. See the details above in Chapter 4.2.

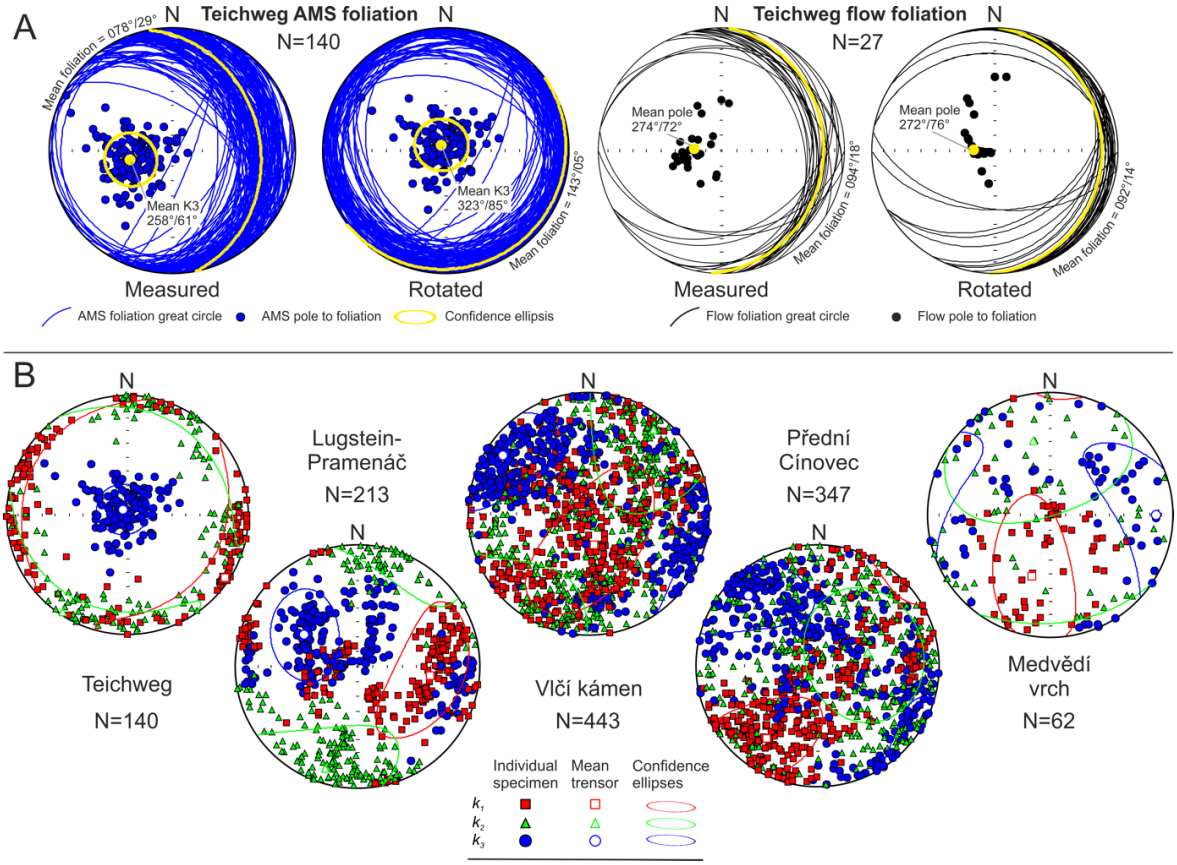

Fig. 14 a) Comparison of magnetic foliation (blue), and flow foliation of Teichweg member ignimbrite (black). Stereonets are equal-area projections on a lower hemisphere. Yellow great circles represent mean values of foliations, yellow symbols their poles, and yellow lines the associated confidence ellipses as determined using the ANISOFT 5 software. Both the magnetic and magmatic foliation stereonets are shown as non-rotated (left stereonets) and rotated after tilt correction (right stereonets). b) Five AMS stereonets of individual specimens, each is representing individual Teplice rhyolite members: Te – Teichweg member, LP – Lugstein-Pramenáč member, VK – former Vlčí kámen "petro-type", PC – Přední Cínovec member, MV – former Medvědí vrch "petro-type".

5.5.2 Teichweg member

AMS measurements of the Teichweg ignimbrites shows well grouped k_3 axes of all individual specimens around their mean value, whereas k_1 and k_2 axes form thin girdle around the stereonet rim (Fig. 14b). Two stations FT001 and FT105 were divided into two stereonets in order to distinguish underlying fall tuff (labeled as T) and overlying ignimbrite

(labeled as I; Fig. 15a). Both fall tuff stations have well grouped k_3 axes steeply dipping to the NE (subhorizontal magnetic foliation). The associated k_1 and k_2 axes are well grouped at station FT001, whereas in the case of FT105 they form a SW dipping girdle (Fig. 15a). In ignimbrites, most of the flow foliations dip shallowly to the west. At most stations, the flow foliation and magnetic foliations are parallel to near-parallel (Fig. 15a). At station FT011, flow foliation was not discernible.

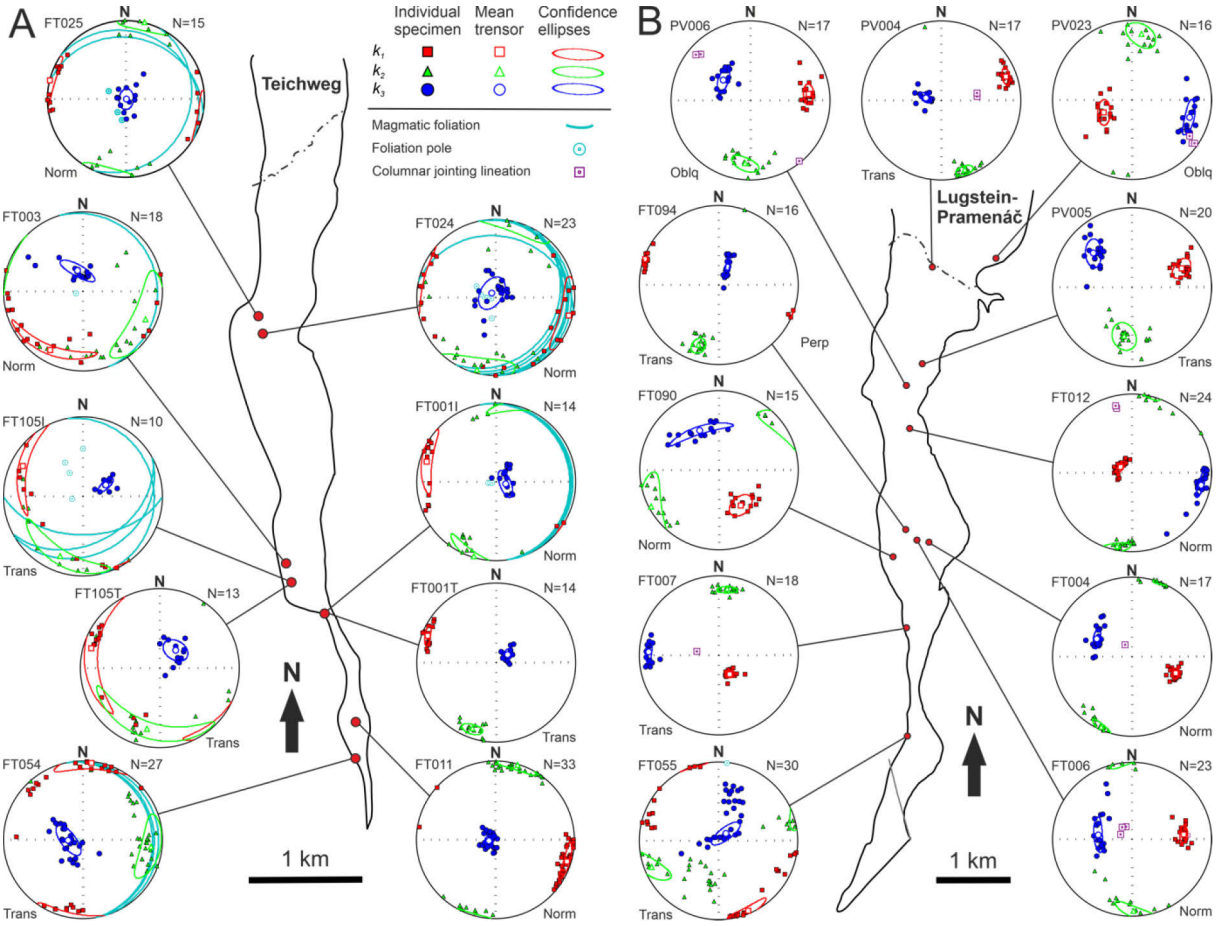

Fig. 15 Stereonets (equal-area projections on a lower hemisphere) of rotated AMS measurements from a) Teichweg member and b) Lugstein-Pramenáč member. In the Teichweg member, stations FT001 and FT105 are labeled with T or I referring to underlying fall tuffs or overlying ignimbrite, respectively. Norm – normal fabrics; Oblq – oblique fabrics; Trans – transverse fabrics.

In detail, stations in the south (FT054 and FT011) have near-horizontal magnetic foliation, but FT011 indicates better grouped principal susceptibility axes than FT054, which form a girdle-like pattern. In addition, these stations are good examples of normal (FT011) and transverse fabrics (FT054), with magnetic lineation plunge being parallel and perpendicular to magnetic foliation dip direction, respectively (Fig. 15a). Between stations FT001I, FT105I and FT003, all k_3 are well grouped, whereas k_1 and k_2 axes are scattered

into thin girdles. While for FT001 and FT105, the subhorizontal magnetic foliation dips to the W and WSW, station FT003 displays k_1 and k_2 girdle pattern with magnetic foliation dipping shallowly to the south. In addition, stations FT024 and FT025 in the northern part are very similar, with near-horizontal magnetic foliation dipping to the east and southeast. Magnetic fabrics are almost always normal (5 stations), with transverse behavior at two stations FT054 and FT105I (Fig. 15a). The overall distribution of magnetic foliation dip direction and magnetic lineation plunge in ignimbrites is five normal and two transverse fabrics out of seven stations (i.e., 71% and 29%, respectively).

5.5.3 Lugstein-Pramenáč member

The Lugstein-Pramenáč member shows well grouped principal susceptibility axes of individual specimens around their mean values (Fig. 15b). The k_3 axes of individual specimens indicate a dominant cluster of moderately dipping magnetic foliations to the east and two minor clusters with magnetic foliations dipping to the west and south. The associated magnetic lineations have a dominant cluster of flat-lying magnetic lineations plunging to the east, and two minor clusters of steep to sub-vertical lineations and subhorizontal west-dipping lineations (Fig. 14b). The two minor clusters represent AMS fabrics on individual sampling stations PV023 and FT012, and FT090 and FT094, respectively (Fig. 15b). In the individual AMS stereonets, maximum principal susceptibility axes are well grouped, but the intermediate and minimum principal susceptibilities sometimes exhibit slight girdle-like patterns (e.g., FT006 and FT090; Fig. 15b).

Lugstein-Pramenáč stations exhibit a range of normal (FT004, FT006, FT012, FT090), oblique (PV006, PV023) and transverse fabrics (PV004, PV005, FT007, FT055, FT094). In detail, magnetic lineations at stations in the center (FT004, FT006, FT007, FT090) are plunging moderately to the south and southeast (Fig. 15b). In the northern part, subhorizontal eastward plunging magnetic lineations are observed and are characterized by transverse and oblique fabrics (PV004, PV005 and PV006; Fig. 15b). In the case of normal FT012 fabric, both the magnetic foliations and lineations are subvertical, dipping and plunging to the WNW. In addition, station PV023 has the orientations of magnetic fabrics similar to FT012 but is characterized as oblique (Fig. 15b). The overall distribution of magnetic foliation dip direction and magnetic lineation plunge of the ignimbrites is four

normal, two oblique and five transverse fabrics out of 11 stations (i.e., 36%, 18 and 46%, respectively).

At seven sampling stations, the orientation of columnar jointing was also measured (FT004, FT006, FT007, FT012, PV004, PV005, PV023). Only at the station PV023, elongation direction of columns is parallel to mean k_3 (perpendicular to magnetic foliation), whereas at station PV004 the columnar jointing is roughly parallel to the mean k_1 axis (magnetic lineation. The rest of the stations shows no apparent parallelism of magnetic fabrics and columnar jointing (Fig. 15b).

5.5.4 Vlčí kámen: Western part of Vlčí Kámen-Medvědí Vrch member

The Vlčí kámen "petro-type" has the largest number of sampling stations among the examined Teplice rhyolite area (a total of 22; Fig. 16). The all data stereonet of this "petro-type" shows rather scattered principal susceptibility axes of all individual specimens, yet k_3 axes show two dominant clusters of steep southeast and northwest dipping magnetic foliations, with k_1 and k_2 axes defining a broad northeast-southwest elongated girdle. In detail, magnetic lineations (k_1 axes) are mostly steep to subvertical, with minor clusters of northeast and southwest shallowly plunging lineations (Fig. 14b).

The central-eastern part (stations FT030, FT033, FT039, FT040 and FT096) indicate both transverse and normal fabrics with largely scattered principal susceptibility axes. In addition, stations FT033 and FT039 exhibit poor girdle-like pattern of k_2 and k_3 axes (Fig. 16). Two other stations, where principal susceptibility axes are moderately scattered, are FT092 (transverse) and PV012 (normal). Well-clustered transverse, ~NNE–SSE striking steep magnetic foliations with a prominent girdle of k_1 and k_2 are displayed at stations FT009 and FT048 (Fig. 16). Stations FT089 and FT157 in the north close, to the Cínovec pluton yield ~E–W striking steep magnetic foliations, different to the overall ~NE–SW magnetic foliations strike of the majority of stations in the Vlčí kámen "petro-type" (Figs. 14b, 16).

The southerly stations have mostly steep to subvertical magnetic foliations dipping to the east and southeast (FT008; FT009; FT042; FT045; FT048; PV009; PV010; PV012). Apart from the normal fabric of PV012, these stations exhibit mostly transverse or oblique fabrics.

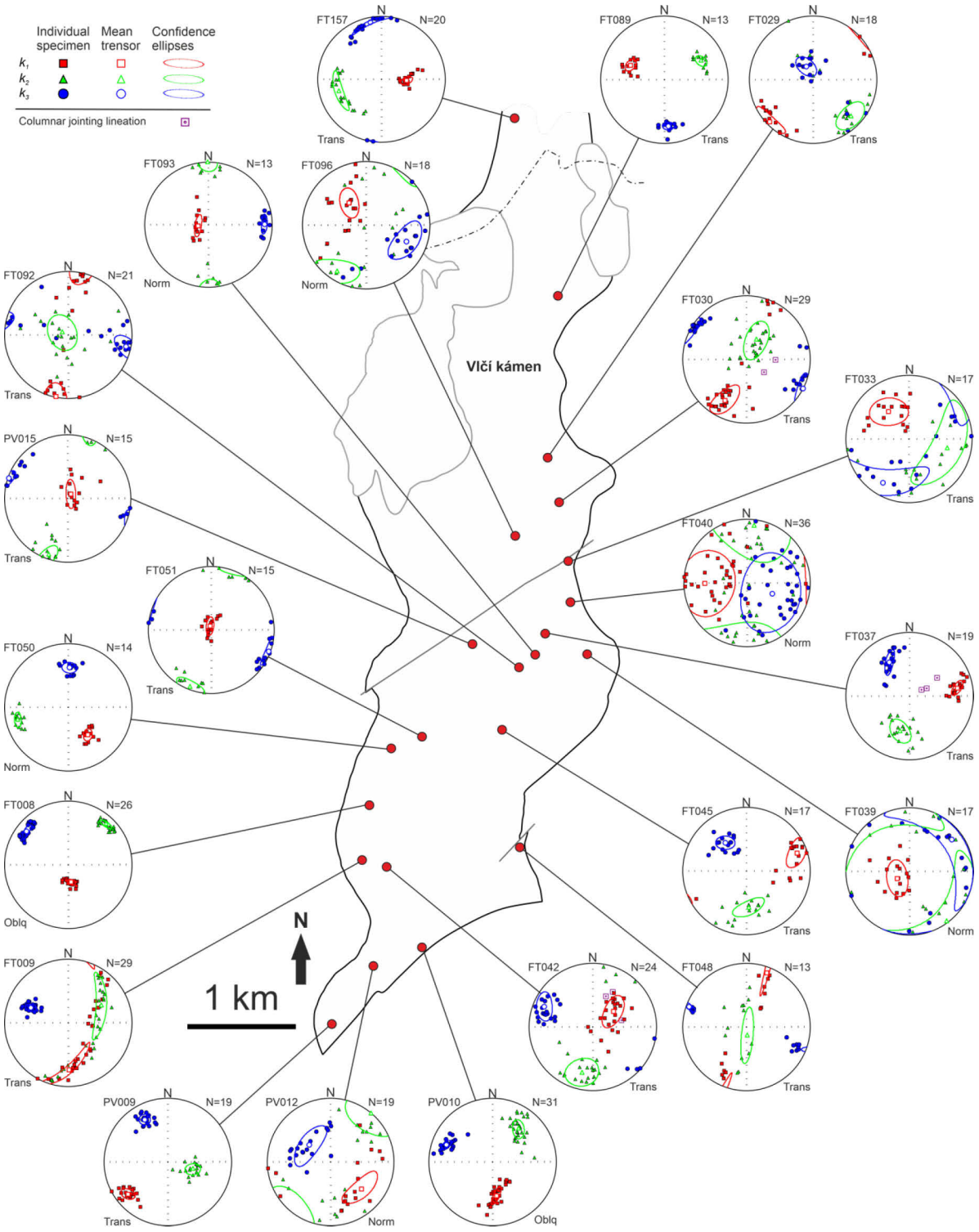

Fig. 16 Stereonets (equal-area projections on a lower hemisphere) of rotated AMS measurements from the western part of Vlčí kámen-Medvědí vrch member, former Vlčí kámen. Norm – normal fabrics; Oblq – oblique fabrics; Trans – transverse fabrics.

In the central part, such transverse fabrics at stations FT030, FT037, FT050, FT051, FT092 and PV015 are also steep to subvertical, however dip both to the west-northwest and east-southeast (Fig. 16). For stations FT093 and FT096 with normal fabrics, the orientation of

the subvertical magnetic foliations dips to the west. Lastly, the only subhorizontal magnetic foliation of the Vlčí kámen "petro-type" was detected in the case of station and FT029 (transverse; Fig. 16). Overall distribution of magnetic foliation dip direction and magnetic lineation plunge in ignimbrites is six normal, two oblique and fourteen transverse fabrics out of twenty-two stations (i.e., 27%, 9% and 64%, respectively).

The Vlčí kámen has only two stations with measured columnar jointing (FT037 and FT042), however, the column elongation is parallel with the mean k_1 axis at station FT042.

5.5.5 Přední Cínovec member

The Přední Cínovec member poses a second largest dataset (18 stations). Similarly as the Vlčí kámen, the Přední Cínovec has overall rather indistinctive fabrics on the stereonet of all individual AMS data (Fig. 14b). However, we can still observe that minimum principal susceptibility axes of all individual specimens depict a broad ~NW–SE girdle-like pattern. The maximum principal susceptibility axes constitute a cluster of southwest plunging shallowly to moderately magnetic lineations, while a minority of specimens indicate also vertical and subhorizontal eastward plunging k_1 axes (Fig. 14b).

AMS ellipsoids of individual sampling stations exhibit three main characteristics: (1) strongly lineated, where k_1 is grouped, and k_2 with k_3 are forming a girdle; (2) strongly foliated, where k_1 with k_2 are forming a girdle, with k_3 being clustered; and (3) a group where all three axes are well-grouped. A few sampling stations are displaying a transitional fabric (Fig. 17).

(1) Among the first group, there are stations FT047, FT076, FT079, FT083, PV017, PV018 and PV019. All are exhibiting either normal or transverse fabric, and the orientations of their steep to shallow k_1 are fluctuating from the SW to the NE, whereas at stations FT076 and PV019 the k_1 is near-horizontal plunging to the north and southwest, respectively (Fig. 17). (2) In the second group, there are three stations FT031, FT081, FT088. These have transverse fabrics and near-vertical NE–SW striking foliations (Fig. 17). FT081 is not forming as good a girdle as the other two stations, but exhibit similar oblate fabrics (Fig., 13b). Station FT032 depicts similar but oblique fabrics, rather scattered principal susceptibility data, and steep ~E–W magnetic foliations (Fig. 17). (3) The third group includes stations FT026, FT069, FT071, FT084, PV020 and PV024. They do not have a general trend of principal susceptibility axes, neither they agree on fabrics pattern, being

normal, oblique and transverse. In addition, station FT027 shows none to poorly clustered principal susceptibility axes (Fig. 17).

The spatial distribution reveals that stations of groups (1) and (3) are concentrated mainly in the center of the Přední Cínovec member, whereas stations of the group (2) are mostly close to the western border (Fig. 17). Moreover, three stations FT032, FT071 and FT084 shows parallel to near-parallel AMS fabrics with a contact of the adjacent younger microgranite dikes (Fig. 17).

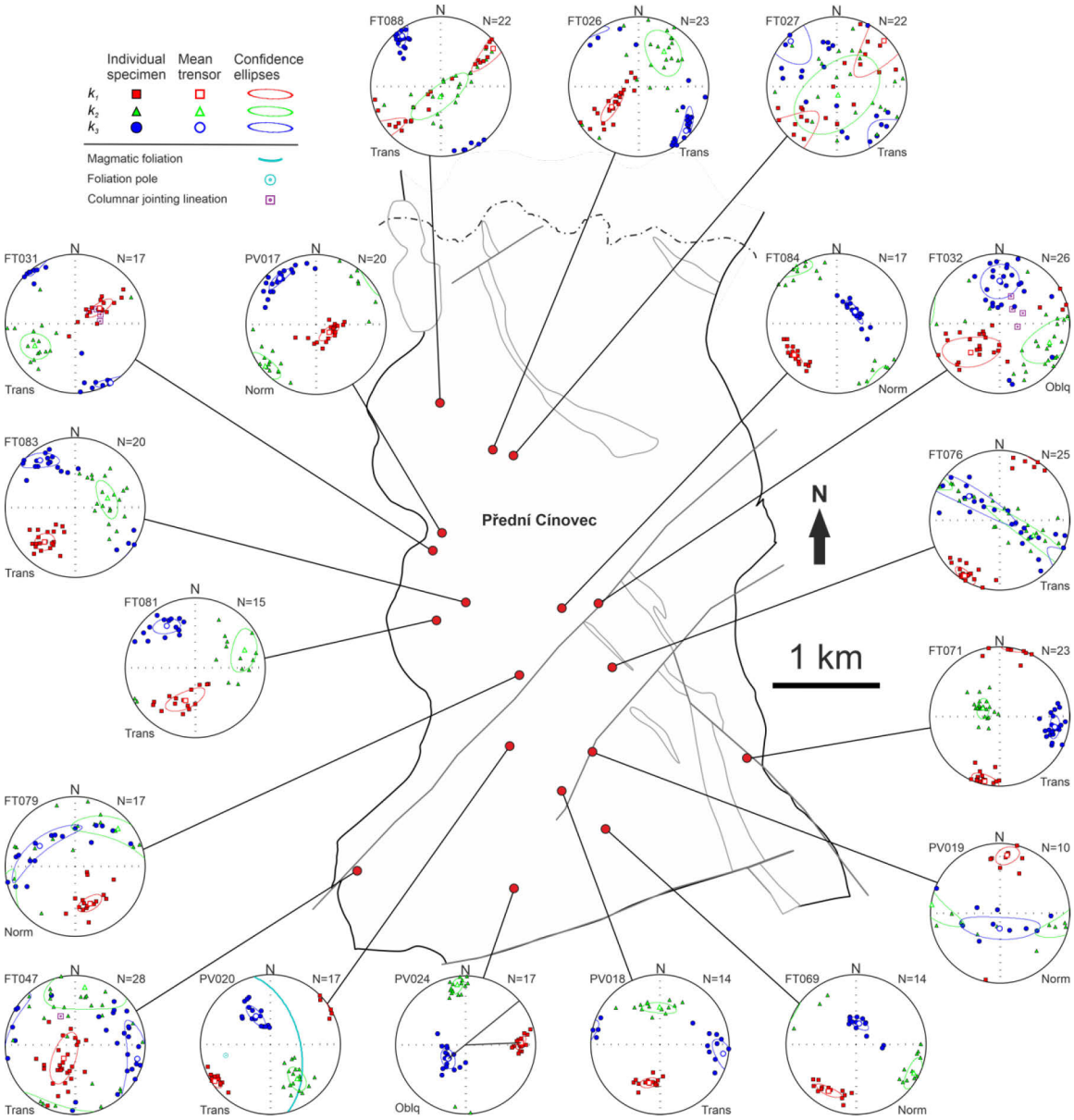

Fig. 17 Stereonets (equal-area projections on a lower hemisphere) of rotated AMS measurements from Přední Cínovec member. Norm – normal fabrics; Oblq – oblique fabrics; Trans – transverse fabrics.

The overall distribution of magnetic foliation dip direction and magnetic lineation plunge in ignimbrites is five normal, two oblique and eleven transverse fabrics out of a total seven (i.e., 28%, 11% and 61%, respectively).

Columnar jointing of the Přední Cínovec was measured at stations FT031, FT032 and FT047. Elongation direction of columns parallel to magnetic lineation is only at station FT032, however, at FT031 and FT047 the columnar lineation is dispersed from the magnetic fabrics (Fig. 17).

5.5.6 Medvědí vrch: Eastern part of Vlčí Kámen-Medvědí Vrch member

In the area of the Medvědí vrch, only five stations were sampled and measured (Fig. 18). All data stereonet shows no apparent clustering of principal susceptibility axes of individual specimens (Fig. 14b). In detail, stations FT019, FT106 and PV022 yield steep ~NW–SE striking foliations, parallel to elongation of younger porphyritic dikes (Fig. 18). Station FT019 has principal susceptibility axes well grouped around their mean value, and the magnetic lineation plunges moderately to the southwest. Station PV022 has principal susceptibility axes a bit more scattered, and the steep lineation plunges to the southeast (Fig. 18). Minimum principal susceptibility axes of individual specimens are well-clustered at station FT106, whereas k_1 and k_2 axes define a thin girdle. Station FT016 displays well clustered principal susceptibility axes, subvertical ~NE–SW magnetic foliation and subvertical magnetic lineation. Station PV021 is somehow different displaying well grouped k_1 axes of individual specimens defining a subhorizontal magnetic lineation and plunging to the SSW, while k_2 and k_3 axes form a thin girdle oriented ~WNW–ESE (Fig. 18). The overall distribution of magnetic foliation dip direction and magnetic lineation is for the ignimbrites: two normal and three transverse fabrics out of total seven (i.e., 40% and 60%, respectively).

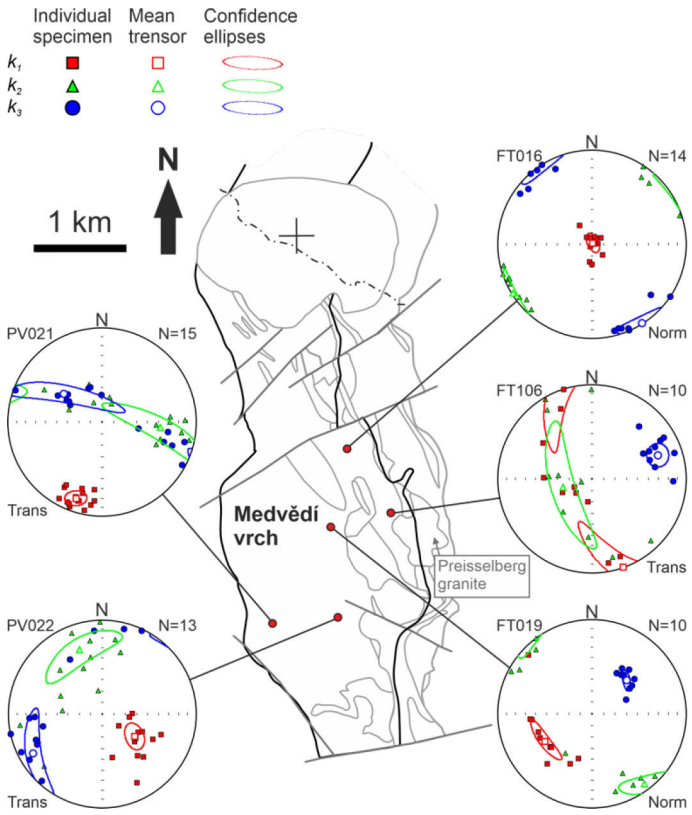

Fig. 18 Stereonets (equal-area projections on a lower hemisphere) of rotated AMS measurements from the eastern part of Vlčí kámen-Medvědí vrch member, former Medvědí vrch. Norm – normal fabrics; Oblq – oblique fabrics; Trans – transverse fabrics.

6 Discussion

6.1 Source of AMS signal

The overall low bulk (mean) susceptibility of the Teichweg member suggests that dominant carriers of the AMS signal are paramagnetic ferrosilicates such as biotite or chlorite. This is further corroborated by a typical hyperbolic course of the thermomagnetic data. Interruption of the hyperbolic course at ca. 400 °C and order of magnitude higher susceptibility on reverse cooling curves is explained by the presence of new Fe-Ti phases. These minerals had grown during the heating experiment, which is evidenced by a missing Verwey transition at first cooling curves. Thermomagnetic curves of the Lugstein-Pramenáč member characterized by a typical Verwey transition and Curie temperatures between ~560–570 °C imply that low-Ti titanomagnetite dominates the AMS signal complemented by a minor contribution of maghemite (Fig. 12). This is in agreement with the overall ferromagnetic susceptibility of this member, however, few stations are characterized rather by paramagnetic minerals (Fig. 11a). The Vlčí kámen "petro-type" k_m–T curves are as well showing a box-like behavior with a Verwey transition and Currie temperatures at ~570 °C interpreted as a low–Ti titanomagnetite carrying the AMS signal (Fig. 12). The bulk (mean) susceptibility diagram, however, displays that majority of specimens have relatively low susceptibility (10^{-4}), and thus implies the dominance of paramagnetic ferrosilicates (Fig. 11a). The Přední Cínovec member yielded much higher ferromagnetic susceptibilities, however, nearly one third is paramagnetic. The ferromagnetic behavior is further corroborated by the course of thermomagnetic curves. These display typical Verwey transition and Curie point temperatures at ca. 570 °C pointing to a dominant low-Ti titanomagnetite with an indistinct contribution of magnetite and hematite as exemplified by minor humps at ca. 350 °C and indistinct k_m decreases at 620 °C and 680 °C, respectively. Paramagnetic contribution can be seen on a slight hyperbolic decrease of k_m after reaching the Verwey transition from ca. –150 °C to 50 °C (Fig. 12). Despite the overall paramagnetic susceptibility of the Medvědí vrch "petro-type" (Fig. 11a), the only one k_m–T curve indicates a weak pattern implying the presence of low-Ti titanomagnetite (Fig. 12).

To summarize the above, AMS signal of the Teichweg member and Medvědí vrch "petro-type" is dominated by paramagnetic ferrosilicates, while the Lugstein-Pramenáč member, Vlčí kámen "petro-type" and Přední Cínovec member include a mixture of

paramagnetic ferrosilicates and low-Ti titanomagnetite. The number of stations with ferromagnetic susceptibilities increases from the Lugstein-Pramenáč, through the Vlčí kámen to Přední Cínovec.

6.2 Magnetic fabrics of pyroclastic density currents deposits

The AMS interpretations with respect to PDC dynamics, flow direction, deposition and the possible effect of welding or rheomorphism are not always straightforward. Convectional relation of angles between foliation dip direction and lineation plunge may distinguish between laminar (normal fabric) and turbulent PDC (transverse fabrics), may assist in the determination of distances from the vent, or may identify the vertical and lateral position within a single ignimbrite flow unit (e.g., Agrò et al., 2015; Moncinhatto et al., 2019; Ort et al., 2003; Platzman et al., 2020). However, local conditions such as paleotopography (at the time of an eruption) may alter these conventions. For instance, the meandering of a PDC and change of the direction is sometimes observed (vertically or horizontally), causing that pyroclastic flows to bypass the direct paths from the source (LaBerge et al., 2009). Furthermore, the intensity of the clustering of principal susceptibility axes may change in a vertical section of a single ignimbrite unit. The axes are usually aligned best at the base, but are more dispersed in upper layers, probably as a result of either upward diminishing shear-rate or more laminar behavior in lower layers (Fisher et al., 1993; Cagnoli and Tarling, 1997; LaBerge et al., 2009). The shape of AMS ellipsoids may also assist in distinguishing between high-grade intensely welded and rheomorphic ignimbrites (Hong et al., 2016). Another important part play tributaries and distributaries of PDC channels (smaller flows converging into a flow and separation of the flow, respectively), so that flow paths at the same distance from the source are different, even for events with one feeding vent (Palmer and MacDonald, 1999). A gravity-driven downflow was described on the flanks of valleys of a volcano, where PDC can sometimes have even opposite direction due to the paleotopography (Ort et al., 2003, 2015). A similar feature was described by Fisher et al. (1993), who have described PDC deposition on the other side of a 1000 m high mountain ridge.

Most of these findings are, however, based upon research of relatively young Cenozoic volcanic rocks, as it is increasingly difficult to interpret older Paleozoic volcanic complexes due to erosion and possible tectonic overprint. For instance, Ort et al. (1999)

have mentioned in their work, how important it is to have undeformed deposits in order to correctly infer the source location.

Nevertheless, several authors determined ignimbrite paleoflows using the AMS on Mesozoic and Paleozoic calderas (e.g., Wang et al., 2001; Sohn et al., 2009; Willcock et al., 2015; Hong et al., 2016). Willcock et al. (2015), who studied the Permian Ora caldera, a caldera likely not affected by the Alpine orogeny. As k_1 axis can vary due to different depositional processes (saltation, rolling, etc.), they used mainly k_3 direction to infer flow directions. Their work benefited mostly from extensive vertical profiles more than 1 km high, and together with a large lateral extent, allowed them to identify both lateral and vertical variations. Among other older ignimbrites, Carboniferous PDC deposits and their source location were examined by Wang et al. (2001). After bedding correction, they have separated measured magnetic fabrics into three groups: normal, inverse and intermediate. Normal fabrics have k_3 axis steep to subvertical and k_1 shallowly plunging < 30°. The inverse fabric on the other hand have a plunge of k_1 > ca. 50° and k_3 < ca. 30°, while intermediate fabrics do not have characteristics of either of the normal and inverse components. Wang et al. (2001) discussed inverse fabric to be probably the result of tectonic overprint, but as the orientation of their ignimbrites was corrected (rotated) for original orientation, they assumed that principal susceptibility axes did change, but only their plunge and not their trend. What is generally agreed upon is that mainly the k_1 and k_3 principal axes and their orientations should be used.

6.3 Flow directions and welding of the Teplice rhyolite

Teplice rhyolite ignimbrites of the Altenberg–Teplice caldera are one of the oldest volcanic deposits that were investigated in terms of PDC dynamics using magnetic fabrics. Provided, that the Teplice rhyolite represents a proximal caldera facies, it is clear that the source vent should be located nearby (e.g., Winter et al., 2008). Thus, a rather different approach in the interpretation of AMS fabric should be applied in contrast to, interpretations of Wang et al. (2001), for instance. Since the topography and outcrop distribution of the Ora caldera enabled Willcock et al. (2015) to study the ignimbrites both in horizontal and vertical sections, their case study is also a little different from the Teplice rhyolite. However, on the southern flank of the Krušné hory/Erzgebirge Mts. the Teplice rhyolite exposes many outcrops in a large aerial extent, thus enables examination of various ignimbrite members. Each of these members yields rather contrasting magnetic fabrics and parameters allowing

me to infer on dynamics of PDCs including flow directions, degree of welding, rheomorphism and caldera resurgence. My interpretations are outlined below.

Among all the Teplice rhyolite members, the Teichweg displays the most uniform AMS fabrics represented by stereonets exhibiting an oblate behavior of subvertical k_3 axes and shallowly dipping magnetic foliations (Figs. 13b and 15a). This AMS fabric pattern corresponds well to the characteristic of magnetic fabrics of Cenozoic ignimbrites interpreted elsewhere as representing imbrication of pyroclastic particles during flow and deposition of PCD (e.g., MacDonald and Palmer, 1990; Fisher et al., 1993; Ort et al., 1999, 2003; LaBerge et al., 2009). This allows me to infer the direction of pyroclastic flow and the location of the possible vent system. Variations in the orientation of magnetic foliations resulting from pyroclastic particles imbrication suggest flow directions to the east (3 stations), west (3 stations) and north (one station; Fig. 19). These variations are explained either as minor changes in paleo-relief locally changing the flow direction, or the near-horizontal foliations impose a large uncertainty on reliable estimation of source location or flow directions. However, the majority of flow foliations measured on outcrops and fiamme asymmetry determined under polarization microscope on oriented thin-sections (after tilt correction; Fig. 4d) indicate dominant flow direction from east and northeast, possibly from the eastern dike abundant area (Fig. 3).

It is important to note, that the presence of flattened fiamme imply a low to moderate degree of welding (Casas-García et al., 2019). Ort et al. (1999) suggested that the apparent macroscopic fabrics such as the preferred orientation of fiamme are either due to load bedding or flow shear. Based on magnetic fabric orientation and asymmetry of flattened fiamme defining strong flow foliation, I interpret that the fabrics in the Teichweg member represent rather the flow shear fabric developed during primary welding. In addition, the dominance of normal fabrics (only two are transverse) implies a laminar behavior of the PDC (Agrò et al., 2015; Ort et al., 2015; Moncinhatto et al., 2019). To conclude, the Teichweg member exemplifies a low- to moderately welded ignimbrite recording a laminar PDC with a vent location to the east or southeast flowing towards east and southeast (Fig. 19). Thus, the vent system might be represented by ~N–S striking microgranite dikes located in the caldera center (Fig. 3a).

6.4 Ignimbrite rheomorphism and local post-collapse resurgence

The dominantly prolate shape of AMS ellipsoids, moderately to strongly ferromagnetic magnetic fabrics with relatively higher anisotropy degree are quite abundant in the area of the Lugstein-Pramenáč member, differing significantly from Teichweg member (Figs. 11, 13 and 15). Such distinction is further supported by the different microstructure of both members (Figs. 4 and 5). Rather steep magnetic foliations and variously plunging magnetic lineations do not represent "classic" magnetic fabrics of non-welded to moderately-welded ignimbrites (Pioli et al., 2008) and may reflect some sort of fabrics transposition. Such a rotation might be initialized by a ductile deformation, which could be caused either by a tectonic strain (Wang et al., 2001) or a change from pyroclastic flow deposition into rheomorphic viscous flow (Pioli and Rosi, 2005; Pioli et al., 2008; Hong et al., 2016). The former can be excluded as after the emplacement of the Altenberg–Teplice caldera, no major tectonic event that can cause such ductile deformation occurred in this area. Moreover, such an event would affect also the Teichweg member. Thus, the rheomorphic viscous flow is more likely. Such rheomorphism, however, obscures the primary flow and depositional making it impossible to interpret the original PDC flow direction and vent locations (Fig. 19).

Magnetic anisotropy data of the Vlčí kámen "petro-type" are very scattered, and do not show any uniform results. Paramagnetic domains on both west and east boundaries do not match with domains of the oblate and prolate shape of the AMS ellipsoids, and most of the stations yield low values of degree of anisotropy. Throughout this "petro-type", orientations of magnetic fabrics vary significantly in both directions and grouping of individual principal susceptibility axes. However, two main trends can be distinguished. At 55% of the stations, the fabrics are prolate with a relatively higher degree of anisotropy, whereas the other 45% are slightly oblate with a lower degree of anisotropy (Fig. 19). Some of these stations (in both groups) exhibit transitional behavior between these two groups but were marked as on or the other group. Importantly, the former group is indistinguishable from the fabric patterns of the Lugstein-Pramenáč member. This implies that a major portion of the Vlčí kámen "petro-type" can be characterized also as rheomorphic ignimbrite, whereas the remainder may represent a transitional type between high-grade strongly welded and rheomorphic ignimbrite (Fig. 19). In both cases, the determination of the PDC flow direction is impossible.

The south-central portion of the Přední Cínovec member is dominated by strongly prolate fabrics and the relatively highest degree of anisotropy among all Teplice rhyolite members. Station-mean magnetic fabrics of the central part are scattered with no apparent fabric pattern on the map. Wang et al. (2001) interpreted similar features as representing ductile deformation. Hence, similarly to Lugstein-Pramenáč and Vlčí kámen, I suggest that magnetic fabrics of the Přední Cínovec represent a rheomorphic viscous flow obscuring the primary flow fabrics (Fig. 19). This interpretation is in agreement with Pioli and Rosi (2005) and Hong et al. (2016).

To summarize, the Lugstein-Pramenáč, Vlčí kámen and Přední Cínovec indicate domains corresponding to rheomorphic viscous flow. These domains are more or less located in the centers of each unit (Fig. 19). The location of rheomorphic domains corresponds well to a model of ignimbrite units of Pioli and Rosi (2005), who proposed that the central portions of voluminous ignimbrites are often characterized by rheomorphism due to the concentration of heat flux. In contrast base, top and margins of ignimbrite units cool more rapidly preventing the formation of rheomorphic viscous flows.

Except for the Teichweg member, rheomorphism largely obscured the primary flow fabric of ignimbrites, thus the interpretation of their vent systems is not possible. Hence, I cannot confirm or rule out whether some of these ignimbrites were sourced from the Sayda-Berggießhübel dike swarm as suggested by Winter et al. (2008).

The magnetic fabrics data do not correlate well with the orientation of poorly defined columnar jointing, which is a rather scares across most of the outcrops. This implies that Teplice rhyolite does not exhibit well-preserved columnar jointing, and/or poor correlation with magnetic fabrics may indicate misinterpretation of columnar jottings with respect to the intersection of several fracture patterns.

6.5 Post-collapse resurgence

The AMS dataset of the Medvědí vrch “petro-type” is rather small to allow extensive interpretations. I outline a hypothesis (not an actual interpretation) for the Medvědí vrch that the magnetic fabric could be influenced by a resurgence in an area intensely intruded by microgranite dikes and Preisselberg pluton (Fig. 3). Indeed, magnetic fabrics in this area strike parallel with intrusive contacts of these dikes forming a poorly constrained contact structural aureole, whereas one station is located too far away from this area to be affected by dike emplacement (Fig. 19). Furthermore, few other stations in the Vlčí kámen and

Přední Cínovec ignimbrites yield contact parallel fabrics with the Cínovec granite and other microgranite dikes, supporting this resurgent hypothesis (Fig. 19). If true, the emplacement of these dikes, plutons and the associated resurgence must have occurred immediately after deposition of Teplice rhyolite, when the ignimbrites were still hot and ductile enough to allow transposition of magnetic fabrics in a magmatic state to reorient into the structural aureole.

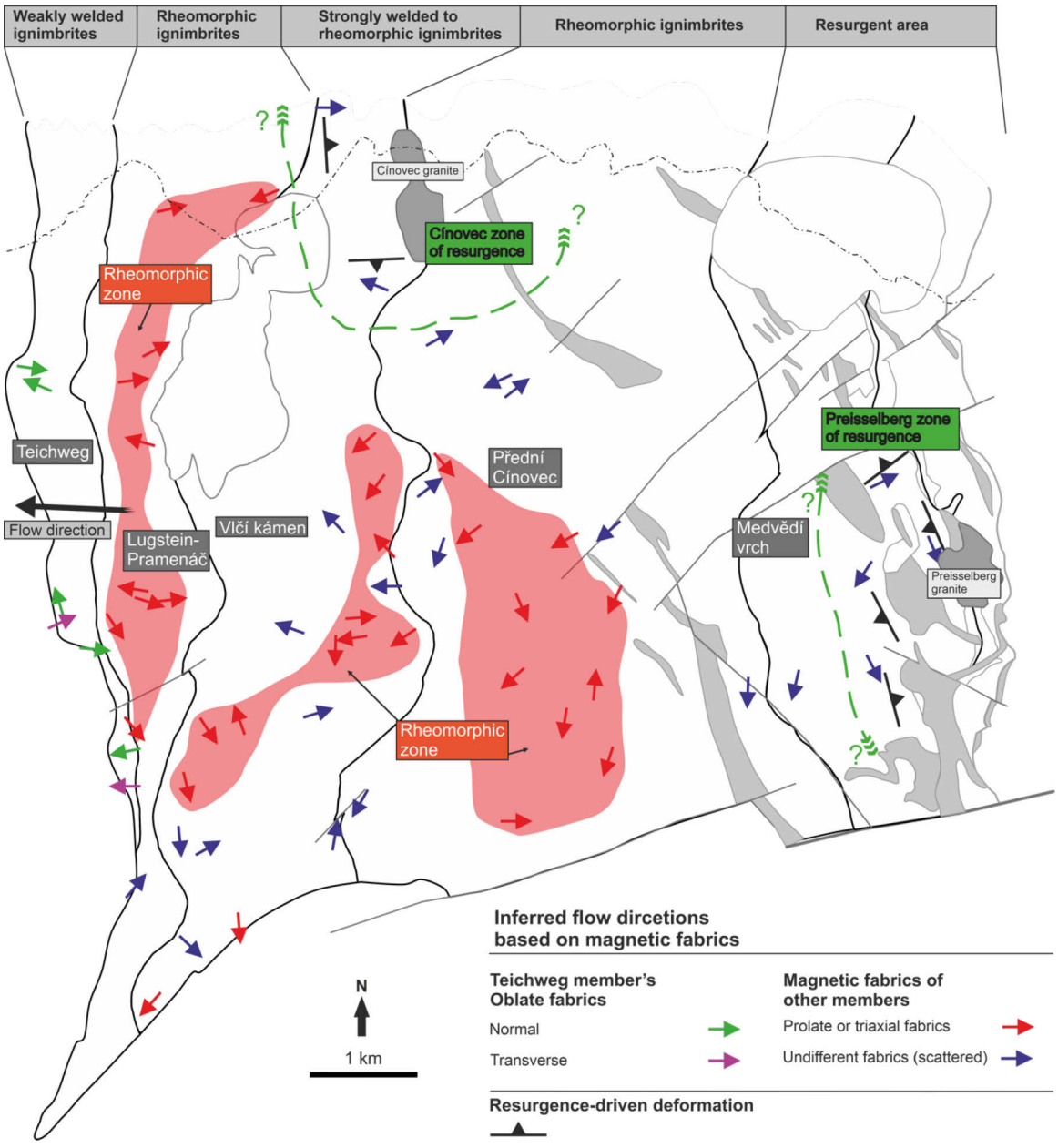

Fig. 19 AMS fabrics were divided into (1) oblatelly-shaped AMS ellipsoids of the Teichweg member with normal and transverse fabrics after Agrò et al. (2015), and (2) prolate to triaxial ellipsoid shapes and stations with scattered principal susceptibility axes (for Lugstein-Pramenáč, Vlčí kámen-Medvědí vrch and Přední Cínovec members). The estimated general flow direction of the Teichweg member from an eastern vent is depicted by an arrow. Note the highlighted zones of rheomorphic and resurgence zones.

7 Conclusions

- The Teplice rhyolite represents caldera proximal ignimbrite facies deposited from several pyroclastic density currents.
- Magnetic fabrics carried by a mixture of paramagnetic ferrosilicates and low-Ti titanomagnetites yielded contrasting AMS parameters, clustering/girdling of principal susceptibility axes and orientation of magnetic foliations and lineations across all examined members of the Teplice rhyolite.
- AMS fabrics allowed me to decipher complex dynamics of these PDCs from flow directions and source vent location, through welding to rheomorphic viscous flow.
- The westerly Teichweg member represents a weakly to moderately welded ignimbrite that was deposited from westward flowing laminar PDC, likely sourced from the vent(s) in the eastern parts of the Altenberg-Teplice caldera rim rich in rhyolite dikes.
- Lugstein-Pramenáč, Vlčí kámen and Přední Cínovec on the other hand are voluminous ignimbrites that were hot enough to initialize rheomorphic viscous flow.
- The rheomorphism, however, obscured primary flow fabrics making it impossible to characterize the associated PDC and identify source areas.
- Lastly, I further hypothesize, that the soon after the deposition the still hot and ductile ignimbrites were intruded by microgranite dikes and granites causing local domains of caldera resurgence.

References

Acocella, V. (2006). Caldera types: How end-members relate to evolutionary stages of collapse. *Geophysical Research Letters*, *33*, L18314.

Acocella, V. (2007). Understanding caldera structure and development: an overview of analogue models compared to natural calderas. *Earth-Science Reviews*, *85*, 125–160.

Agrò, A., Zanella, E., Le Pennec, J. L., & Temel, A. (2015). Magnetic fabric of ignimbrites: A case study from the Central Anatolian Volcanic Province. *Geological Society of London, Special Publications*, *396*, 159–175.

Babuška, V., & Plomerová, J. (2013). Boundaries of mantle-lithosphere domains in the Bohemian Massif as extinct exhumation channels for high-pressure rocks. *Gondwana Research*, *23*, 973–987.

Baer, E., Fischer, R., Fuller, M., & Valentine, G. (1997). Turbulent transport and deposition of the Ito pyroclastic flow: determinatoins using anisotropy of magnetic susceptibility. *Journal of Geophysical Research*, *102*, 22565–22586.

Benek, R. (1991). Aspects of volume calculation of paleovolcanic eruptive products – the example of the Teplice rhyolite (east Germany). *Zeitschrift Für Geologische Wissenschaften*, *19*, 379–389.

Borradaile, G. J. (2001). Magnetic fabrics and petrofabrics: their orientation distributions and anisotropies. *Journal of Structural Geology*, *23*, 1581–1596.

Borradaile, G. J., & Jackson, M. (2010). Structural geology, petrofabrics and magnetic fabrics (AMS, AARM, AIRM). *Journal of Structural Geology*, *32*, 1519–1551.

Branney, M. J., Barry, T. L., & Godchaux, M. (2004). Sheathfolds in rheomorphic ignimbrites. *Bulletin of Volcanology*, *66*, 485–491.

Branney, M. J., & Kokelaar, P. (1992). A reappraisal of ignimbrite emplacement: progressive aggradation and changes from particulate to non-particulate flow during emplacement of high-grade ignimbrite. *Bulletin of Volcanology*, *54*, 504–520.

Branney, M. J., & Kokelaar, P. (2002). *Pyroclastic Density Currents and the Sedimentation of Ignimbrites*. Geological Society of London Memoirs, 27, pp 143.

Breiter, K. (2012). Nearly contemporaneous evolution of the A- and S-type fractionated granites in the Krušné hory/Erzgebirge Mts., Central Europe. *Lithos*, *151*, 105–121.

Breiter, K., Förster, H. J., & Seltmann, R. (1999). Variscan silicic magmatism and related tin-tungsten mineralization in the Erzgebirge-Slavkovsky les metallogenic province. *Mineralium Deposita*, *34*, 505–521.

Breiter, K., Novák, J. K., & Chlupáčová, M. (2001). Chemical Evolution of Volcanic Rocks in the Altenberg – Teplice Caldera (Eastern Krušné Hory Mts., Czech Republic, Germany). *Geolines*, *13*, 17–22.

Breiter, K., Ďurišová, J., Hrstka, T., Korbelová, Z., Vaňková, M., Galiová, M. V., et al. (2017). Assessment of magmatic vs . metasomatic processes in rare-metal granites: a case study of the Cínovec/Zinnwald Sn-W-Li deposit, Central Europe. *Lithos*, *293*, 198–217.

Butler, R. F., & Banerjee, S. K. (1975). Theoretical single-domain grain size range in magnetite and titanomagnetite. *Journal of Geophysical Research*, *80*, 4049–4058.

Cagnoli, B., & Tarling, D. H. (1997). The reliability of anisotropy of magnetic susceptibility (AMS) data as flow direction indicators in friable base surge and ignimbrite deposits: Italian examples. *Journal of Volcanology and Geothermal Research*, *75*, 309–320.

Casas-García, R., Rapprich, V., Breitkreuz, C., Svojtka, M., Lapp, M., Stanek, K., et al. (2019). Lithofacies architecture, composition, and age of the Carboniferous Teplice Rhyolite (German-Czech border): insights into the evolution of the Altenberg-Teplice Caldera. *Journal of Volcanology and Geothermal Research*, *386*, 106662. doi:10.1016/j.jvolgeores.2019.106662

Cháb, J., Stráník, Z., Eliáš, M. (2007). *Geological map of the Czech Republic1:500.000.* Czech Geological Survey, Prague.

Chapin, C. E., & Lowell, G. R. (1979). Primary and secondary flow structures in ash-flow tuffs of the Gribbles Run paleovalley, central Colorado. *GSA Special Papers, 180*, 137–154.

Clark, D. A. (1997). Magnetic petrophysics and magnetic petrology: aids to geological interpretation of magnetic surveys. *AGSO Journal of Australian Geology & Geophysics*, *17*, 83–103.

Cole, J., Milner, D., & Spinks, K. (2005). Calderas and caldera structures: a review. *Earth-Science Reviews*, *69*, 1–26.

Dörr, W., & Zulauf, G. (2010). Elevator tectonics and orogenic collapse of a Tibetan-style plateau in the European Variscides: the role of the Bohemian shear zone. *International Journal of Earth Sciences*, *99*, 299–325.

Eisenreich, M., & Jeřábek, M. (1978). Geologická mapa teplického ryolitu 1:10 000. Česká geologická

služba, Praha.
Elston, W., & Smith, E. (1970). Determination of flow direction of rhyolitic ash-flow tuffs from fluidal textures. *Geological Society of America Bulletin, 81*, 3393–3406.
Fiala, F. (1960). Teplický křemenný porfyr mezi Krupkou, Cínovcem, Dubím a Mikulovem a horniny přidružené. *Sborník Ústředního Ústavu Geologického*, *26*, 445–494.
Finger, F., Gerdes, A., René, M., & Riegler, G. (2009). The Saxo-Danubian Granite Belt: magmatic response to post-collisional delamination of mantle lithosphere below the southwestern sector of the Bohemian Massif (Variscan orogen). *Geologica Carpathica*, *60*, 205–212.
Fisher, R. V., Orsi, G., Ort, M., & Heiken, G. (1993). Mobility of a large-volume pyroclastic flow – emplacement of the Campanian ignimbrite, Italy. *Journal of Volcanology and Geothermal Research*, *56*, 205–220.
Förster, H. J., & Tischendorf, G. (1994). The western Erzgebirge–Vogtland granites: implications to the Hercynian magmatism in the Erzgebirge–Fichtelge anticlinorium. In R. Seltmann, H. Kämpf, & P. Möller (Eds.), *Metallogeny of Collisional Orogens focused on the Erzgebirge and comparable metallogenic setting*, Czech Geological Survey, Prague.
Förster, H. J., Tischendorf, G., Trumbull, R. B., & Gottesmann, B. (1999). Late-collisional granites in the Variscan Erzgebirge, Germany. *Journal of Petrology*, *40*, 1613–1645.
Franke, W. (2006). The Variscan orogen in Central Europe: construction and collapse. *Geological Society of London Memoirs, 32*, 333–343.
Franke, W., & Zelazneiewicz, A. (2002). Structure and evolution of the Bohemian Arc. *Geological Society of London, Special Publications*, *201*, 279–293.
Fusán, O., Kodym, O., Matějka, A. (1967). *Geologická mapa Československa 1:500.000.* Kartografický a reprodukční ústav, Praha.
Gnojek, I., Sedlák, J., Rapprich, V., Skácelová, Z., Mlčoch, B., Krentz, O., & Casas-García, R. (2018). Structure of the Carboniferous Altenberg-Teplice Caldera (Eastern part of the Krušné hory/Erzgebirge Mts.) revealed by combined airborne and ground gamma-ray spectrometry. *Journal of Geosciences*, *63*, 3–20.
Grégoire, V., Darrozes, J., Gaillot, P., Nédélec, A., & Launeau, P. (1998). Magnetite grain shape fabric and distribution anisotropy vs rock magnetic fabric: a three-dimensional case study. *Journal of Structural Geology*, *20*, 937–944.
Guy, A., Edel, J.-B., Schulmann, K., Tomek, Č., & Lexa, O. (2011). A geophysical model of the Variscan orogenic root (Bohemian Massif): Implications for modern collisional orogens. *Lithos*, *124*, 144–157.
Holub, F. V., Machart, J., & Manová, M. (1997a). The Central Bohemian Plutonic Complex: geology, chemical composition and genetic interpretation. *Sborník Geologických Věd, Ložisková Geologie*, *31*, 27–50.
Holub, F. V., Cocherie, A., & Rossi, P. (1997b). Radiometric dating of granitic rocks from the Central Bohemian Plutonic Complex (Czech Republic): constraints on the chronology of thermal and tectonic events along the Moldanubian-Barrandian boundary. *Comptes Rendus de l'Académie Des Sciences - Series IIA - Earth and Planetary Science*, *325*, 19–26.
Hong, H., Yu, Y., Doh, S.-J., Suk, D., & Kim, J. (2016). Magnetic fabrics and source implications of Chisulryoung Ignimbrites, South Korea. *Frontiers in Earth Science*, *4*(August), 1–14.
Hrouda, F. (1982). Magnetic anisotropy of rocks and its application in geology and gephysics. *Geophysical Surveys*, *5*, 37–82.
Hrouda, F., & Kahan, Š. (1991). The magnetic fabric relationship between sedimentary and basement nappes in the High Tatra Mountains, N. Slovakia. *Journal of Structural Geology*, *13*, 431–442.
Janoušek, V., & Holub, F. V. (2007). The causal link between HP-HT metamorphism and ultrapotassic magmatism in collisional orogens: case study from the Moldanubian Zone of the Bohemian Massif. *Proceedings of the Geologists' Association*, *118*, 75–86.
Janoušek, V, Holub, F. V., Verner, K., Čopjaková, R., Gerdes, A., Hora, J. M., et al. (2019). Two-pyroxene syenitoids from the Moldanubian Zone of the Bohemian Massif: Peculiar magmas derived from a strongly enriched lithospheric mantle source. *Lithos*, *342–343*, 239–262.
Jelínek, V. (1981). Characterization of the magnetic fabric of rocks. *Tectonophysics, 79*, T63–T67.
Jiránek, J. (1991). *Geologická mapa Československa 1:25.000, list 02-322 Krupka*. Česká geologická služba, Praha.
Jiránek, J., Kříbek, B., Mlčoch, B., Procházka, J., Schovánek, P., Schovanková, D., et al. (1987). *Komplexní geologické zpracování teplického ryolitu.* Česká geologická služba, Praha.
Johan, V., & Johan, Z. (1994). Accessory minerals of the Cínovec (Zinnwald) granite cupola, Czech Republic Part 1: Nb-, Ta- and Ti-bearing oxides. *Mineralogy and Petrology*, *51*, 323–343.
Johan, Z., & Johan, V. (2005). Accessory minerals of the Cínovec (Zinnwald) granite cupola, Czech Republic: Indicators of petrogenetic evolution. *Mineralogy and Petrology*, *83*, 113–150.

Johan, Z., Strnad, L., & Johan, V. (2012). Evolution of the Cínovec (Zinnwald) Granite Cupola, Czech Republic: Composition of feldspars and micas, a clue to the Origin of W, Sn mineralization. *Canadian Mineralogist*, *50*, 1131–1148.
Klečka, M., & Matějka, D. (1996). Moldanubian Batholith – an example of the evolution of the Late Palaeozoic granitoid magmatism in the Moldanubian Zone, Bohemian Massif (Central Europe). In R. K. Srivastava, R. Chandra & A. A. Balkema (Eds.), *Magmatism in Relation to Diverse Tectonic Settings*, Oxford and IBH Publishing, New Delhi.
Klomínský, J., Jarchovský, T., & Rajpoot, G. S. (2010). *Atlas of plutonic rocks and orthogneisses in the Bohemian Massif: Lugicum*. Czech Geological Survey, Prague.
Knight, M. D., Walker, G. P., Ellwood, B. B., & Diehl, J. F. (1986). Stratigraphy, paleomagnetism, and magnetic fabric of the Toba Tuffs: constraints on the sources and eruptive styles. *Journal of Geophysical Research: Solid Earth*, *91*, 10355–10382.
Kotková, J., Schaltegger, U., & Leichmann, J. (2010). Two types of ultrapotassic plutonic rocks in the Bohemian Massif - Coeval intrusions at different crustal levels. *Lithos*, *115*, 163–176.
Kroner, U., & Romer, R. L. (2013). Two plates – Many subduction zones: the Variscan orogeny reconsidered. *Gondwana Research*, *24*, 298–329.
LaBerge, R. D., Porreca, M., Mattei, M., Giordano, G., & Cas, R. (2009). Meandering flow of a pyroclastic density current documented by the anisotropy of magnetic susceptibility (AMS) in the quartz latite ignimbrite of the Pleistocene Monte Cimino volcanic centre (central Italy). *Tectonophysics*, *466*, 64–78.
Lange, H., Tischendorf, G., Paelchen, W., Klemm, I., & Ossenkopf, W. (1972). Fortschritte der metallogenie im Erzgebirge. B. zur Petrographie und Geochemie der granite der Erzgebirges. *Geologie Deutschlands*, *21*, 457–489.
Liew, T. C., Finger, F., & Höck, V. (1989). The Moldanubian granitoid plutons of Austria: chemical and isotopic studies bearing on their environmental setting. *Chemical Geology*, *76*, 41–55.
Lipman, P. W. (1997). Subsidence of ash-flow calderas: relation to caldera size and magma-chamber geometry. *Bulletin of Volcanology*, *59*, 198–218.
Lobin, M. (1986). *Aufbau und Entwicklung des Permosiles im östlichen und mittleren Erzgebirge.* TU Bergakademie Freiberg, Ph.D. thesis.
MacDonald, W. D., & Palmer, H. C. (1990). Flow directions in ash-flow tuffs: a comparison of geological and magnetic susceptibility measurements, Tshirege member (upper Bandelier Tuff), Valles caldera, New Mexico, USA. *Bulletin of Volcanology*, *53*, 45–59.
Matte, P. (1986). Tectonic and plate tectonic model for the Variscan Belt of Europe. *Tectonophysics*, *126*, 329–374.
Mlčoch, B., & Skácelová, Z. (2010). Geometry of the Altenberg-Teplice Caldera revealed by the borehole and seismic data in its Czech part. *Journal of Geosciences*, *55*, 217–229.
Moncinhatto, T. R., Haag, M. B., Hartmann, G. A., Savian, J. F., Poletti, W., Sommer, C. A., et al. (2019). Mineralogical control on the magnetic anisotropy of lavas and ignimbrites: a case study in the Caviahue-Copahue field (Argentina). *Geophysical Journal International*, *220*, 821–838.
Müller, A., & Seltmann, R. (2002). Plagioclase-mantled K-feldspar in the Carboniferous porphyritic microgranite of Altenberg-Frauenstein, Eastern Erzgebirge/Krušné Hory. *Bulletin of the Geological Society of Finland*, *74*, 53–79.
Nagata, T. (1962). *Rock Magnetism*. Maruzen Company, Tokyo.
Opluštil, S., Schmitz, M., Cleal, C. J., & Martínek, K. (2016). A review of the Middle-Late Pennsylvanian west European regional substages and floral biozones, and their correlation to the Geological Time Scale based on new U-Pb ages. *Earth-Science Reviews*, *154*, 301–335.
Ort, M. H., Rosi, M., & Anderson, C. D. (1999). Correlation of deposits and vent locations of the proximal Campanian Ignimbrite deposits, Campi Flegrei, Italy, based on natural remanent magnetization and anisotropy of magnetic susceptibility characteristics. *Journal of Volcanology and Geothermal Research*, *91*, 167–178.
Ort, M. H., Orsi, G., Pappalardo, L., & Fisher, R. V. (2003). Anisotropy of magnetic susceptibility studies of depositional processes in the Campanian Ignimbrite , Italy. *Bulletin of Volcanology*, *65*, 55–72.
Ort, M. H., Porreca, M., Geissman, J. W., & Aquila, L. (2015). The use of palaeomagnetism and rock magnetism to understand volcanic processes: introduction. *Geological Society, London, Special Publications*, *396*, 1–11.
Palmer, H. C., & MacDonald, W. D. (1999). Anisotropy of magnetic susceptibility in relation to source vents of ignimbrites: empirical observations. *Tectonophysics*, *307*, 207–218.
Paterson, S. R., Fowler, T. K., Schmidt, K. L., Yoshinobu, A. S., Yuan, E. S., & Miller, R. B. (1998). Interpreting magmatic fabric patterns in plutons. *Lithos*, *44*, 53–82.
Pharaoh, T. C. (1999). Palaeozoic terranes and their lithospheric boundaries within the Trans-European

Suture Zone (TESZ): a review. *Tectonophysics*, *314*, 17–41.
Pin, C. (1990). Variscan oceans: Ages, origins and geodynamic implications inferred from geochemical and radiometric data. *Tectonophysics*, *177*, 215–227.
Pioli, L., Lanza, R., Ort, M., & Rosi, M. (2008). Magnetic fabric, welding texture and strain fabric in the Nuraxi Tuff, Sardinia, Italy. *Bulletin of Volcanology*, *70*, 1123–1137.
Pioli, L., & Rosi, M. (2005). Rheomorphic structures in a high-grade ignimbrite: the Nuraxi tuff, Sulcis volcanic district (SW Sardinia, Italy). *Journal of Volcanology and Geothermal Research*, *142*, 11–28.
Platzman, E. S., Sparks, R. S. J., & Cooper, F. J. (2020). Fabrics, facies, and flow through a large-volume ignimbrite: Pampa De Oxaya, Chile. *Bulletin of Volcanology*, *82*, 1–19.
Porreca, M. (2003). Magnetic fabric and implications for pyroclastic flow and lahar emplacement, Albano maar, Italy. *Journal of Geophysical Research*, *108*, 2264. doi: 10.1029/2002JB002102.
Potter, D. K., & Stephenson, A. (1988). Single-domain particles in rocks and magnetic fabric analysis. *Geophysical Research Letters*, *15*, 1097–1100.
Racek, M., Lexa, O., Schulmann, K., Corsini, M., Štípská, P., & Maierová, P. (2017). Re-evaluation of polyphase kinematic and 40Ar/39Ar cooling history of Moldanubian hot nappe at the eastern margin of the Bohemian Massif. *International Journal of Earth Sciences*, *106*, 397–420.
Rajlich, P. (1988). Tectonics of the NW border of the Central Bohemian Pluton and the Variscan transpression of the Bohemicum block structure. *Sborník Geologických Věd, Geologie*, *43*, 9–81.
Richter, C., van Der Pluijm, B. A., & Housen, B. A. (1993). The quantification of crystallographic preferred orientation using magnetic anisotropy. *Journal of Structural Geology*, *15*, 113–116.
Roche, O., Buesch, D. C., & Valentine, G. A. (2016). Slow-moving and far-travelled dense pyroclastic flows during the Peach Spring super-eruption. *Nature Communications*, *7*, 10890. doi: 10.1038/ncomms10890.
Rochette, P, Jackson, M., & Aubourg, C. (1992). Rock magnetism and the interpretation of magnetic susceptibility. *Reviews of Geophysics*, *30*, 209–226.
Rochette, P., Aubourg, C., & Perrin, M. (1999). Is this magnetic fabric normal? A review and case studies in volcanic formations. *Tectonophysics*, *307*, 219–234.
Rose, W., & Chesner, C. (1987). Dispersal of ash in the great Toba eruption, 75 ka. *Geology, 15*, 913–917.
Ross, C., & Smith, R. L. (1961). Ash-flow tuffs: their origin, geologic relations and identification and zones. *U.S. Geological Survey Professional Paper*, *366*, 1–77.
Šafanda, J., Verner, K., Franěk, J., Peřestý, V., Holeček, J., & Fischer, T. (2020). Geology and geothermal potential in the eastern flank of Eger Rift (Litoměřice area, Czech Republic). *Geothermics*, *86*, 101808. doi: 10.1016/j.geothermics.2020.101808
Schovánek, P. (2004a). *Geologická mapa České republiky 1:25.000, list 02-143 Cínovec*. Česká geologická služba, Praha.
Schovánek, P. (2004b). *Geologická mapa České republiky 1:25.000, list 02-321 Dubí*. Česká geologická služba, Praha.
Schovánek, P., Adamová, M., Breiter, K., Burda, J., Cajz, V., Elznic, A., et al. (2004). *Vysvětlivky k základní geologické mapě České republiky 1:25 000*. Česká geologická služba, Praha.
Schulmann, K., Konopásek, J., Janoušek, V., Lexa, O., Lardeaux, J. M., Edel, J. B., et al. (2009). An Andean type Palaeozoic convergence in the Bohemian Massif. *Comptes Rendus Geoscience*, *341*, 266–286.
Schulmann, K., Lexa, O., Janoušek, V., Lardeaux, J. M., & Edel, J. B. (2014). Anatomy of a diffuse cryptic suture zone: An example from the Bohemian Massif, European variscides. *Geology*, *42*, 275–278.
Schust, F. (1980). Zum Zusammenhang zwischen der paläogeographischen Entwicklung und der Intrusionstiefe der Granite im Osterzgebirge. *Zeitschrift Für Angewandte Geologie*, *26*, 405–411.
Sohn, Y. K., Son, M., Jeong, J. O., & Jeon, Y. M. (2009). Eruption and emplacement of a laterally extensive, crystal-rich, and pumice-free ignimbrite (the Cretaceous Kusandong Tuff, Korea). *Sedimentary Geology*, *220*, 190–203.
Soriano, C., Beamud, E., Garcés, M., & Ort, M. H. (2016). "Anomalous" magnetic fabrics of dikes in the stable single domain/superparamagnetic threshold. *Geophysical Journal International*, *204*, 1040–1059.
Sparks, R. S. J. (1976). Grain size variations in ignimbrites and implications for the transport of pyroclastic flows. *Sedimentology*, *23*, 147–188.
Stampfli, G. M., Hochard, C., Vérard, C., Wilhem, C., & vonRaumer, J. (2013). The formation of Pangea. *Tectonophysics*, *593*, 1–19.
Štemprok, M. (1993). Magmatic evolution of the Krušné hory-Erzgebirge batholith. *Zeitschrift Für Geologische Wissenschaften, 21*, 237–245.
Štemprok, M. (2016). Drill hole CS-1 penetrating the Cínovec/Zinnwald granite cupola (Czech Republic): an A-type granite with important hydrothermal mineralization. *Journal of Geosciences*, *61*, 395–423.

Štemprok, Miroslav, Holub, F. V, & Novák, J. K. (2003). Multiple magmatic pulses of the Eastern Volcano-Plutonic Complex, Krušné hory/Erzgebirge batholith, and their phosphorus contents. *Bulletin of Geosciences*, *78*, 277–296.

Štemprok, M., Dolejš, D., Müller, A., & Seltmann, R. (2007). Textural evidence of magma decompression, devolatilization and disequilibrium quenching: an example from the Western Krušné hory/Erzgebirge granite pluton. *Contributions to Mineralogy and Petrology*, *155*, 93–109.

Štemprok, M., Dolejš, D., & Holub, F. V. (2014). Late Variscan calc-alkaline lamprophyres in the Krupka ore district, Eastern Krušné hory/Erzgebirge: Their relationship to Sn-W mineralization. *Journal of Geosciences*, *59*, 41–68.

Tait, J. A., Bachtadse, V., Franke, W., & Soffel, H. C. (1997). Geodynamic evolution of the European Variscan fold belt: palaeomagnetic and geological constraints. *International Journal of Earth Sciences*, *86*, 585–598.

Tarling, D., & Hrouda, F. (1993). *Magnetic Anisotropy of Rocks*. London: Chapman & Hall.

Tischendorf, G., Förster, H. J. (1990). Acid magmatism and related metallogenesis in the Erzgebirge. *Geological Journal*, *25*, 443–454.

Tomek, F., Žák, J., Svojtka, M., Finger, F., & Waitzinger, M. (2019). Emplacement dynamics of syn-collapse ring dikes: An example from the Altenberg-Teplice caldera, Bohemian Massif. *Geological Society of America Bulletin*, *131*, 997–1016.

Veevers, J. J. (2004). Gondwanaland from 650-500 Ma assembly through 320 Ma merger in Pangea to 185-100 Ma breakup: Supercontinental tectonics via stratigraphy and radiometric dating. *Earth-Science Reviews*, *68*, 1–132.

Verner, K., Žák, J., Šrámek, J., Paclíková, J., Zavřelová, A., Machek, M., et al. (2014). Formation of elongated granite-migmatite domes as isostatic accommodation structures in collisional orogens. *Journal of Geodynamics*, *73*, 100–117.

Vigneresse, J.-L. (2001). Comparing granitic processes in Brittany and Saxony/NW Bohemia regarding to interactions between heat stress and source. *Zeitschrift Für Geologische Wissenschaften*, *29*, 1–22.

Walther, D., Breitkreuz, C., Rapprich, V., Kochergina, Y. V., Chlupáčová, M., Lapp, M., et al. (2016). The late Carboniferous Schönfeld–Altenberg depression on the NW margin of the Bohemian Massif (Germany/Czech Republic): Volcanosedimentary and magmatic evolution. *Journal of Geosciences*, *61*, 371–393.

Wang, X., Roberts, J., & Schmidt, P. (2001). Flow directions of Carboniferous ignimbrites, southern New England Orogen, Australia, using anisotropy of magnetic susceptibility. *Journal of Volcanology and Geothermal Research*, *110*, 1–25.

Wetzel, H. U. (1984). *Late Variscan faulting and subsequent magmatic dykes as expression of cortical development in the eastern Erzgebirge (Altenberg block)*. Zentralinstitut für Physik der Erde Potsdam, Academy of Sciences of the GDR, Potsdam, Germany. Ph.D. thesis.

Wetzel, H. U., Lobin, M., Pälchen, W., & Schilka, W. (1985). Eastern Erzgebirge (Upper Paleozoic). In R. Benek, H. Lützner, & G. Schwab (Eds.), *Late Paleozoic and Cenozoic continental sedimentation and magmatism in the southern part of the G.D.R*. Guidebook of excursions in the GDR Potsdam, Academy of Sciences of the GDR. 56–85.

Whitney, D. L., & Evans, B. W. (2010). Abbreviations for names of rock-forming minerals. *American Mineralogist*, *95*, 185–187.

Willcock, M. A. W., Mattei, M., Hasalová, P., Giordano, G., Cas, R. A. F., & Morelli, C. (2015). Flow behaviour in the intra-caldera setting: An AMS study of the large (>1290 km3) Permian Ora ignimbrite. *Geological Society of London, Special Publications*, *396*, 177–204.

Winchester, J. A., Pharaoh, T. C., Verniers, J., Ioane, D., & Seghedi, A. (2006). Palaeozoic accretion of Gondwana-derived terranes to the East European Craton: recognition of detached terrane fragments dispersed after collision with promontories. *Geological Society of London Memoirs*, *32*, 323–332.

Winter, C., Breitkreuz, C., & Lapp, M. (2008). Textural analysis of a Late Palaeozoic coherent-pyroclastic rhyolitic dyke system near Burkersdorf (Erzgebirge, Saxony, Germany). *Geological Society of London, Special Publications*, *302*, 199–221.

Žáček, V., & Škoda, R. (2009). Petrology of crystalline rocks in the geothermal borehole GTPV-LT1 in Litoměřice. *Geoscience Research Repports, 42*, 205–212.

Žák, J., Schulmann, K., & Hrouda, F. (2005). Multiple magmatic fabrics in the Sázava pluton (Bohemian Massif, Czech Republic): a result of superposition of wrench-dominated regional transpression on final emplacement. *Journal of Structural Geology*, *27*, 805–822.

Žák, J., Dragoun, F., Verner, K., Chlupáčová, M., Holub, F. V. & Kachlík, V. (2009). Forearc deformation and strain partitioning during growth of a continental magmatic arc: the northwestern margin of the Central Bohemian Plutonic Complex, Bohemian Massif. *Tectonophysics*, *469*, 93–111.

Žák, J., Verner, K., Holub, F. V., Kabele, P., Chlupáčová, M., & Halodová, P. (2012). Magmatic to solid

state fabrics in syntectonic granitoids recording early Carboniferous orogenic collapse in the Bohemian Massif. *Journal of Structural Geology*, *36*, 27–42.
Žák, J., Verner, K., Janoušek, V., Holub, F. V., Kachlík, V., Finger, F., et al. (2014). A plate-kinematic model for the assembly of the Bohemian Massif constrained by structural relationships around granitoid plutons. *Geological Society of London, Special Publications*, *405*, 169–196.
Žák, J., Svojtka, M., & Opluštil, S. (2018). Topographic inversion and changes in the sediment routing systems in the Variscan orogenic belt as revealed by detrital zircon and monazite U–Pb geochronology in post-collisional continental basins. *Sedimentary Geology*, *377*, 63–81.
Zrelak, P. J., Pollock, N. M., Brand, B. D., Sarocchi, D., & Hawkins, T. (2020). Decoding pyroclastic density current flow direction and shear conditions in the flow boundary zone via particle-fabric analysis. *Journal of Volcanology and Geothermal Research*, *402*, 106978.
Zulauf, G., Dörr, W., Fiala, J., & Kotková, J. (2002). Evidence for high-temperature diffusional creep preserved by rapid cooling of lower crust (North Bohemian shear zone, Czech Republic). *Terra*, 343–354.

Appendix A

Field maps:

Topographic maps of Czechia, 1:25000. Sheets: 02-321 Dubí; 02-322 Krupka; 02-143 Cínovec.
Topographic map of Germany,1:25000. Sheet: 5248 Altenberg.

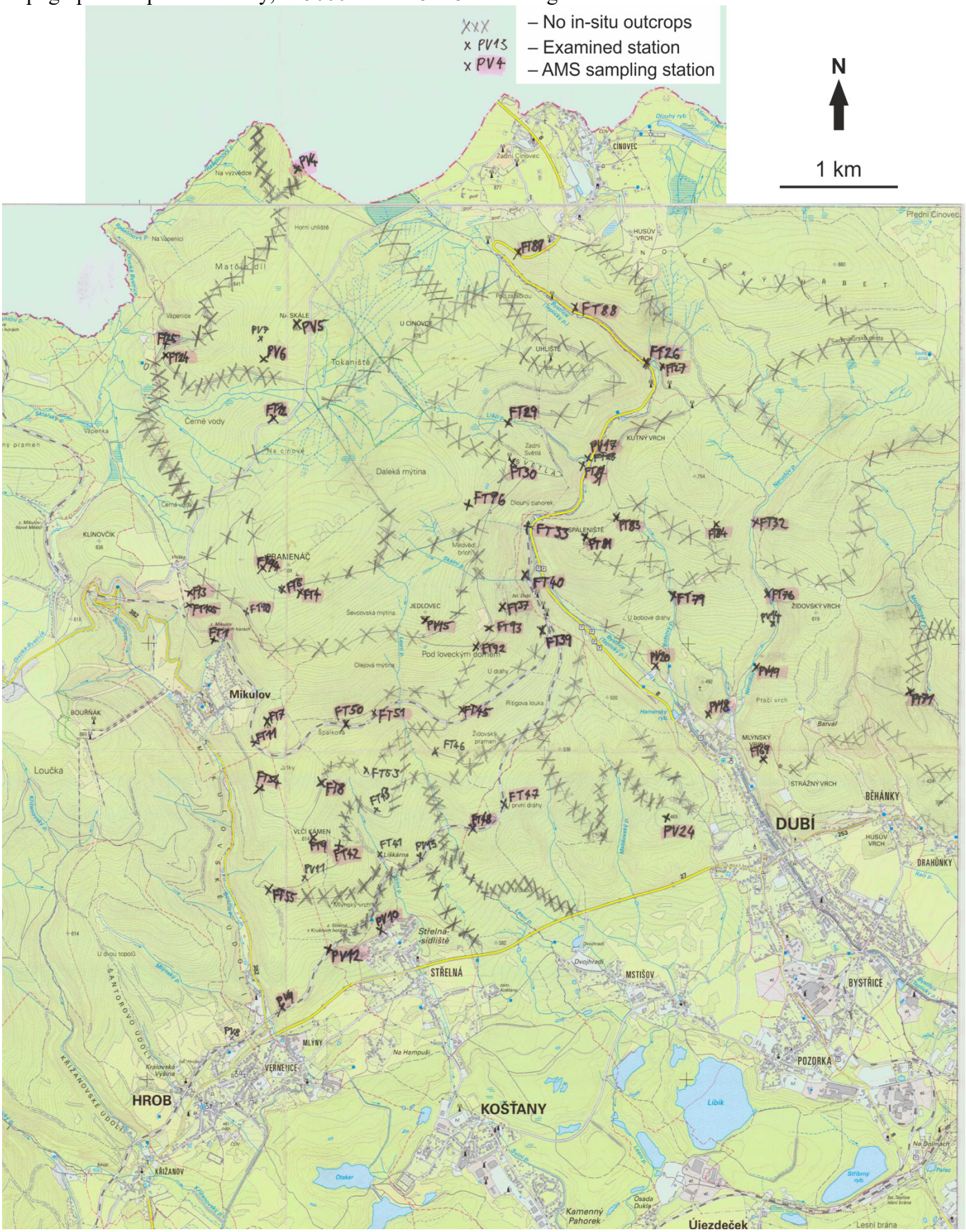

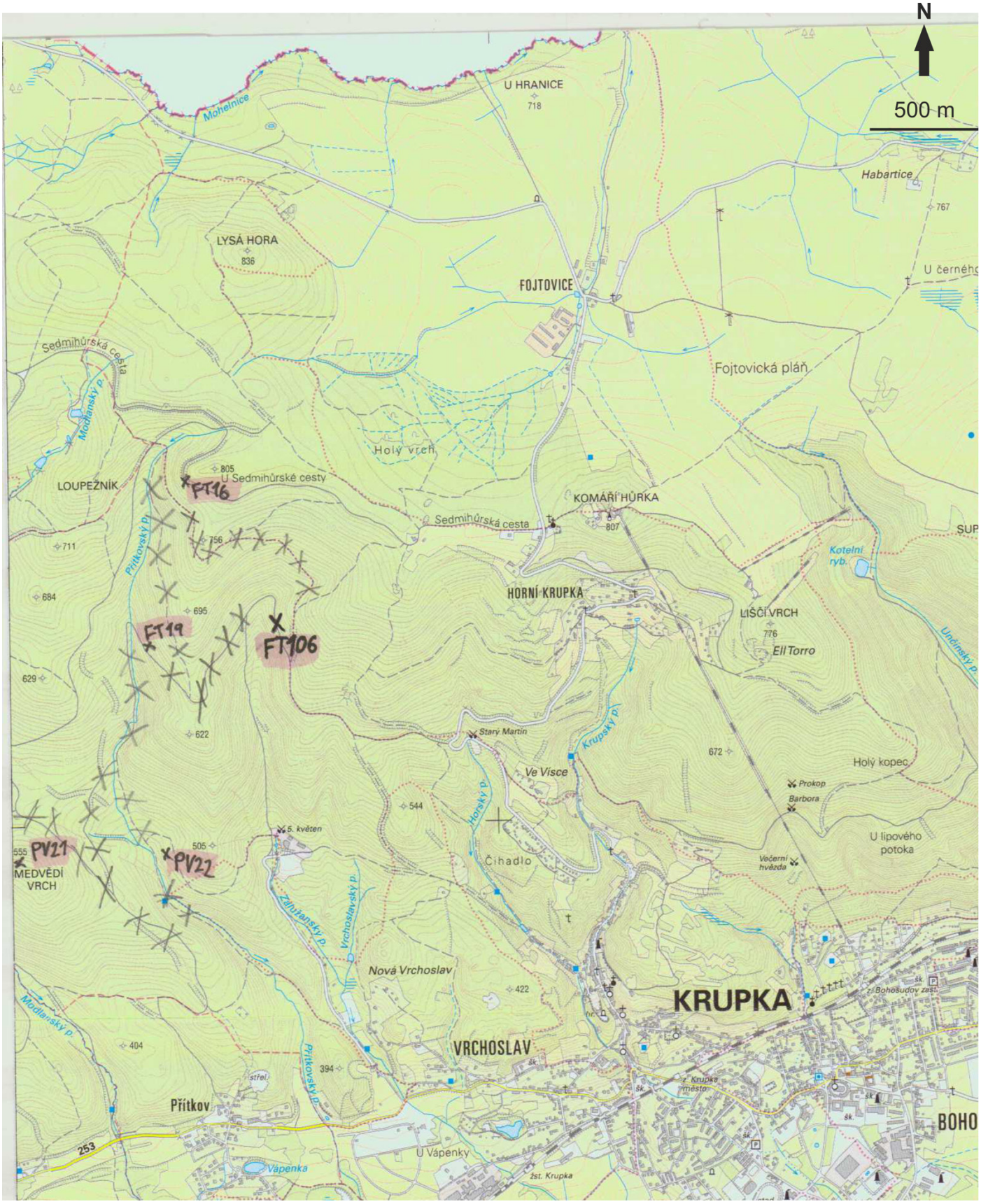
N
500 m
U HRANICE
718
Mohelnice
LYSÁ HORA
836
FOJTOVICE
Habartice
767
Sedmihůrská cesta
Modlanský p.
Fojtovická pláň
Holý vrch
LOUPEŽNÍK
805
U Sedmihůrské cesty
FT16
KOMÁŘÍ HŮRKA
807
Sedmihůrská cesta
711
756
Přítkovský p.
684
695
FT19
FT106
HORNÍ KRUPKA
Kotelní ryb.
LIŠČÍ VRCH
776
Ell Torro
629
622
Starý Martin
Krupský p.
672
Holý kopec
Ve Visce
Prokop
Barbora
544
Horský p.
5. květen
555
PV21
505
PV22
MEDVĚDÍ VRCH
Čihadlo
U lipového potoka
Večerní hvězda
Zdhřanský p.
Vrchoslavský p.
Nová Vrchoslav
422
KRUPKA
Modlanský p.
404
VRCHOSLAV
394
střel.
Přítkov
Přítkovský p.
253
U Vápenky
Vápenka
žst. Krupka
BOHO


N
500 m
Raupennest
Sonnenhof
Schwarzer Teich
Tanner-Stolln
Triangulationssäule Kahleberg
Gruner Stein
Kahleberg
Pfaffenbusch
Fritzschens Kuppe
Adamsloch
Neugraben
Tiefenbach
Quergraben
Sport
Schwarzer Teich
An den Räumen
Buchwald
Lugsteinhof
Georgenfeld
Klügelhütte
Großer Lugstein
Kleiner Lugstein
PV23
FT152
NSG Georgenfelder Hochmoor
Grenzgraben
Jägerhof
Jagdschloß
Gießhübel
REHEFELD-ZAUNHAUS
Wilde Weißeritz
Hemmschuh
Hemmschuh Stolln
ZINNWALD-GEOR
S182
S174a
170

Appendix B

Mean values of measured AMS properties per station, separated by affiliance to the members.

Teichweg

Name	N	Kaver	Laver	Faver	Paver	Taver	K1d [°]	K1i [°]	C1a [°]	C1b [°]	K3d [°]	K3i [°]	C3a [°]	C3b [°]
FT001A	14	1.02E-04	1.007	1.004	1.011	-0.273	112	12	9	4	262	77	6	4
FT001B	14	8.46E-05	1.005	1.010	1.015	0.148	107	12	27	7	231	70	15	6
FT003	18	5.92E-05	1.004	1.011	1.015	0.482	31	5	40	6	293	58	20	6
FT011	33	3.37E-04	1.003	1.004	1.007	0.084	292	26	15	5	71	57	6	5
FT024	23	4.34E-05	1.005	1.015	1.021	0.486	109	26	30	12	260	60	18	12
FT025	15	7.06E-05	1.003	1.007	1.010	0.347	107	21	20	7	247	63	11	8
FT054	27	1.89E-04	1.009	1.014	1.024	0.168	3	15	29	8	256	49	19	8
FT105A	13	5.42E-05	1.006	1.017	1.024	0.456	106	10	58	9	314	78	13	10
FT105B	10	4.79E-05	1.003	1.011	1.014	0.593	114	2	44	5	309	88	10	4

Lugstein-Pramenáč

Name	N	Kaver	Laver	Faver	Paver	Taver	K1d [°]	K1i [°]	C1a [°]	C1b [°]	K3d [°]	K3i [°]	C3a [°]	C3b [°]
FT004	17	3.02E-03	1.015	1.014	1.029	-0.048	96	60	8	5	267	30	18	5
FT006	23	1.60E-03	1.017	1.017	1.035	0.005	137	57	5	4	282	28	10	4
FT007	18	1.11E-03	1.011	1.010	1.021	-0.067	203	58	5	4	93	12	9	4
FT012	24	5.79E-04	1.008	1.004	1.012	-0.346	265	53	7	3	107	35	11	4
FT055	30	1.03E-04	1.011	1.003	1.014	-0.323	159	4	17	5	262	72	18	6
FT090	15	3.63E-04	1.004	1.005	1.010	-0.011	176	44	13	10	312	36	32	4
FT094	16	4.52E-04	1.006	1.003	1.010	-0.302	112	18	6	2	299	72	10	2
PV004	17	2.40E-03	1.013	1.010	1.023	-0.128	70	41	7	5	261	48	7	4
PV005	20	6.65E-04	1.010	1.012	1.021	0.129	70	61	13	7	299	20	15	8
PV006	17	2.75E-03	1.018	1.015	1.033	-0.101	92	53	9	6	286	36	13	6
PV023	16	2.24E-03	1.008	1.014	1.023	0.286	247	31	13	7	121	44	16	6

Vlčí kámen

Name	N	Kaver	Laver	Faver	Paver	Taver	K1d [°]	K1i [°]	C1a [°]	C1b [°]	K3d [°]	K3i [°]	C3a [°]	C3b [°]
FT008	26	1.57E-03	1.011	1.014	1.025	0.148	211	52	6	3	305	3	8	4
FT009	29	3.56E-04	1.001	1.008	1.009	0.696	189	15	42	5	283	16	8	4
FT029	18	1.02E-04	1.004	1.003	1.007	-0.247	45	20	18	9	283	56	16	10
FT030	29	4.76E-04	1.004	1.009	1.012	0.381	213	7	27	10	121	17	16	9
FT033	17	1.45E-04	1.004	1.003	1.007	-0.114	303	33	25	18	34	1	58	18
FT037	19	2.66E-03	1.009	1.006	1.016	-0.223	86	51	11	5	312	30	17	5
FT039	17	7.93E-05	1.002	1.002	1.004	-0.074	245	45	24	13	48	44	77	17
FT040	36	7.07E-05	1.004	1.003	1.007	-0.186	266	8	41	37	158	66	51	40
FT042	24	5.34E-04	1.005	1.009	1.014	0.295	11	80	23	11	110	2	18	11
FT045	17	1.11E-03	1.006	1.008	1.014	0.160	71	44	22	10	304	32	12	9
FT048	13	7.56E-04	1.005	1.015	1.021	0.353	13	27	36	2	111	15	13	2
FT050	14	2.48E-04	1.006	1.004	1.010	-0.201	173	46	8	6	338	44	9	7
FT051	15	2.69E-03	1.011	1.012	1.023	0.037	260	63	12	5	115	23	15	6
FT089	13	6.91E-05	1.005	1.009	1.014	0.235	283	21	8	6	186	17	7	6
FT092	21	1.39E-04	1.003	1.002	1.005	-0.244	9	13	22	10	107	30	21	9
FT093	13	1.95E-03	1.007	1.009	1.016	0.140	254	50	15	4	95	38	10	5
FT096	18	9.91E-04	1.005	1.010	1.015	0.290	297	40	21	11	131	49	26	16
FT157	20	1.76E-04	1.006	1.006	1.011	-0.027	145	77	8	4	344	13	23	3

Name	N	Kaver	Laver	Faver	Paver	Taver	K1d [°]	K1i [°]	C1a [°]	C1b [°]	K3d [°]	K3i [°]	C3a [°]	C3b [°]
PV009	19	2.96E-04	1.005	1.005	1.010	0.021	52	5	10	6	320	19	8	6
PV010	31	1.04E-03	1.004	1.006	1.010	0.206	194	34	12	4	286	3	7	4
PV012	19	4.61E-04	1.005	1.008	1.013	0.299	153	43	26	12	287	36	30	13
PV015	15	3.12E-04	1.002	1.005	1.008	0.382	259	69	19	6	112	18	10	6

Přední Cínovec

Name	N	Kaver	Laver	Faver	Paver	Taver	K1d [°]	K1i [°]	C1a [°]	C1b [°]	K3d [°]	K3i [°]	C3a [°]	C3b [°]
FT026	23	1.31E-04	1.004	1.006	1.010	0.238	238	24	23	6	139	19	26	6
FT027	22	2.55E-04	1.006	1.004	1.010	-0.107	42	31	59	17	133	3	37	17
FT031	17	2.75E-03	1.018	1.014	1.032	-0.154	26	81	19	6	151	5	15	6
FT032	26	3.22E-03	1.008	1.010	1.018	0.092	230	16	36	17	336	44	23	20
FT047	28	6.14E-04	1.007	1.006	1.013	-0.053	235	44	32	13	109	31	39	14
FT069	14	5.26E-03	1.009	1.009	1.018	0.036	214	1	14	5	306	65	12	5
FT071	23	4.95E-03	1.011	1.014	1.025	0.085	12	11	13	10	111	42	11	7
FT076	25	2.39E-03	1.015	1.008	1.023	-0.268	31	15	11	7	293	27	66	11
FT079	17	4.23E-04	1.015	1.007	1.022	-0.375	181	37	14	8	288	22	51	9
FT081	15	2.16E-03	1.007	1.011	1.018	0.210	212	30	25	10	314	20	15	9
FT083	20	3.52E-03	1.015	1.011	1.026	-0.155	226	10	13	9	318	9	22	9
FT084	17	3.79E-03	1.015	1.012	1.028	-0.125	55	1	11	4	315	85	16	4
FT088	22	1.63E-04	1.003	1.007	1.010	0.364	51	34	41	8	320	2	14	6
PV017	20	1.78E-03	1.015	1.015	1.030	-0.009	205	69	14	6	316	8	14	6
PV018	14	2.76E-03	1.018	1.005	1.023	-0.531	209	23	10	6	104	31	19	9
PV019	10	1.72E-03	1.020	1.009	1.029	-0.396	356	29	15	9	221	53	48	13
PV020	17	2.04E-03	1.014	1.011	1.025	-0.162	56	21	8	6	304	43	17	6
PV024	17	3.41E-03	1.012	1.005	1.017	-0.408	95	47	9	4	239	37	12	8

Medvědí vrch

Name	N	Kaver	Laver	Faver	Paver	Taver	K1d [°]	K1i [°]	C1a [°]	C1b [°]	K3d [°]	K3i [°]	C3a [°]	C3b [°]
FT016	14	8.79E-05	1.008	1.007	1.014	-0.057	250	64	9	5	149	5	17	8
FT019	10	2.83E-04	1.003	1.005	1.008	0.205	242	15	20	5	19	70	9	4
FT106	10	4.74E-05	1.010	1.011	1.021	0.096	341	1	59	9	71	53	11	9
PV021	15	2.78E-04	1.011	1.004	1.015	-0.465	21	3	9	7	289	30	55	7
PV022	13	2.08E-04	1.004	1.004	1.008	0.053	170	61	12	8	61	10	35	8